Studies for the LHCb SciFi Tracker

-

Investigation of SCSF-78 scintillating fibres performances and development of a novel class of highly efficient scintillating fibres

A thesis submitted for the degree of
DOCTOR OF NATURAL SCIENCES
(Dr. rer. nat.)

Laura Gavardi

Faculty of Physics
Technische Universität Dortmund

Dortmund, October 2017

Der Fakultät Physik der Technischen Universität Dortmund zur Erlangung des akademischen Grades eines Doktors der Naturwissenschaften vorgelegte Dissertation.

Gutachter:
Dr. Johannes Albrecht
Prof. Dr. Kevin Kröninger

Vorsitzender der Prüfungskommission:
Prof. Dr. Manfred Bayer

Datum der mündlichen Prüfung:
8. Januar 2018

Abstract

The LHCb detector will undergo a major upgrade during the Long Shutdown 2 of the LHC, which will take place from 2019 to 2020. As part of the upgrade, the main tracker will be replaced by a SciFi Tracker, based on scintillating fibres read out by SiPMs. Over $10'000\,\mathrm{km}$ of fibres are needed to build the SciFi Tracker, which will extend over an area of $360\,\mathrm{m}^2$. It will provide a spatial resolution of better than $85\,\mu\mathrm{m}$ and a detection efficiency of 98.7%.

This thesis presents a series of studies on scintillating fibres for the LHCb detector. A set of tests to ensure the quality of the fibres are described. Both the radiation resistance and the optical and geometrical properties are systematically monitored. The reported results refer to 6700 km of fibres, corresponding to 61% of the ordered quantity. The fibres performances are stable in time and within the specifications required for the SciFi Tracker. The average attenuation length amounts to 351 cm, the light yield to 13.8 photoelectrons and the degradation of the attenuation length after exposure to a dose of 1 kGy from 40 keV X-rays to $\Lambda'/\Lambda_0 = 0.72$. The fibres have a nominal diameter of $250\,\mu\mathrm{m}$. Occasionally occurring irregularities in the fibres shape are refined with a thermal procedure, conceived in order to reduce the diameter to a maximum of $350\,\mu\mathrm{m}$, without harming the fibre. The success rate is close to 100% for bumps smaller than $500\,\mu\mathrm{m}$. In case of failure of the shrinking procedure, which occurs on average once every 12.5 km of analysed fibres, the bump is manually cut away and the fibre glued with UV curing glue.

The radiation hardness of the fibres, which is one of the major hurdle faced by the SciFi Tracker, is a major topic of this manuscript. The dose profile in the Tracker rapidly changes over the length of each fibre: after 10 years of operations it will range from 40 Gy at one fibre's extremity to a maximum of 35 kGy at the other extremity. Several irradiation tests were performed on single fibres. The samples were irradiated up to different doses and the results used as input to simulate the ageing of the Tracker. A full SciFi module was irradiated with the same dose profile as in LHCb, confirming the simulated result. At the end of the Tracker's lifetime a signal loss of 40% is expected in the most irradiated region.

Finally, an ongoing R&D program will be presented, which aims at the development of a new class of scintillating fibres through the exploitation of the NOL mechanism. The prototype fibres do not yet excel in light yield nor in attenuation length. However, with their decay times constants of $\tau = 1.2$ - $1.4\,\mathrm{ns}$, they outperform the commercially available traditional fibres, the fastest of which provides $\tau = 2.4\,\mathrm{ns}$.

Contents

Chapter 1

Introduction

Scintillating fibres represent a well-established technology for particle detection. Their history began in 1957 when G. T. Reynolds and P. E. Condon prepared the first scintillating filaments, with different lengths and diameters between 0.5 and 1 mm [1]. The actual form of scintillating fibres, composed by a core material surrounded by a cladding, was proposed in the early 1980s [2]. They rapidly became a commercial product, with manufacturers in the US, Japan and France [3]. Scintillating fibres combine several appealing qualities, which make them to an attractive option for particle tracking. The granularity given by the small diameter leads to good spatial resolutions. The flexibility of the fibres allows to pack them in matrices in a variety of geometrical configurations, ensuring a high hit efficiency. The low density of the plastic material guarantees a low material budget, important to reduce the multiple scattering of the particles through the detector. Finally the low cost allows to instrument very large areas and the short decay time provides a good time resolution.

There are several examples of trackers based on scintillating fibres. One of those is the UA2 detector at CERN, which used sixty thousand fibres arranged in 24 cylindrical layers [4]. The 2 m long fibres had a diameter of 1 mm and provided a spatial resolution of better than 0.2 mm and a detection efficiency greater than 90%.

Another detector which exploited the characteristics of scintillating fibres is the Central Fibre Tracker of the D∅ experiment at Fermilab [5]. The fibres were mounted on eight concentric support cylinders, with each cylinder supporting an axial and a stereo doublet layers of fibres. The obtained doublet layer resolution amounted to about 100 μm and the hit efficiency to 99.5%.

The excellent timing properties of scintillating fibres will be exploited by the Mu3e experiment in the search for the lepton flavour violating decay $\mu^+ \rightarrow e^+e^-e^+$ [6]. The detector will include a fast scintillating fibre hodoscope to discriminate against the combinatoric background from $\mu^+ \rightarrow e^+\overline{\nu}_\mu\nu_e$ decays.

Scintillating fibres are also used in astrophysics. Just to mention one example, the Cosmic Ray Isotope Spectrometer (CRIS), whose aim is the measurements of the isotopes of galactic cosmic ray nuclei from helium to zinc over an energy range of about 100 to 500 MeV/nucleon, is one of the instruments aboard the ACE spacecraft [7]. CRIS is equipped with a Scintillating Optical Fiber Trajectory (SOFT) hodoscope to measure the particles trajectories.

Currently under construction is a main upgrade of the LHCb detector at the LHC [8]. The LHCb experiment specializes in the precise study of flavour physics in the search for effects of new physics beyond the Standard Model. The goal of the upgrade, which will take place in 2019 - 2020, is to increase the statistical sensitivity to key observables, allowing to attain unprecedented precision in flavour physics. As a part of the upgrade, the current main tracker will be replaced by a SciFi Tracker, based on scintillating fibres read out by SiPMs [9]. It will use more than 10′000 km of 250 µm diameter fibres in a planar configuration. Each of the 12 planes, which will extend over 6 m in width and 4.8 m in height, will be composed of 12 SciFi modules. The fibres in each module will be glued together in a six-layer geometry.

As mentioned above, the efficacy of scintillating fibres as particle detectors was demonstrated in the past in numerous occasions. However, the SciFi Tracker will push this technology to the limits. The challenges are defined by the LHCb performance requirements and by the harsh environment at the LHC. The fibres will be 2.5 m long, read out at one extremity and mirrored at the other end. To be detected by the SiPMs, the produced scintillation photons will travel up to 2.5 m and the ones reflected at the mirror up to 5 m. Therefore a high transport efficiency is required, corresponding to an attenuation length of at least 3 m. At the same time, with the LHC bunch spacing of 25 ns and a propagation time of the light through the fibre of 6 ns/m, the decay time should be as small as possible. Finally, the biggest challenge will be provided by the unprecedented ionizing dose to which the fibres will be exposed. It will amount to 35 kGy in the most affected region at the end of the SciFi Tracker's lifetime. To contrast the effect of the induced degradation the light yield of the fibres should be as high as possible.

A big drawback of plastic scintillators is indeed represented by their moderate radiation hardness, which prevents or at least limits their use in harsh radiation environments. The outcome of exposure to ionising dose is an increase of the photons attenuation in the scintillator, i.e. a decrease of the transport efficiency of the fibre. The direct consequence is a reduction of the number of photons which can be collected at the end of the fibre by the photodetector.

An attempt to mitigate the problems deriving from the ageing of fibres in a radiation environment is provided by the so-called NOL material [10, 11]. It is a novel scintillation material, which promises a higher light yield with respect to conventional scintillators. An R&D program is still ongoing to successfully apply this novel technology to scintillating fibres.

This thesis project focuses on the properties, especially the radiation resistance, of scintillating fibres for the upgraded LHCb detector. The first chapters give a general introduction to the topic. In particular, Chapter 2 reviews the working principle of scintillating fibres and their characteristics. It also summarises the main results from existent studies in the literature on radiation hardness of plastic scintillators. Chapter 3 introduces the LHCb detector and its upgrade, with a main emphasis on the SciFi Tracker, which is currently in the production phase. The over $10'000\,\mathrm{km}$ of fibres needed to build the SciFi Tracker are produced by the Japanese company Kuraray[1] and systematically examined after delivery. The numerous tests performed to ensure the quality of the fibres are presented in Chapter 4. The quality assurance inspections aim at the monitoring of the optical and geometrical characteristics of the fibres, as well as their degradation after exposure to X-rays.

From the literature review in Chapter 2 it will be clear that the degradation of plastic scintillators depends on a huge amount of factors like, for instance, the dopants used, the absorbed dose, the radiation source, the gas atmosphere during and after irradiation. The contribution of all these factors leads to sometimes inconclusive or even contradictory results in the published papers dealing with this topic. In particular the fibres chosen for the SciFi Tracker have received limited study in literature. It is therefore mandatory to study the ageing of these specific fibres under well defined conditions in order to predict their behaviour in the environment of the upgraded LHCb experiment. For this reason several irradiation campaigns were performed by the SciFi Group. Chapter 5, 6 and 7 describe some of these tests and their results.

One of the most debated topics in the literature is the effect of the dose rate. Some authors, quoted in Chapter 2, claim that irradiations carried out with low dose rates are more deleterious than exposures to high dose rates. This is a very important point for the SciFi project because the dose rate in the upgraded LHCb detector will be about 10^{-2} - 10^{-5} Gy/h, while most of the irradiation tests were performed at accelerators with dose rates of 10^{4} - 10^{7} Gy/h. The dose rate dependency of the LHCb fibres is addressed in both Chapter 5 and 6.

Finally the last chapter is dedicated to the afore mentioned R&D program about NOL-based scintillating fibres. The chapter reports on the current status of this ambitious project and gives an outlook on the next steps that are going to be undertaken.

---

[1] Kuraray Co. Ltd., Tokyo, Japan

Chapter 2

Scintillating fibres

Scintillators are widely used as particle detectors. Their field of application ranges from particle and nuclear physics to astrophysics and medical physics.
The discussion here follows the review in Ref. [12]. Scintillators can be divided into two main categories: organic and inorganic scintillators. The scintillation mechanism is different for this two classes. In inorganic materials the scintillation is the result of impurities or defects in the crystalline lattice. Energy deposited in the crystal can excite electrons into the conduction band. De-excitation can proceed either by thermal dissipation or by light emission. On the other side, scintillation in plastic material is given by the excitation of π-electrons of the benzene ring of an aromatic polymer chain. In this second case scintillation is an intrinsic property of the molecules, exhibited in the solid, liquid and vapour state. The characteristics of organic and inorganic scintillators differ in many aspects. Whereas organic materials have low densities ($\rho \sim 1\,\mathrm{g/cm^3}$) and fast decay times ($\tau = 1$ - $10\,\mathrm{ns}$), their inorganic counterpart show higher densities (typically ~ 4 - $8\,\mathrm{g/cm^3}$) and are slower (ns - μs). The high light output provided by inorganic crystals compares with smaller yields given by plastic scintillators (~ 70000 photons/MeV versus ~ 10000 photons/MeV).
The high density and atomic number make inorganic scintillators suitable for calorimetry or gamma and X-ray detection. Organic materials are widely employed in tracking devices or timing detectors.

Scintillating fibres combine the qualities of scintillating detectors with the fine granularity and flexibility provided by the fibre technology.
The base material in a scintillating fibre is a scintillator, such as plastic, glasses or liquids in capillaries [3, 13]. Plastic, such as polystyrene (PS) or polyvinyltoluene (PVT), is the most convenient among these options. It is more efficient, faster in response and has a lower material density than glasses. It also shows mechanical advantages (it is simpler and more robust) with respect to the capillary structures used to support liquid scintillators. In particular, polystyrene has a higher refractive index and it is easier to draw than PVT.
The working principle of scintillating fibres is based upon the scintillation

mechanism combined with trapping and transport of the produced photons by total internal reflection inside the fibre. Key properties of scintillating fibres are the scintillation light yield, the decay time and the attenuation length. When an ionizing particle traverses a scintillator, it transfers part of its energy producing an excitation of the scintillating material. The light yield is the number of produced photons per deposited energy in the fibre. Photons are emitted when the fibre's compounds relax to the ground state. The excited species have a characteristic mean lifetime, and their population decays exponentially. The decay time determines the rate at which the light is emitted following the excitation and is characteristic of the particular scintillation material. The probability of survival of a photon transported through the fibre over a distance d is given by the Beer-Lambert law $P(d) = e^{(-d/\Lambda)}$, where the attenuation length $\Lambda(\lambda)$ is material and wavelength dependent. Alternatively, the absorption coefficient $\alpha(\lambda) \equiv \mu(\lambda) \equiv [\Lambda(\lambda)]^{-1}$ is used, e.g. in the context of radiation damage (often in this case the additional absorbtion, $\Delta\mu \equiv \mu_{\mathrm{irrad}} - \mu_{\mathrm{unirrad}}$, is quoted).

This chapter presents the properties of scintillating fibres (scintillation process and light collection and transport). The discussion is followed by a review of the literature on the radiation hardness of plastic scintillators.

2.1 Scintillation process

The information given in this and in the following section follow the general overviews in Ref. [3, 13].

A minimum ionizing particle deposits about 200 keV/mm in polystyrene. A few eV of deposited energy are required to produce an excitation of molecular levels in the benzene rings of the polymer chain. Unfortunately, pure polystyrene has a poor quantum efficiency. Moreover, it emits photons in the wavelength range 280 - 400 nm, with maximum intensities in the region between 310 - 340 nm (Fig. 2.1). At the same time, in this wavelength region, polystyrene exhibits a very high absorption, due to effects such as Rayleigh scattering, molecular vibrations and electronic transitions (Fig. 2.2). These inefficiencies are overcome by doping the polymer base with an organic fluorescent dye with suitably matching excitation energy levels, the so-called "activator". Some examples of activators are p-Terphenyl (p-Tp), 2-(4-t-butylphenyl)-5-(4-biphenylyl)-1,3,4-oxadiazole (bPBD) and 3-hydroxyflavone (3HF). The concentration of the dopant is chosen to be about 1% by weight, so that the distance between a dye molecule and any excitation site in the polymer is in the order of a nanometre. In this way energy is quickly (less than 1 ns) transferred via non-radiative dipole-dipole coupling through the mechanism known as Förster transfer [14]. Important features of the dye are a high quantum efficiency, less than a few nanoseconds decay time and an emission spectrum such that the photons emitted after the relaxation to the ground state are less strongly absorbed by polystyrene. The energy transmission via radiative process is also possible and it competes with the Förster transfer. Whilst the rate

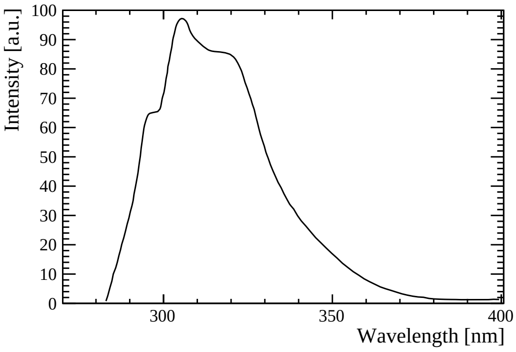

Figure 2.1: Emission spectrum of undoped polystyrene [3].

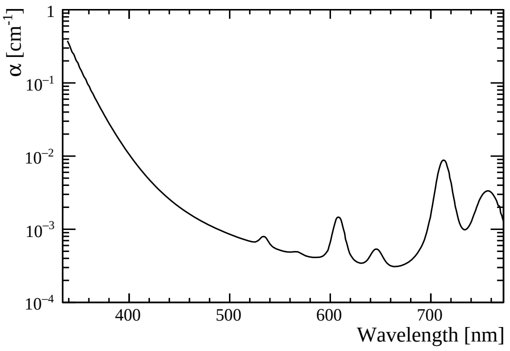

Figure 2.2: Photons attenuation in undoped polystyrene [3].

of the dipole coupling can be increased by a higher dopant concentration, this would also lead to a higher self-absorption. A secondary dye, often referred to as "wavelength shifter", can be added in a very low concentration (about 0.05% by weight). The wavelength shifter absorbs the blue or UV photons from the activator and re-emits them at longer wavelengths, thus increasing the overall transparency of the fibre. Typical wavelength shifters are tetraphenyl-butadiene (TPB) and 1,4-bis(5-phenyloxazol-2-yl) (POPOP). The admixture of the second dye can be avoided if the activator has a strong Strokes' shift, i.e. high separation between the absorption and emission spectrum, as it is the case of 3HF. However this higher transparency comes at the cost of a longer decay time. In particular 3HF has a decay time of 6 ns, which is about 2.5 times higher than the decay time of TPB. Absorption and emission spectra of typical compounds used in plastic scintillators are shown in Fig. 2.3.

2.2 Light trapping and transport

The photons emitted by the dye are isotropically oriented. The fibre core is surrounded by either one or two claddings, where the multi-cladding configuration is both mechanically and optically more performant. The thickness of each cladding is typically $\leq 3\%$ of the total fibre diameter. The claddings have smaller refractive index than the fibre core, for example polymethylmethacrylate (PMMA, $n = 1.49$) can be used for the inner cladding and a fluorinated polymer ($n = 1.42$) for the external cladding, while polystyrene has a refractive index $n = 1.59$. The photons crossing the fibre axis are then trapped inside the fibre by total internal reflection if they fulfil the requirement $\vartheta > \vartheta_{crit} = \arcsin(n_{\text{clad}}/n_{\text{core}})$, where ϑ is their angle of incidence relative to the surface normal (Fig. 2.4). Considering the materials mentioned above, the fraction of the trapped photons which will be transported towards one end of the fibre is $d\Omega/4\pi = 3.1\%$ ($\vartheta_{crit} = 20.4°$) for single cladding and $d\Omega/4\pi = 5.3\%$ ($\vartheta_{crit} = 26.7°$) for multi-cladding fibres. The trapped photons can be lost at the core-cladding or cladding-cladding interface if

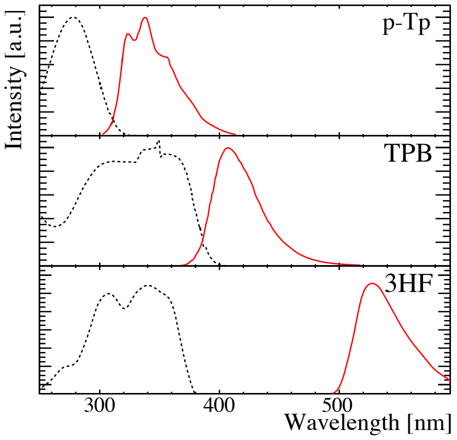

Figure 2.3: Absorption (black dashed curves) and emission (red straight curves) spectra of some typical compounds used in plastic scintillators [15–17].

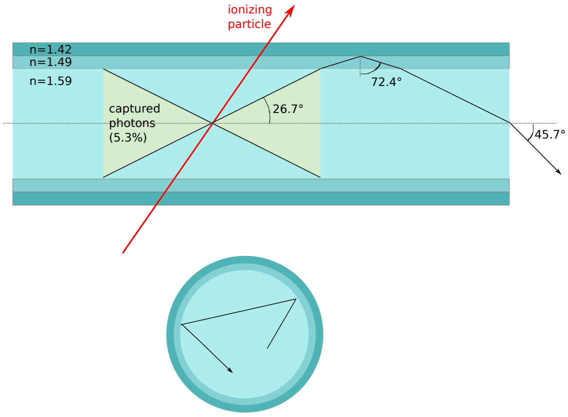

Figure 2.4: Side and front view of a multi-cladding fibre. Possible trajectories of meridional (top) and non-meridional (bottom) photons trapped inside the fibre are also sketched.

the surfaces are not regular. In reality the trapping fraction is higher, because photons with non-meridional trajectories, i.e. non crossing the fibre axis, can be reflected even with an angle smaller than ϑ_{crit}. However, as illustrated in Fig. 2.4, those photons follow helicoidal paths and are therefore quickly lost, due to the longer path-length and the higher number of reflections to which they are subjected when travelling through the fibre.

2.3 Radiation damage of plastic scintillators

The literature about radiation induced damage to plastic scintillators is extremely wide. What emerges is that the degradation depends on several factors such as total absorbed dose, dose rate, temperature and gas environment. Furthermore, the choice of the polymer and of the dyes, as well as the dimensions of the scintillator can affect the radiation hardness of the detector. As a result, the published papers are not always in complete agreement, sometimes even in open contradiction. A summary of some of those results is reported in the following.

The first question to be addressed concerns the origins of the degradation. Irreversible damages, such as loss of mass, cracks and bubbles can occur in the polymer [18, 19]. Besides the physical consequences, also chemical reactions can be induced. Free radicals are created in plastic scintillators during irradiation [20–22]. At least three distinct radical species were identified with Electron Spin Resonance (ESR) studies in polystyrene after γ irradiation [23]. The free radicals can annihilate through interaction either with other radicals or with oxygen [21]. Thus it can be distinguished between two types of induced damage: a “permanent” one, related to irreparable changes in the structure of the polymer, and an “annealable” one, associated with radicals which disappear after irradiation. The exposure to radiation results in a reduced fluorescence efficiency and in the creation of additional absorption centers and hence in a loss of transparency.

Studies have been performed to determine if the type of the incident radiation can influence the result: no difference was seen between irradiations with protons, electrons or γ-rays from a ^{60}Co source [24, 25]. Tests with fast neutrons were also performed, leading to the conclusions that this kind of radiation does not contribute to the observed damage [26].

The degradation of pure polystyrene has been studied after exposure to γ-rays with a ^{60}Co source [22, 27, 28]. Figure 2.5 shows the additional absorption $\Delta\mu(\lambda)$ after a dose of 50 kGy. The damage rises with decreasing wavelength and a transient absorption peak is to be seen at $\lambda = 525\,\text{nm}$.
Whether the dyes suffer from the irradiation is debated. The authors of Ref. [22] observed identical sets of PS-based scintillators which contained p-Terphenyl plus either BBQ, 3HF or dimethyl-POPOP as dopants. One set was made with pure dopants, whilst the other set was made with pure dopants which had been previously irradiated with large dose of γ-radiation. The authors could not see any difference neither during nor after irradiation of the scintillators, hence they concluded that the dyes are not susceptible to radiation.
On the other hand the comparison of scintillating fibres (PS-based plus various dopants) and clear fibres (pure PS) after exposure to γ-rays [19] or 100 keV X-rays [21, 29] shows that the scintillating fibres are more strongly harmed than the clear fibres. This leads to the conclusion that the dyes contribute to the overall degradation of the fibres. In particular a transient absorption band in the wavelength region between 500 nm and 700 nm is observed in the fibres BCF-12[1] and SCSF-978[2] and a stronger damage, especially in the blue wavelengths, persists in the fibres SCSF-38[2] and SCSF-81[2].

A dependence on the dopants choice has also been reported as far as the relation between performance degradation and total absorbed dose is concerned. The permanent damage in pure polystyrene rises linearly with the dose as shown in Figs. 2.6 and 2.7 [28, 29]. For the scintillating fibre SCSF-38[2], at $\lambda = 430\,\text{nm}$ the permanent damage rises faster at low dose ($< 750\,\text{Gy}$) than at higher doses, and also at $\lambda = 610\,\text{nm}$ a non-linear behaviour is observed (Fig. 2.8, [29]). The ratio of the attenuation length after to before the irradiation with ^{60}Co has been plotted as a function of the dose for a clear fibre (pure PS) and a scintillating fibre doped with 3HF [30]: the data points seem to lie on a single line with a logarithmic dependence from the dose (Fig. 2.9).

Particular attention has been dedicated to the influence of the surrounding

---

[1] Bicron Corporation, now Saint-Gobain Crystals, Hiram, Ohio, U.S.A.

[2] Kuraray Co. Ltd., Tokyo, Japan

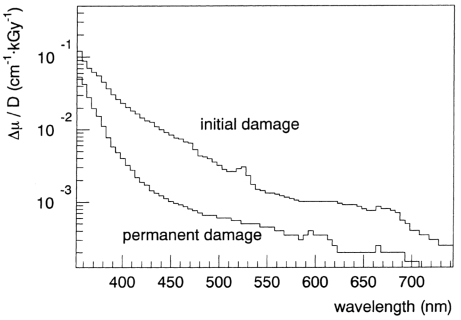

Figure 2.5: Initial (e.g. directly after the end of the irradiation) and permanent damage in pure PS after exposure to γ-rays from a ^{60}Co source to a dose of 50 kGy (Figure taken from Ref. [21], calculated from data in Ref. [27]).

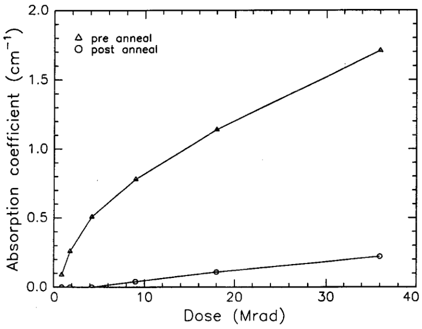

Figure 2.6: Transient ("pre anneal.") and permanent ("post anneal.") absorption in pure PS at a wavelength of 430 nm after irradiation with a ^{60}Co source and a dose rate of 3 kGy/h [28].

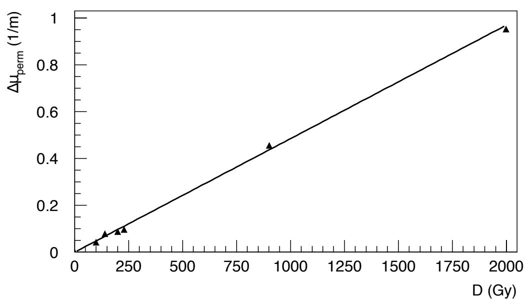

Figure 2.7: Permanent optical damage of pure PS (clear fibre BCF-98) at a wavelength of 425 nm after irradiation with a 100 keV X-ray source and a dose rate of 37 Gy/h [29].

gas atmosphere during and after irradiation. Several experiments showed that the annealing is much faster in presence of oxygen, regardless of the conditions during irradiation [21, 22, 31]. Nevertheless, there are indications that the presence of oxygen during irradiation may enhance the damage. Discs of pure polystyrene of 1 cm thickness were irradiated to the same dose of 100 kGy and with the same dose rate of 10 kGy/h in nitrogen, in air (STP), and in oxygen at 2 atm and at 40 atm absolute [22]. Directly after irradiation the sample irradiated in oxygen at 40 atm showed the smallest damage, but after two weeks annealing in air it had the biggest damage, whilst the sample irradiated in nitrogen was the less susceptible (Fig. 2.10). In addition to this, no dose rate effects were seen when irradiating with either 300 Gy/h or 10 kGy/h to a dose of 100 kGy in inert gas atmosphere (nitrogen or argon). The conclusion of the authors is that the oxidation products created during irradiation decrease the performance of the scintillator. This could imply the possibility that high dose rate experiments underestimate the damage caused by low dose rate irradiations, because oxygen diffusion is a time dependent process. In particular, in the case of a high dose

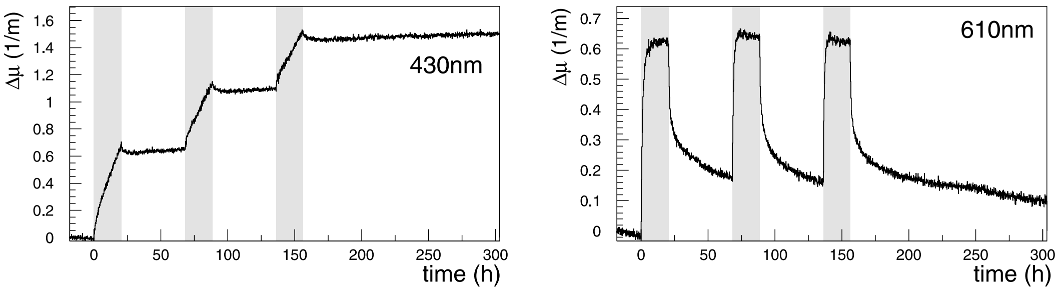

Figure 2.8: Time dependence of the radiation-induced absorption $\Delta\mu$ during and after a triple irradiation of the fibre SCSF-38 (exposure times: $3 \times 20.5\,\mathrm{h}$, dose rate: 36 Gy/h, total dose: 2.2 kGy, grey background = exposure time) [29]. At 430 nm the permanent damage increases by $\Delta\mu = 0.6\,\mathrm{m}^{-1}$ in the first irradiation (up to 738 Gy) and by $\Delta\mu = 0.35\,\mathrm{m}^{-1}$ in the third irradiation. At 610 nm $\Delta\mu$ saturates at the same level for all three irradiations.

rate irradiation all the oxygen will interact with the freed radicals on the surface of the sample and it will not diffuse into the scintillator.

Large polystyrene-based scintillators doped with PPO and POPOP with a thickness of 19 cm were irradiated in air with a ^{60}Co γ-rays source with a dose rate of either 0.1 Gy/h or 85 Gy/h to the same doses and it was found that at the lower dose rate the detectors were less resistant [32].

On the other hand the polystyrene-based SCSN-38[3], 2 mm thick scintillators, did not show any dose rate effect when exposed to ^{60}Co at either 30 Gy/h, 100 Gy/h, or 1000 Gy/h under otherwise identical conditions [31]. The authors also irradiated SCSN-38 and SCSN-61[3] materials in nitrogen or air with a 25 MeV proton beam. Afterwards the samples were stored in the same gas atmosphere as during irradiation. The measured induced absorption ($\chi \equiv \Delta\mu$) is shown in Fig. 2.11: in air the initial damage was much smaller and the annealing much faster, but the recovery in nitrogen lead to a smaller permanent damage after about 100 days.

The irradiation of polystyrene-based scintillating fibres BCF-12 with 100 keV X-rays [21] showed that the initial damage is considerably reduced if oxygen is present during irradiation (Fig. 2.12). The authors' conclusion was that the peroxy radicals produced from the interaction of free radicals with oxygen do not act as absorption centres and therefore when oxygen is present the annealing takes place already during irradiation. The authors reported also the presence of dose rate effect when irradiating in argon: the higher the dose rate, the stronger the initial damage (Fig. 2.13).

The role of temperature and its effect on the the fibres performances was also investigated. A transmission loss was observed in the scintillating fibre SCSF-38 when exposed to temperatures higher than 40°C, without irradiation [33]. The exposure to high temperature can also influence the radiation resistance of a

---

[3] Kyowa Gas Chemical Co., Ltd., now Kuraray Co. Ltd., Tokyo, Japan

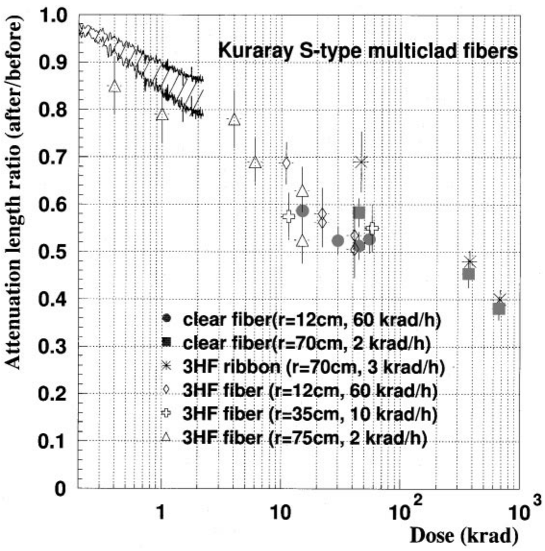

Figure 2.9: Ratio of attenuation length after to before irradiation with a ^{60}Co source. The shaded region shows the range of the ratio for a clear fibre where the attenuation length was evaluated during irradiation at 20 Gy/h. Other data were measured 1-2 weeks after the irradiation. [30].

scintillator. In particular it has been shown that if the scintillators SCSN-38, SCSN-81 (Kuraray) and RH-1 (Bicron) are previously stored in air or vacuum at temperatures higher than 54°C, although no degradation is seen after the heating, the damage caused by a subsequent irradiation to 10 kGy is stronger [34].
On the other hand a process of thermal annealing is reported for pure polystyrene: after a total dose of 400 kGy the recovery by heating is more efficient than annealing in oxygen [22], and an increase in the temperature (30°C - 90°C) after a dose of 100 kGy results in a faster annealing [28].

As stated at the beginning of this section, the literature on radiation hardness of plastic scintillators is extremely wide. The full picture remains however unclear and unsatisfactory, since it is not possible to extrapolate the degradation of a specific scintillator in any determined radiation environment. Before the construction of a detector exploiting plastic scintillators, their radiation hardness should be tested under conditions which come as close as possible to the ones in the real detector.

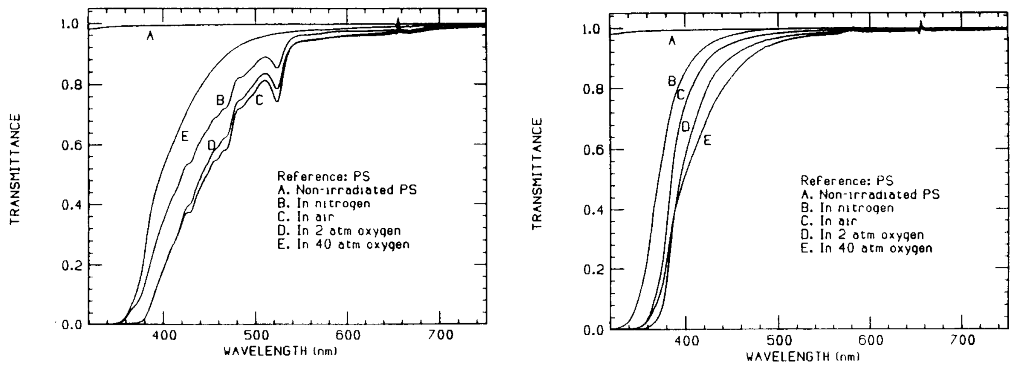

(a) (b)

Figure 2.10: Transmittance spectra for pure PS after irradiation in different gas atmospheres (a) directly after irradiation up to 100 kGy and (b) after two weeks annealing period in oxygen [22].

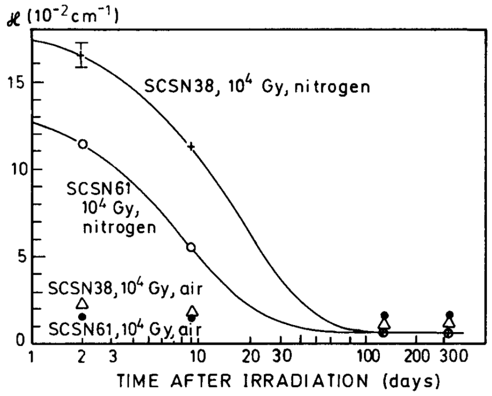

Figure 2.11: Induced absorption after irradiation and annealing in air and in nitrogen [31].

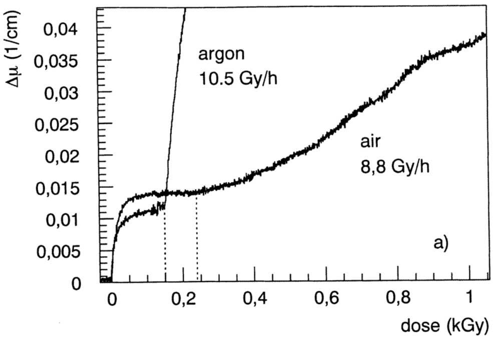

Figure 2.12: Comparison of the induced absorption $\Delta\mu(\lambda = 580\,\mathrm{nm})$ due to the irradiation of a BCF-12 fibre in air and in argon with 100 keV X-rays [21].

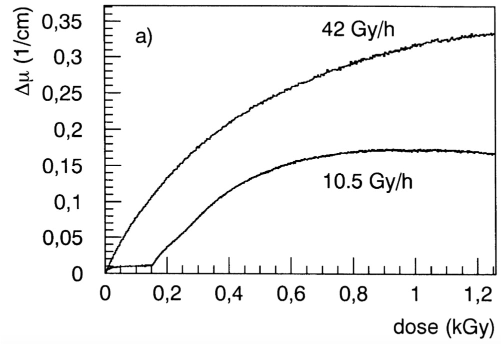

Figure 2.13: Induced absorption $\Delta\mu(\lambda = 580\,\mathrm{nm})$ during the irradiation of a BCF-12 fibre in argon with 100 keV X-rays [21].

Chapter 3

The LHCb detector and its upgrade

The LHCb experiment [35], one of the four major experiments at the LHC, will be upgraded during the Long Shutdown 2 of the LHC [8]. This chapter introduces the Standard Model of particle physics and the current LHCb detector. The physics program at LHCb, which motivates the detector's upgrade, is briefly presented, followed by a concise overview of the strategy for each subsystem's upgrade. The SciFi Tracker, on which this thesis project is focused, is discussed in more detail at the end of the chapter.

3.1 The Standard Model of particle physics

The Standard Model (SM) [36–38] was conceived in the late 1970s, combining the results of experiments and theoretical studies in the field of particle physics. It describes the fundamental particles and their interactions. According to the SM the matter is composed by three types of elementary particles: leptons, quarks and gauge bosons.

Quarks and leptons are fermions with spin 1/2. There are six leptons (electron, muon, tau and their corresponding neutrinos) and six quarks (up, down, charm, strange, top, also called truth, and bottom, also known as beauty). To each fermion corresponds an anti-fermion, with identical mass and lifetime, but with the signs of all the quantum numbers reversed.

Leptons and quarks are further divided into three generations, displayed in Table 3.1, where each generation consists in an electrically charged lepton and a neutrino or in a up-type and a down-type quark. Whilst all fermions undergo electromagnetic (excluding neutrinos, which are electrically neutral), weak and gravitational interactions, only quarks feel the strong force.

Forces are mediated by the gauge bosons, which are vectors of spin 1. The photon is the mediator of the electromagnetic interaction, the Z and W's (W^+ and W^-) of the weak force and the gluons of the strong force.

A final fundamental particle predicted by the Standard Model, a scalar boson

	Leptons						Quarks					
Generation	I		II		III		I		II		III	
Particle	e	ν_e	μ	ν_μ	τ	ν_τ	u	d	c	s	t	b
Q	-1	0	-1	0	-1	0	2/3	-1/3	2/3	-1/3	2/3	-1/3

Table 3.1: Leptons and quarks and their electrical charge Q.

with spin 0, is the Higgs boson. Its recent discovery at the LHC [39, 40] marked a big triumph for the the SM, according to which the Higgs boson is responsible for the particles' masses through the so-called Higgs mechanism.

The Standard Model has proved to be a solid representation of the nature which surrounds us. The validity of its predictions were successfully observed in several occasions through experimental tests. It is however clear that the SM does not yet depict the whole picture. For instance it does neither include gravity, nor explain the dark matter or the asymmetry between matter and anti-matter. Many theories were developed to extend the SM in an attempt to answer the remaining open questions. At the same time a big effort is being put to experimentally test with progressively increasing precision the limits of the Standard Model and/or possibly discover effects of some New Physics beyond it. Some experiments, as for instance ATLAS and CMS, try to achieve this results through on-shell production of new particles. The complementary approach of LHCb is to search for New Physics by accurately measuring processes that are precisely predicted in the Standard Model.

3.2 The LHCb detector

The main goal of the LHCb experiment is the search of physics beyond the Standard Model in the beauty and charm sector. The data collected and analysed with the LHCb detector are the results of high-energetic proton-proton collisions. The accelerated protons collide inside the Large Hadron Collider (LHC) at CERN [41, 42].

At the LHC the beauty quarks are predominantly produced in the same forward or backward direction. This is the reason why the LHCb detector was designed as a single-arm spectrometer with a forward angular coverage in the pseudo-rapidity range of $2 < \eta < 5$. A sketch of the LHCb detector with its subdetectors is shown in Fig. 3.1. The Vertex Locator (VELO) is a silicon vertex detector that surrounds the interaction region where the proton-proton collisions take place. Together with the VELO, the tracking system is based on a silicon strip detector (TT) and on the three tracking stations (T1 - T3), which combine silicon strip detectors in the high η region and straw drift chambers in the low η region. The TT and the stations T1 - T3 are located respectively in front and behind a 4 Tm dipole magnet. The particle identification relies on two Ring Imaging Cherenkov (RICH) detectors, one electromagnetic and one hadronic calorimeter and finally

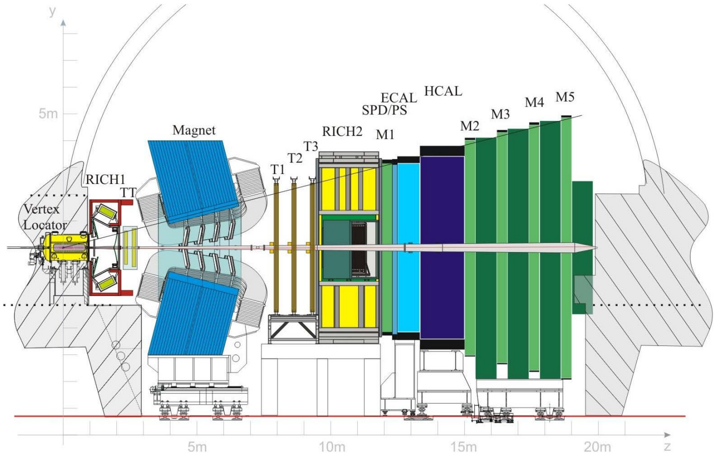

Figure 3.1: Layout of the LHCb detector [35].

on muon stations (M1 - M5).

During Run 1 of the LHC (2010 - 2012) the LHCb detector has collected data produced by pp collisions at a centre-of-mass energy of $\sqrt{s} = 7\,\text{TeV}$ (in 2010 and 2011) and $\sqrt{s} = 8\,\text{TeV}$ (in 2012), corresponding to a total integrated luminosity of $3\,\text{fb}^{-1}$. After the first Long Shutdown, the LHC restarted operations in 2015. Currently Run 2 is ongoing, with the LHC operating at $\sqrt{s} = 13\,\text{TeV}$. In September 2017 it was announced that the milestone corresponding to $6\,\text{fb}^{-1}$ of collected data had been hit [43]. At the end of 2018 the total integrated luminosity over the whole period 2010 - 2018 is expected to reach $8\,\text{fb}^{-1}$.
The detector operated at a maximum instantaneous luminosity of $4 \cdot 10^{32}\,\text{cm}^{-2}\text{s}^{-1}$. It has produced a wide range of remarkable results for particle physics. Nevertheless most results on key observables sensitive to physics beyond the Standard Model are statistically limited. A detector upgrade is needed to significantly go further in precision.

3.3 Highlights of LHCb achievements and upgrade prospects

The study of the properties of beauty and charm hadrons is a major focus of the LHCb detector. The analysis of the data collected by LHCb during its first years of operations provided significant results for particle physics. To mention some examples, a big success was the first evidence, published by LHCb, of the very rare decay $B_s^0 \to \mu^+\mu^-$ [44], followed by the first observation of this decay in the combined data analysed by the CMS and LHCb collaborations [45]. The probability, or branching fraction, of the B_s^0 meson to decay into a muon pair is very well-predicted and very small in the Standard Model: $\mathcal{B}(B_s^0 \to \mu^+\mu^-)_{SM} = (3.66 \pm 0.23) \cdot 10^{-9}$. Significant modifications of this observable are to be found in several extensions of the Standard Model, which

makes the decay $B_s^0 \to \mu^+\mu^-$ an interesting candidate to search for deviations from the SM. The experimental challenge is given by the rarity of the decay, so that no evidence of it could be found by any experiment before the LHC started operations. The value measured by the CMS and LHCb collaborations, $\mathcal{B}(B_s^0 \to \mu^+\mu^-) = (2.8^{+0.7}_{-0.6}) \cdot 10^{-9}$, is statistically compatible with the prediction of the Standard Model and allows to place stringent constraints on other theories. Another milestone hit by the LHCb collaboration was the observation of pentaquark-states, i.e. particles composed of five quarks [46]. Although such particles were already proposed in 1964 by Gell-Mann [47], the previous claimed discoveries turned out to be spurious [48].
An extensive description of the physical achievements of LHCb with the data collected during Run I of the LHC can be found in Ref. [49]. A more complete review is constantly updated on the public web page of the experiment[1]. The results obtained prove the power of LHCb as a tool to precisely test the Standard Model and potentially attest the existence of New Physics effects in deviations from the SM predictions.

The planned upgrade of the LHCb detector will allow to significantly increase the sensitivity on various physical observables. A central point of the upgrade is the substitution of the current trigger with a highly flexible software-based trigger. This will increase the readout rate capability from the current 1 MHz to the maximum LHC bunch-crossing frequency of 40 MHz. Furthermore it will significantly improve the trigger efficiency for a broad range of physics channels, allowing to extend the physics reach of the LHCb experiment. An example is the decay $B_s^0 \to \phi\phi$. The amplitude of this decay is suppressed in Standard Model, which makes it an interesting candidate to search for effects not predicted by the SM. The trigger efficiency on this decay after the upgrade is expected to be increased by a factor 4 with respect to Run I [50].

3.4 The upgrade of the LHCb detector

The upgraded LHCb detector is designed to collect at least $50\,\mathrm{fb}^{-1}$ at an instantaneous luminosity of $2 \cdot 10^{33}\,\mathrm{cm}^{-2}\mathrm{s}^{-1}$ and with a readout rate of 40 MHz [8]. The schedule with the luminosity evolution for the current and upgraded LHCb detector is shown in Table 3.2.

The trigger

The first selection in the current LHCb trigger is provided by a hardware trigger based on informations such as transversal energy and transversal momentum [35]. The hardware trigger has a maximum readout rate of 1 MHz, which is one of the main limitations of the current detector. As shown in Fig. 3.2, with the current

---

[1] LHCb public page: http://lhcb-public.web.cern.ch/lhcb-public/

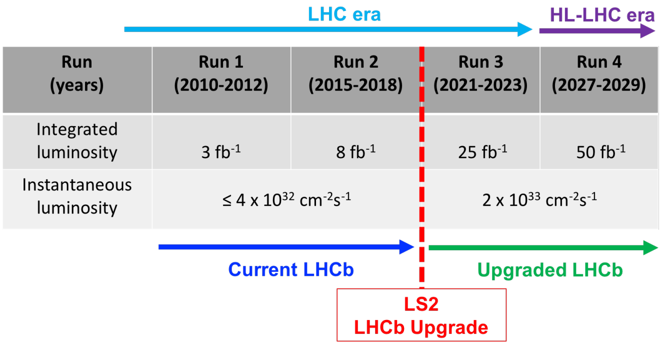

Run (years)	Run 1 (2010-2012)	Run 2 (2015-2018)	Run 3 (2021-2023)	Run 4 (2027-2029)
Integrated luminosity	3 fb^{-1}	8 fb^{-1}	25 fb^{-1}	50 fb^{-1}
Instantaneous luminosity	$\leq 4 \times 10^{32}\ \mathrm{cm}^{-2}\mathrm{s}^{-1}$		$2 \times 10^{33}\ \mathrm{cm}^{-2}\mathrm{s}^{-1}$	

Table 3.2: Schedule and luminosity evolution for the LHCb detector.

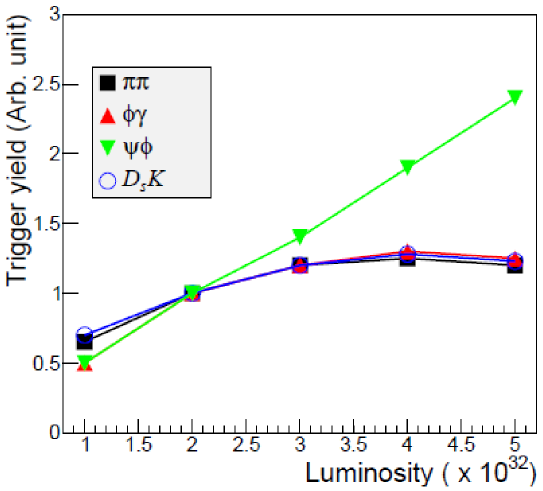

Figure 3.2: Trigger yield of the current trigger as a function of the luminosity for different decay channels [50].

trigger an increase in luminosity corresponds to a saturation in signal yields for hadronic channels. In order to overcome this obstacle a new full software trigger will be used [50]. The upgraded trigger will be able to process the full event information, having access to variables which are more discriminating than the transverse energy, like the impact parameter of tracks originating from a secondary vertex. This requires reading out the whole detector at 40 MHz. As a consequence, the font-end electronics of all the subdetectors must be replaced.

Particle Identification

The overall structure of the two RICH detectors will remain unchanged in the upgrade [51]. Nevertheless the currently used Hybrid Photon Detectors need to be replaced, since the 1 MHz readout electronics is embedded within the tube. It was chosen to substitute them with Multianode Photomultipliers with external readout electronics. Furthermore the optical layout of RICH1 will be modified in order to reduce the hit occupancy. This will be achieved by increasing the focal length of the spherical mirrors.

The calorimeters and muon system will only undergo minor changes during the upgrade, because the active elements do not need to be replaced. Since their main purpose in the current detector is to provide information for the hardware trigger, the Scintillating Pad Detector and the Preshower will be removed, which is expected to ease the calibration of the calorimeter system. The gain of the PMTs in the calorimeters will be reduced by a factor 5 in order to cope with the higher luminosity. In the muon system, because of the high particle flux, only the first of the five muon stations will be removed and an additional shielding will be installed around the beam pipe in front of the second station.

The Tracking System

The upgraded VELO [52] will surround the luminous region at LHCb and cover the full angular acceptance of the LHCb detector. It will consist of two retractable halves, each one composed by an array of 26 L-shaped silicon pixel sensors. The two halves will be moveable in order to protect the VELO during LHC injection or non-stable beams situations. The detector will be housed in a secondary vacuum, separated from the machine vacuum by a thin corrugated metal foil, called RF-foil. With respect to the current vertex detector the active region will be moved by 3 mm closer to the beam pipe, at a distance of 5.1 mm from the beam. The VELO will be exposed to an harsh radiation environment: in the innermost region it is expected to have accumulated an integrated flux of up to $8 \cdot 10^{15}\,\mathrm{n_{eq}/cm^2}$ after $50\,\mathrm{fb}^{-1}$. A cooling system is needed to prevent the silicon from thermal runaway effects due to irradiation and to cope with the ASIC power dissipation. The cooling will be achieved by evaporative CO_2 circulating within microchannels integrated in the L-shaped sensors.

The Upstream Tracker (UT) is the upgraded version of the TT detector [9]. It will be composed of four planes of silicon strip sensors, as the TT, but with higher segmentation. The two middle planes will be rotated by ±5° in order to perform stereo measurements. The finer granularity is needed in order to reduce the occupancy in the detector at upgrade conditions. Furthermore the UT will be moved closer to the beam pipe, consequently improving the small-angle acceptance.

3.4.1 The SciFi Tracker

The Scintillating Fibre (SciFi) Tracker [9, 53] will substitute the three current tracking stations T1 - T3. It will replace both the silicon strip detector and the straw drift chambers, covering the full acceptance after the magnet.

The active element in the SciFi Tracker will be plastic scintillating fibres, with a circular cross-section and a diameter of 250 μm. They will be wound into 2.4 m long, 13 cm wide and 1.35 mm high mats, composed by six layers of fibres as

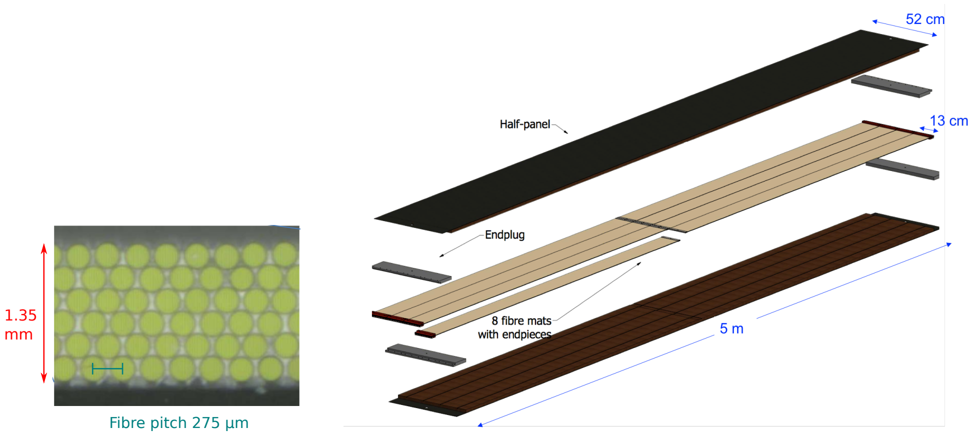

(a) (b)

Figure 3.3: (a) Cross section of a fibre mat. The fibres are arranged in a six-layer pattern with a pitch of 275 µm. The gap between the fibres is filled with glue. (b) Exploded view of a SciFi module composed by eight fibre mats, sandwiched between honeycomb panels. Pictures taken from [53].

shown in Fig. 3.3(a). Eight fibre mats, protected by 20 mm high honeycomb sheets laminated on the outer side with carbon-fibre skins, will be arranged to form a SciFi module (Fig. 3.3(b)). The SciFi Tracker will be composed by three stations, also called T1, T2 and T3, surrounding the beam pipe. They will be located between the magnet and the RICH2 detector as shown in Fig. 3.4(a). Each station will consist of four detection layers, with the two central layers of each station rotated by a stereo angle of $+5°$ and $-5°$, respectively. Each detection layer will be composed of 12 SciFi modules (Fig. 3.4(b)) with a material budget of $X/X_0 = 1.02\%$. The middle modules will be provided with a cut-out to allow the beam pipe to pass through the detector. A mirror will be glued on the fibres extremity close to the beam pipe, while on the other end the fibres will be read out by customised linear arrays of SiPM detectors (Hamamatsu, model H2016_HRQ). Each array will consist of 128 channels, built out of two 64 channel silicon dies arranged in one package as shown in Fig. 3.5. There is a 250 µm gap between the dies and a 400 µm gap between two detector arrays. Each fibre mat will be read out by four SiPM arrays. The detection principle is displayed in Fig. 3.6: a particle passing through the fibres produces scintillation photons, which propagate through the fibres to the photodetectors. Each of the 96 pixels in one SiPM channel can detect a photon and the channel signal is proportional to the total number of fired pixels. Signals in adjacent channels which pass a certain amplitude threshold are grouped together as clusters. The position of the particle can be calculated with a weighted mean of the channel signals.

The SciFi Tracker is required to have a hit detection efficiency higher than 98%, a spatial resolution of better than 100 µm in the bending plane and a low material budget of $X/X_0 \leq 1\%$ per detection layer. The modules performances were

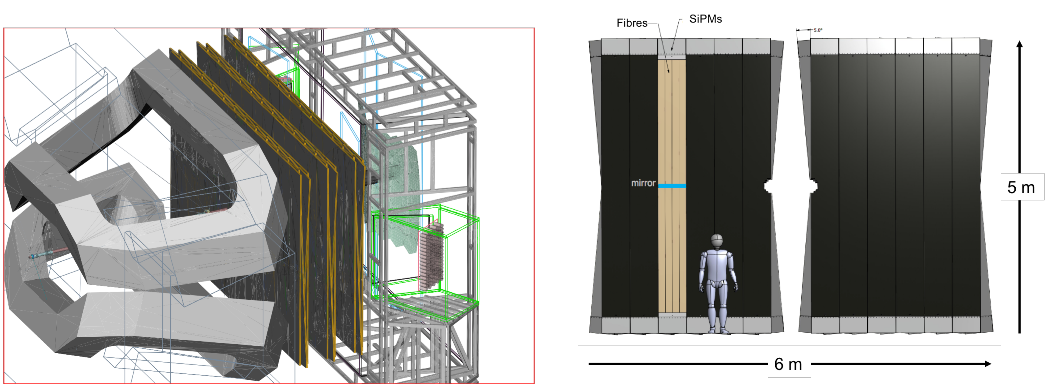

(a) (b)

Figure 3.4: (a) The location of the three stations composing the SciFi Tracker downstream of the magnet [9]. (b) Layout of one of the 12 SciFi detection layers [53].

evaluated during different testbeam campaigns (Fig. 3.7, [54]). A few additional testbeam campaignes took place since the publication of Ref. [54], although the results are not yet published. Furthermore, the SciFi Tracker is currently in the production phase and the light yield of each finished fibre mat or module is evaluated using a ^{90}Sr source. When the ionizing particles hit the fibres close to the mirror, the typical light collected by the SiPMs amounts to 16 - 20 photoelectrons. Such light yield values lead to a hit efficiency of $> 98.7\%$. The position resolution in the x-axis is better than 85 µm.

A plot of the hit efficiency as a function of the collected light is shown in Fig. 3.8 [55]. The efficiency at low light yield was evaluated using irradiated modules. A more detailed description of the modules irradiation tests and their result can be found in Chapter 7.

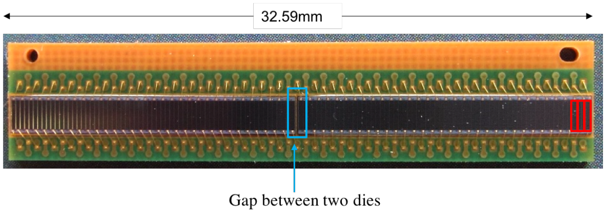

Figure 3.5: Package with 2 × 64 channels [9]. Some of the channels are highlighted in red, while the 250 µm gap between the dies is highlighted in blue.

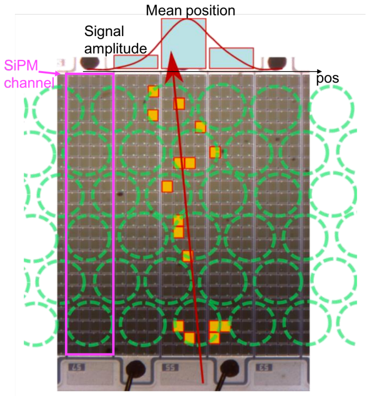

Figure 3.6: Detection principle of the SciFi tracker [9]. The fibres cross sections are indicated in green. The fired pixels are highlighted in yellow.

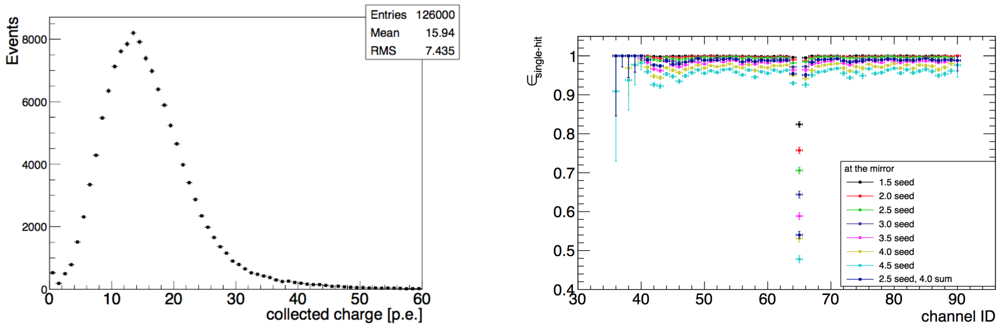

(a) (b)

Figure 3.7: Performances of the SciFi modules at the mirror [54]: (a) Collected charge distribution; (b) Hit detection efficiency for different threshold choices. The drop in the efficiency corresponds to the gap between the dies of one SiPM array.

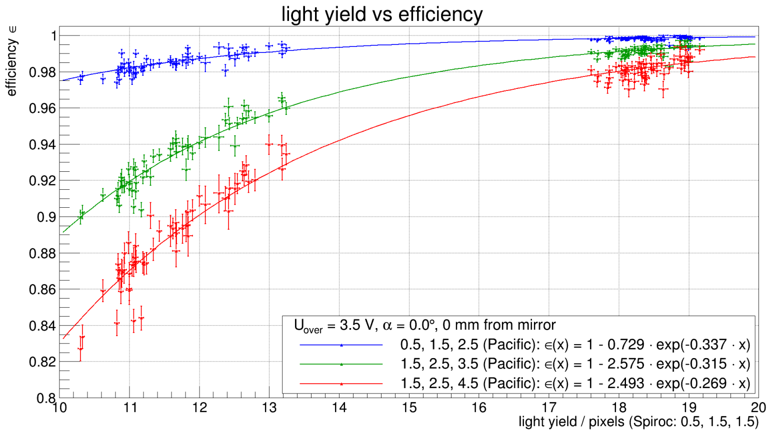

Figure 3.8: Hit efficiency as a function of the light yield [55]. Each curve correspond to a differently defined amplitude threshold.

Scintillating fibres

The SciFi Tracker will employ SCSF-78 scintillating fibres produced by Kuraray[2]. They have a multi-cladding structure with PMMA as inner cladding and a fluorinated polymer as outer cladding. The thickness of each cladding is 3% of the total diameter. They are based on a polystyrene core, doped with p-Terphenyl as activator and presumably TPB as wavelength shifter. They emit in the blue region of the visible spectrum, with a maximum intensity at $\lambda = 430\,\text{nm}$ (Fig. 3.9). Photons with different wavelengths are not equally attenuated when travelling through a scintillating fibre. In particular, photons with smaller wavelengths have enough energy to excite electronic transitions and are therefore more easily absorbed than photons with higher wavelengths. This effect can be clearly seen

---

[2] Kuraray catalogue: http://kuraraypsf.jp/psf/index.html

from the absorption spectrum of polystyrene (Fig. 2.2). The emission spectrum of a fibre is therefore shifted towards longer wavelengths when the distance between excitation point and photodetector increases. Most of the particles created from proton-proton collisions at the LHC will hit the fibres at a distance of about 2.5 m from the photodetectors. The emission spectrum of SCSF-78 fibres at 2.5 m peaks at 450 nm, nicely matching with the PDE distribution of the SiPMs. The spectral resolved attenuation length of a SCSF-78 fibre is shown in Fig. 3.10. It increases from about 2 m at 440 nm, to more than 10 m for photons with $\lambda > 500$ nm. The absorption spectrum of polystyrene (Fig. 2.2) also shows several peaks in correspondence with vibrational levels at $\lambda \sim 535$ nm, $\lambda \sim 570$ nm, $\lambda \sim 610$ nm, $\lambda \sim 650$ nm, $\lambda \sim 710$ nm and $\lambda \sim 760$ nm. The enhanced absorption in the PS-based SCSF-78 fibres at $\lambda = 535$ nm, $\lambda = 570$ nm and $\lambda = 610$ nm is clearly visible in Fig. 3.10.

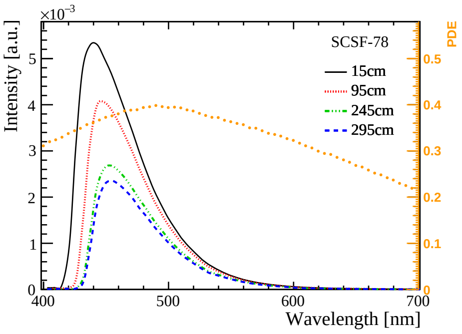

Figure 3.9: Emission spectra of a SCSF-78 fibre at distances of 15 cm, 95 cm, 245 cm and 295 cm, respectively, from the spectrometer. The photodetection efficiency of the SiPMs is also shown [9].

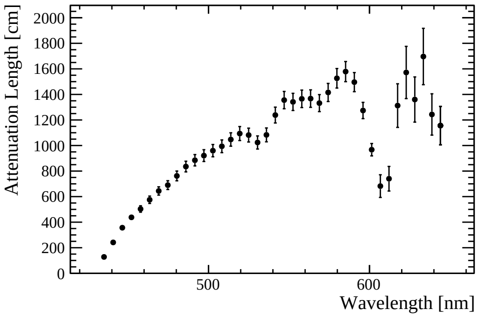

Figure 3.10: Attenuation length of a SCSF-78 fibre as a function of the photon wavelength [9].

Radiation environment

When packed inside the operating SciFi Tracker, the fibres will have to withstand a very harsh environment. A study of the radiation levels in LHCb after an integrated luminosity of 50 fb^{-1} at upgrade conditions [56] was performed using a Fluka [57, 58] simulation of the LHCb detector. The resulting dose distribution is shown in Fig. 3.11. The maximum dose will be registered close to the beam pipe and will amount to 35 kGy. Moving away from the beam pipe region, the dose will rapidly decrease till a value of 40 Gy in the SiPMs region.

Several dedicated irradiation campaigns were performed in order to test the ageing of the SCSF-78 fibres as a function of the dose. Fibres were irradiated at different facilities up to different doses. A summary of all the performed irradiation tests is outlined in Tables 3.3 and 3.4. A spectral analysis including all the irradiation experiments on single fibres or fibre bundles (also those described

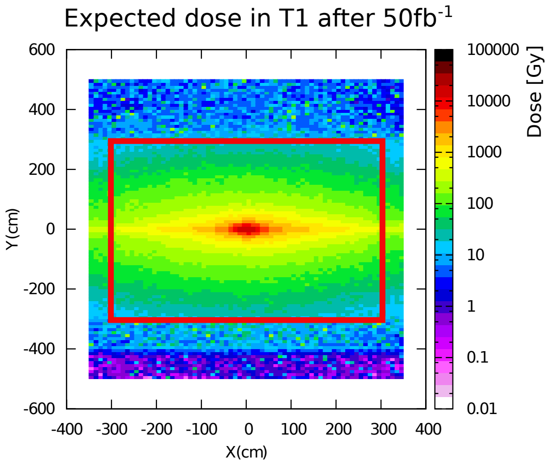

Figure 3.11: Dose distribution in the T1 plane after an integrated luminosity of 50 fb^{-1} [9]. The (0,0) coordinates correspond to the beam pipe position. The red frame represents the edges of the SciFi station.

in Chapter 6) was performed [61]. The best prediction for the induced absorption of photons emitted at 450 nm is $\alpha_{\text{rad}}(D) = 0.004 \cdot D^{0.8}$, with the dose D in kGy and α_{rad} in cm^{-1}. The simulation predicts a signal loss of about 40% at the end of the SciFi's lifetime in the most irradiated region.
To test this prediction a full SciFi module was irradiated in the PS synchrotron with the same LHCb dose profile (see Chapter 7). The expected signal loss of 40% was confirmed.

As previously mentioned the typical light yield of unirradiated modules at the mirror amounts to 16 - 20 photoelectrons. The best performant modules will be selected to be placed in the central region of the SciFi Tracker, where the dose is higher. Therefore after 10 years of operation at the mirror, i.e. in the most irradiated region, a light yield of 12 photoelectrons is expected. The effect on the hit efficiency can be seen in the plot in Fig. 3.8. The hit efficiency at 12 photoelectrons can vary between about 90% and about 99% depending on the selected threshold.

Facility/ Ref.	**Dose** [kGy]	**Dose rate** [Gy/h]	**Short description**
PS, CERN. [9,59]	3, 22	$2.25 \cdot 10^4$, $5.0 \cdot 10^3$	Eight 2.94 m long fibres were glued on a plexiglass support and irradiated with 24 GeV protons. The layout was chosen such that the first 150 cm of the fibres were not irradiated. The immediately following 75 cm long section was exposed to 3 kGy with a dose rate of 22.5 kGy/h. The last section, also 75 cm long, absorbed 22 kGy with a dose rate of 5 kGy/h.
KIT, Karlsruhe. [9,60]	9, 10, 18, 37, 43, 60	$1.8 \cdot 10^6$	Fibre bundles were glued on different PVC boards. The fibres in each bundle had a length of 200 cm and 40 cm, respectively. They were exposed to 23 MeV protons with a dose rate of $1.8 \cdot 10^6$ Gy/h. Different sections of the fibres were irradiated up to different doses in the range 9 to 60 kGy.
MLL, Garching. [61]	100	$4 \cdot 10^4$	Four 50 cm long fibres were arranged on a support made of foam. The central region of the fibres was exposed to 21 MeV protons over a length of 5 cm. The total dose was 100 kGy and the dose rate 40 kGy/h.
AAA/ CERN. [62]	0.34	$2 \cdot 10^1$	A 3 m long fibre was placed in a tube surrounded by fludeoxyglucose (^{18}F), a radioactive liquid usually used in positron emission tomography provided by the company AAA[3]. It emits low energy β^+ ($E \leq 634$ keV) and consequent 511 keV gammas.
LHCb cavern. [9,61]	0.23, 0.26, 1.0	$\sim 10^{-2}$	Three sets of 1.1 m long fibres were glued to different supports and placed in the LHCb cavern. They were exposed to multi-GeV hadrons. The average dose absorbed by each fibre set along its length was 0.23, 0.26 and 1.0 kGy, respectively.

Table 3.3: Summary of irradiation tests on SCSF-78 fibres performed in previous works from the SciFi group.

[3] Advance Accelerator Applications, 20 Rue Diesel, 01630 Saint Genis Pouilly, France.

Facility/ Ref.	**Dose** [kGy]	**Dose rate** [Gy/h]	**Short description**
LHCb Tunnel. Chapter 6 of this thesis	3.3	$2 \cdot 10^{-1}$	Two fibre bundles were glued on a light support and placed in the LHCb tunnel close to the beam pipe. They were exposed to mostly multi-GeV hadrons up to a dose of 3.3 kGy.
^{106}Ru Uni DO Chapter 6 of this thesis	$3.5 \cdot 10^{-2}$, $3.8 \cdot 10^{-2}$, $5.0 \cdot 10^{-2}$, $5.6 \cdot 10^{-2}$, $6.9 \cdot 10^{-2}$, $7.3 \cdot 10^{-2}$	$6.6 \cdot 10^{-2}$, $7.2 \cdot 10^{-2}$, $9.0 \cdot 10^{-2}$, $10.2 \cdot 10^{-2}$, $12.6 \cdot 10^{-2}$, $13.2 \cdot 10^{-2}$	Nine 7 m long fibres were wound on a plastic wheel. Three fibres were not irradiated and used as reference fibres. The other six fibres were exposed to β particles emitted from ^{106}Ru ophthalmic plaques. (Max. β energy: 3.5 MeV, mean β energy: 1.4 MeV).
Module irradiation, PS, CERN. Chapter 7 of this thesis	SciFi dose profile	10^3 - 10^4	A SciFi module was exposed to 24 GeV protons to a dose profile similar to the one in the real SciFi Tracker. The module's performances were evaluated before and after the irradiation in test beam campaigns and in the lab with a ^{90}Sr source.

Table 3.4: Summary of irradiation tests on SCSF-78 fibres performed within the framework of this thesis project.

Chapter 4

Quality assurance tests

The scintillating fibres for the SciFi detector are produced by the Japanese company Kuraray. Over 10′000 km of fibres are to be delivered to CERN in the period from May 2016 to January 2018. They are periodically delivered with the following schedule: from May 2016 to August 2016 in batches of 100 km every week (start of production), and from September 2016 in batches of 300 km every two weeks (full production mode). Every batch is composed by 8 (start of production) or 24 (full production) spools of 12.5 km fibres each.
The fibres are carefully and systematically inspected before being assembled into SciFi modules. This chapter describes the tests performed to monitor the quality of the delivered fibres. In particular:

- the attenuation length
- the light yield
- the resistance to X-ray irradiation
- the diameter profile

are regularly measured for every batch. The most part of the setups used for quality assurance were already in use, projected and tested by the CERN SciFi group and, in the case of the diameter scanner, with the main contribution from the SciFi group in Aachen. Nevertheless, the equipment for the bump shrinking method and the validation of this procedure, the software to perform a fast measurement and analysis of the spectral attenuation length and the X-ray test were developed and set up within the framework of this thesis project.
The planned time schedule for the delivery is shown in the plot in Fig. 4.1, together with the progress of the quality assurance at CERN. At the time in which this thesis was written, the analysed fibres amounted to 6′700 km. Therefore the results presented in this chapter refer to 61% of the total ordered fibres.

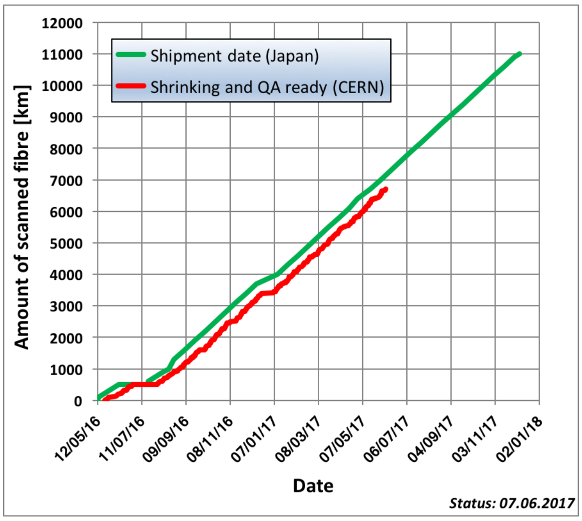

Figure 4.1: The planned time schedule for the delivery of 11′000 km scintillating fibres (green line) and the progress of the QA tests at CERN (red line).

4.1 Attenuation length

The setup to measure the attenuation length is described in Ref. [63]. A 3.5 m long fibre is tensed and held in position with magnetic soft rubber fixtures. The wavelength shifter inside the fibre is directly excited with four UV-LEDs emitting at the wavelength of 390 nm. The LEDs are symmetrically surrounding the fibre, hold in position by a box, which can be manually moved along a 3.5 m long optical bench. The fibre is readout at one extremity of the optical bench by a Si-PIN photodiode of type Newport 818-UV. The other extremity is covered with Aquadag[1] to absorb the photons and avoid rear reflection inside the fibre. The outer surface of the fibre close to the PIN diode is also covered with Aquadag over a length of a few centimetres in order to suppress photons travelling in the cladding. To ensure an even surface, the readout extremity of the fibre is cut with a guillotine-like cutter. A schematic of the setup is shown in Fig. 4.2.

A Labview program is used to save and plot the current measured by the diode at various distances between the excitation point and the photodetector. The same software also performs a fit to the resulting exponential curve and displays the value of the attenuation length. The whole procedure takes about 2 minutes and no further analysis is needed. This allows to measure the attenuation length for each spool.

Fig. 4.3 shows an example of a fit to extrapolate the attenuation length. The fitting curve is a single exponential $I(x) = I_0 \exp(-x/\Lambda)$, where $x \in [100\,\text{cm}, 300\,\text{cm}]$ is the distance from the photodetector, $I(x)$ is the intensity of the current recorded by the PIN diode and Λ the attenuation length. The fit ranges are chosen to avoid

---

[1] Aquadag (water based graphite coating) is an aqueous-based colloidal dispersion of ultra-fine graphite. Henkel Cooperation.

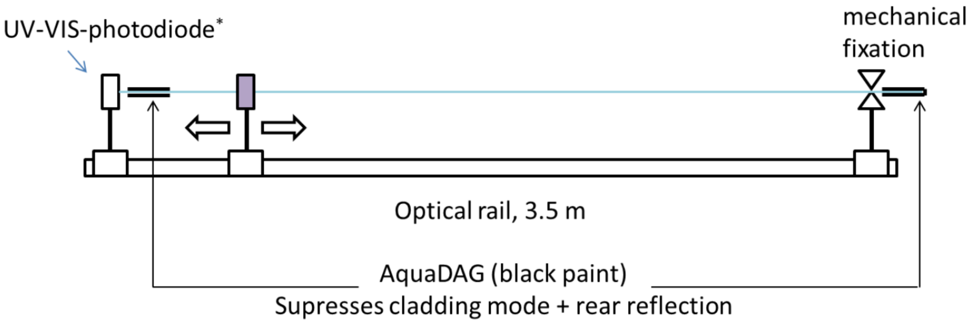

Figure 4.2: Seup to measure the attenuation length. Illustration taken from Ref. [63].

the contribution of a second exponential with shorter attenuation length due to losses of cladding light and to photons travelling with non-meridional trajectories inside the fibre. This steep exponential term has typical attenuation lengths of 20 - 30 cm, i.e. it is already sufficiently attenuated at 100 cm to be ignored.

The reproducibility of the attenuation length for the same 3.5 m long fibre sample was estimated to be 5%. It should be noted that the transmission of photons is affected by the geometry of the fibre, so it can vary along the 12.5 km long fibre which form a spool. Those variations were studied by measuring several 3.5 m long samples along a spool, and were found to be smaller than 10% per spool.

Since the fibres inside the SciFi tracker will be 2.5 m long, the requirement is that the attenuation length measures at least 300 cm. The average attenuation length after 61% of analysed spools is 351 cm, which is well above the required limit. An example of a plot displaying the attenuation length per spool is shown in Fig. 4.4.

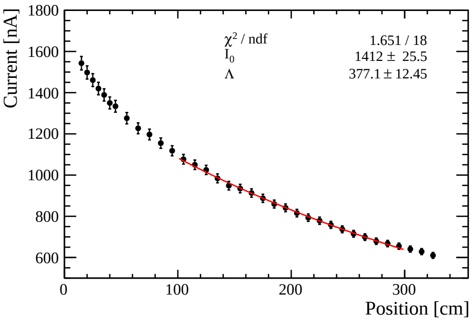

Figure 4.3: Example of a fit to extrapolate the value of the attenuation length.

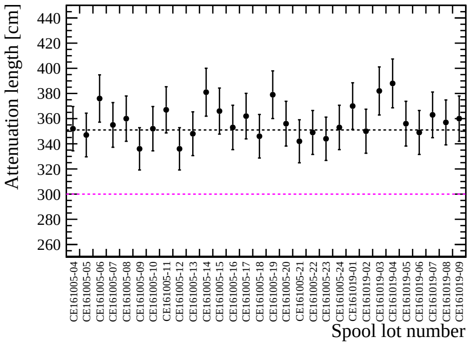

Figure 4.4: Attenuation length per spool. For clarity purposes only 30 spools are shown in this plot. The chosen subset is representative for all the tested spools. The magenta dashed line corresponds to the required limit of 300 cm agreed with the manufacturer. The black dashed line represents the average of 351 cm.

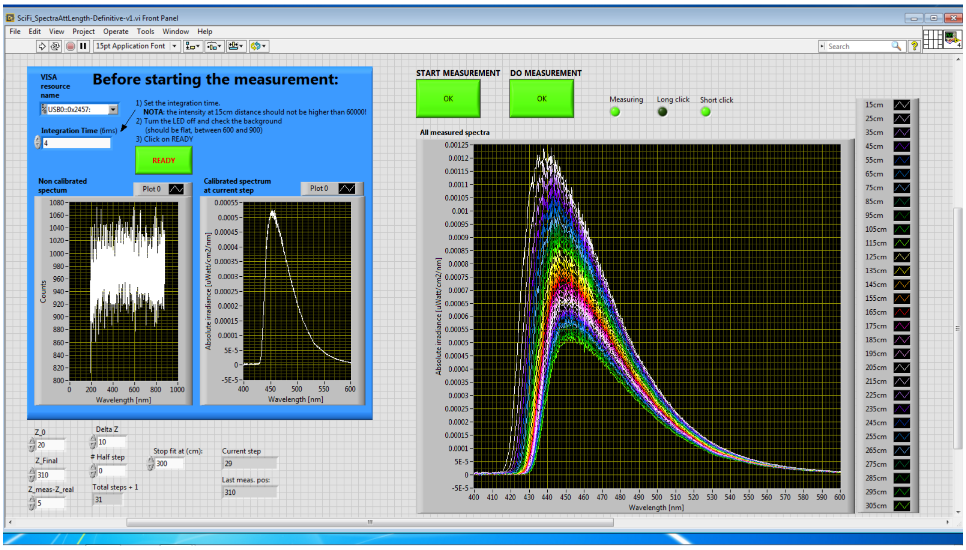
SciFi_SpectraAttLength-Definitive-v1.vi Front Panel

Before starting the measurement:

1) Set the integration time.
NOTA: the intensity at 15cm distance should not be higher than 60000!
2) Turn the LED off and check the background
(should be flat, between 600 and 900)
3) Click on READY

VISA resource name: USB0::0x2457:

Integration Time (6ms): 4

Z_0: 20

Z_Final: 310

Z_meas-Z_real: 5

Delta Z: 10

Half step: 0

Total steps + 1: 31

Stop fit at (cm): 300

Current step: 29

Last meas. pos: 310

Figure 4.5: Screenshot of the Labview program to measure the spectral attenuation length. On the right the emission spectra at different excitation points are displayed.

4.1.1 Spectral attenuation length

The spectral attenuation length is measured with the same setup described in the previous section, with a spectrometer of type Ocean Optics USB2000+UV-VIS-ES replacing the Si-PIN diode. The spectrometer is connected to the scintillating fibre via a clear fibre with a diameter of 1 mm. Since the numerical aperture of the fibre (NA = 0.72) is larger than the one of the spectrometer (NA = 0.22), a lens is added between the scintillating fibre and the clear fibre [64]. The emission spectrum of a 3.5 m long fibre is recorded at different excitation distances from the spectrometer. The attenuation length is then derived from exponential fits to the intensities measured with the spectrometer in wavelength bins of about 5 nm. The reproducibility of the spectral attenuation length for the same 3.5 m long fibre sample in the wavelength range 425 nm - 620 nm was estimated to be 3%.
With the help of the dedicated Labview program, the time needed to perform the measurement is about 2 minutes. A screenshot of the Labview program is shown in Fig. 4.5. The wavelength dependent attenuation length $\Lambda(\lambda)$ for a typical fibre sample is shown in Fig. 3.10 and discussed in Section 3.4.1.

4.2 Light yield

The setup, presented in detail in Ref. [65], is conceived to monitor the scintillation light yield and compare different fibre samples during the serial production phase of the SciFi detector. A fibre is locally excited with energy filtered 1 MeV electrons from a ^{90}Sr source. Contrarily to UV light, which only excites the wavelength shifter, a minimum ionizing particle, like a 1 MeV electron, triggers the full scintillation process. The excitation points are at well defined distances from the

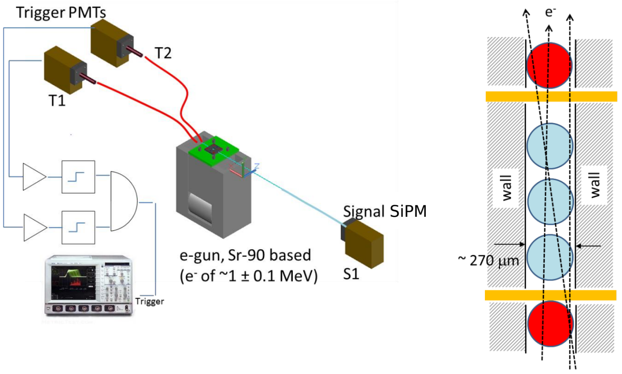

Figure 4.6: Left: Main components of the scintillation yield setup. Right: Details of the arrangement of the trigger fibre (top and bottom in red) and the fibres under test in between. Figure taken from Ref. [65].

photodetector.

The light yield of a single scintillating fibre of 250 µm diameter is small. In order to increase the signal to noise ratio, the combined signal of three fibres is read out simultaneously. The scintillation light is detected by a silicon photomultiplier (SiPM of the type Hamamatsu S13360-1350CS). The main components of the setup and the arrangements of the fibres are shown in Fig. 4.6. The three signal fibres are piled up in a vertical stack on top of the radioactive source. Two trigger fibres, placed on top and on the bottom of the stack, are singularly read out by two Hamamatsu H7826 photomultiplier tubes (PMTs). The trigger signal is provided by the coincidence of the two PMTs. In this way it is ensured that the minimum ionizing β particle traversed all the three signal fibres. In order to achieve a good quality readout end cut, the signal fibres are glued together in a cylindrical plastic connector and then cut with a diamond milling tool. The other end is left unmachined. The whole setup is placed inside a dark room at an ambient temperature of about 22°C.

The signals are readout with a LeCroy LT344 digital oscilloscope, which samples the voltage pulses. After pedestal subtraction, the mean accumulated signal charge at a defined excitation distance is converted into photoelectrons (p.e.) using the well visible photoelectron peaks of the SiPM signals. The number of generated photoelectrons is plotted against the distance between excitation point and SiPM, resulting in an exponential curve. The scintillation light yield corresponds to the extrapolated value from the exponential fit at a distance $d = 0$. An example is shown in Fig. 4.7. The uncertainty associated to the extrapolated value for the light yield amounts to 4% of the value.

This method allows to determine the intrinsic light yield independently from the attenuation length of the fibres. On the other hand the light yield of a SciFi Module as measured from the test beams depends both on the intrinsic light yield and on the transport efficiency of the fibres. The light yield of a Module is therefore always quoted together with the distance between excitation point and photon detection (e.g. 16 photoelectrons at the mirror, see Section 3.4.1 and Fig.

3.7). The conceptual discrepancy between the quoted light yield for single fibres and SciFi Modules does not affect the validity of the QA setup, which allows to compare different fibres by performing a measurement under defined and stable experimental conditions.
The average light yield after 61% of analysed spools is 13.8 p.e., well above the required limit of 10 p.e. An extract of the measured light yield values as a function of the spool is shown in Fig. 4.8.

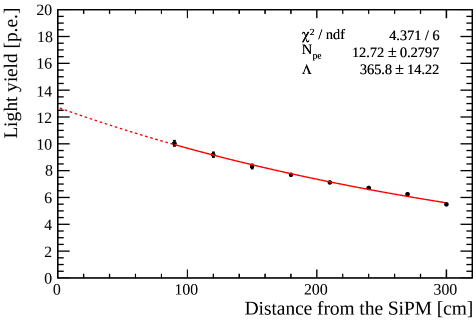

Figure 4.7: Example of a fit to extrapolate the value of the light yield.

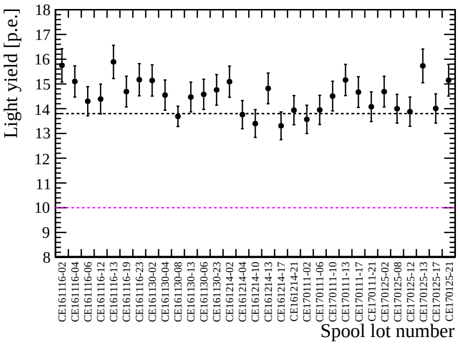

Figure 4.8: Light yield per spool. For clarity purposes only 30 spools are shown in this plot. The chosen subset is representative for all the tested spools. The magenta dashed line corresponds to the required limit at 10 p.e. The black dashed line represents the average of 13.8 p.e.

4.3 X-ray test

The X-ray irradiation test for the fibre QA is outlined in this section. Firstly, some initial tests are described (Section 4.3.1), which were performed with a setup already in use at CERN, in order to assess the effectiveness of X-ray tubes for our purposes. Given the positive outcome of these tests, an X-ray tube with a tungsten target was purchased and a customized setup for fibre QA was conceived and built. The customized setup, together with the results of the systematic irradiation tests, are presented in Section 4.3.2.

4.3.1 Feasibility studies on X-ray tubes for fibre QA

The production of X-rays in a tube is started by heating a filament to induce thermionic emission. The electrons are accelerated by the high voltage towards the anode material (target). X-rays are produced from the interaction of the accelerated electrons and the target. The mechanisms responsible for X-rays

generation are the bremstrahlung and the emission of characteristic radiation. The bremstrahlung is characterised by a continuum energy spectrum with the maximum achievable energy corresponding to the value of the high voltage, whereas the characteristic radiation has a well defined energy, characteristic of the target material. Therefore the accelerating voltage and the target material have an impact on the energy distribution of the emitted X-rays.
X-ray tubes are powerful tools for radiation hardness studies. They offer several advantages compared to other radiation sources. They are compact, easily accessible and easier to use than synchrotron beams. Contrary to α- and β-particles emitters, the intensity of the beam can be modulated, so that the object under test can be irradiated with a great variety of dose rates. The focused beam and the relative low energy, make them easier to shield than γ-ray sources.
The characteristics of X-ray tubes appoint them as interesting candidates for the quality assurance of the fibres during serial production of the SciFi Tracker. In the following, the dose rate measurements and the first experiments to test the effect of X-ray radiation on SCSF-78 scintillating fibres are described.

4.3.1.1 Copper target

The goal of this irradiation campaign was to answer the question if an X-ray tube would be an adequate radiation source for the quality assurance test. For this purpose we could use an X-ray tube with copper target already in operation at CERN[2], primarily used for ageing studies and stress tests of micro pattern gas detectors such as GEM and MircoMegas.

Dose rate

The dose rate was measured with a calibrated silicon diode[3] before starting the tests on radiation resistance of the fibres. During fibres irradiations the dose and dose rate were monitored with Gafchromic HD-810[4] films. In order to determine the dose rate, the measured quantities are the current produced in the silicon diode during irradiation and the colouration (optical density) of the films after exposition. Both these quantities can be converted into a value for the dose rate (diode) or dose (films) with a calibration factor.
The result given by the diode is immediate, therefore it could be used to perform several measurements in the time at disposal. A linearity scan of the X-ray tube as a function of high voltage and anode current was performed. The result, with the diode facing the beam outlet at a distance of 0.5 cm from the tube, is shown in Fig. 4.9. The dose rate in SiO_2 is obtained multiplying the current by a conversion factor $k = 22.88 \cdot 10^{-2}\,\mathrm{Gy} \cdot \mathrm{min}^{-1} \cdot \mathrm{nA}^{-1}$. There might be however some uncertainty coming from the fact that the diode was calibrated with higher energy photons.

---

[2] E. Olivieri, L. Ropelewski, CERN, EP-DT department.

[3] Quantrad PIN diode, provided by F. Faccio, CERN, EP-ESE department.

[4] http://www.gafchromic.com/

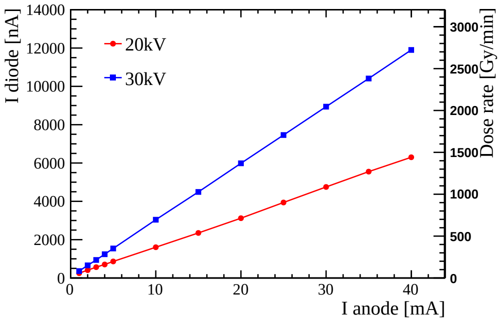

Figure 4.9: Current induced in a silicon diode facing the beam outlet at a distance of 0.5 cm as a function of different settings of an X-ray tube with Cu target. The right axis shows the dose rate in SiO_2.

Setup

A PANalytical[5] X-ray tube with a copper target was placed in a shield produced by the company Italstructures (now GNR)[6]. The shield was provided with a mechanical outlet in correspondence with the X-ray beam. The tube was connected to a power supply (model COMPACT 3K5 by Italstructures), capable to deliver a tunable high voltage of up to 60 kV and current of up to 60 mA. A closed hydraulic circuit was connected to the tube, to cool the Cu target during irradiation. The whole setup was placed in a custom made shielding box with copper walls.

The beam spot was a circle with a diameter of 13 mm. In order to irradiate a fibre over its whole length of 3.5 m, the sample under test was coiled inside a teflon tube around a plastic wheel with a diameter of 15 cm. The plastic wheel was connected to a motor and rotated with constant speed during the whole irradiation. The wheel was positioned in front of the tube, so that the fibre was at 1 cm distance from the beam outlet. A sketch and pictures of the setup can be seen in Fig. 4.10.

The energy spectrum of the X-rays emitted by a tube with Cu target peaks at 8 keV because of the characteristic K lines for copper atoms (4.11, [66]). The mass attenuation coefficient of teflon for 8 keV photons is $\mu/\rho = 13.27\,\mathrm{cm}^2/\mathrm{g}$ [67]. The intensity of the X-ray beam before impinging on the fibre was

$$\mathrm{I}(t = \rho x) = \mathrm{I}_0 \cdot e^{-\frac{\mu}{\rho} \cdot t} = 0.23 \cdot \mathrm{I}_0 \qquad (4.1)$$

where $x = 0.5\,\mathrm{mm}$ is the thickness of the teflon tube, $\rho = 2.2\,\mathrm{g/cm}^3$ is the density of teflon and I_0 is the intensity of the X-ray beam before travelling through the teflon.

In this layout some sections of the fibre shield other sections as illustrated in

---

[5] http://www.panalytical.com

[6] http://www.gnr.it

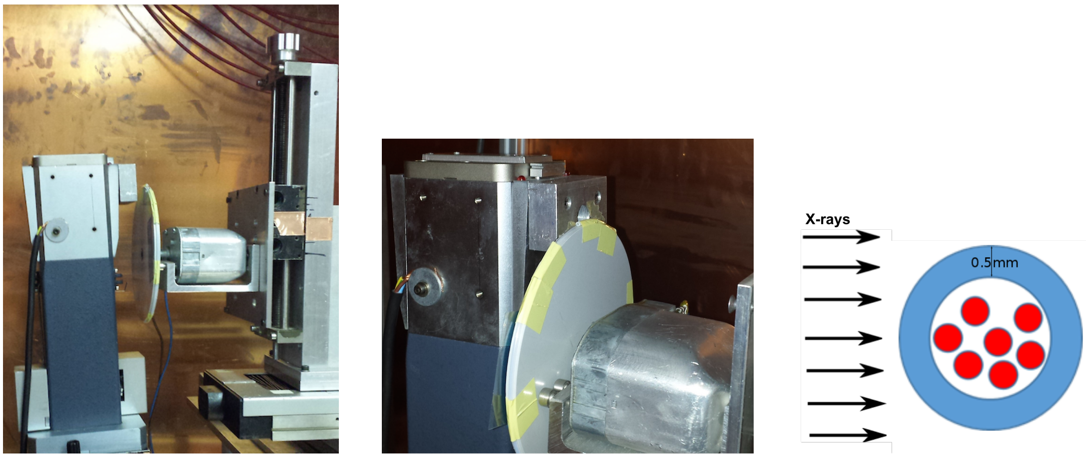

Figure 4.10: Pictures of the setup to irradiate a fibre sample with X-rays from a tube with Cu target. On the right a sketch of the cross-section of the teflon tube (in blue) containing the fibre sample (in red) is shown.

the sketch in Fig. 4.10. The mass attenuation coefficient of polystyrene for 8 keV photons is $\mu/\rho = 4.252\,\mathrm{cm}^2/\mathrm{g}$ [67], therefore a 0.25 mm diameter fibre dim the beam by about 10%. Thus, a non-uniformity in the absorbed dose of about 30%, due to the attenuation in the fibre itself should be taken into account.

Dosimetry was carried out with Gafchromic HD-810 films, attached to the teflon tube during irradiation. They consist of an active layer, approximately 6.5 µm thick, coated on a clear, transparent 97 µm thick polyester sheet. When irradiated, the active component in the dosimetric film reacts to form a blue coloured polymer and the optical density of the film is proportional to the absorbed dose as shown in Fig. 4.12. It should be noted that the calibration curve is valid for high energy photons above approximately 0.2 MeV. It was reported that the energy response of the films decreases by approximately 30% when the effective photon energy is reduced from 1710 keV to 28 keV (Fig. 4.13, taken from Ref. [68]). Most of the X-rays generated in this setup have an energy of 8 keV. The response of HD-810 for energies smaller than 28 keV is not given in Ref. [68]. Therefore a 30% correction is applied to the dose estimated from the curve in Fig. 4.12, but the presence of a systematic error on the dose evaluation can not be excluded.
Pictures of dosimetric films after irradiation are shown in Fig. 4.14: the reduced intensity of the X-ray beam after traversing the teflon and the fibre is immediately clear. The optical densities, measured with a Model 37-443 Nuclear Associates densitometer[7], confirmed the extent of the absorption assumed from the theory.

Radiation tests

Three 3.5 m long fibre samples were exposed to X-ray radiation. The attenuation length of each sample was measured before and after the exposure. The three

---

[7] http://www.flukebiomedical.com

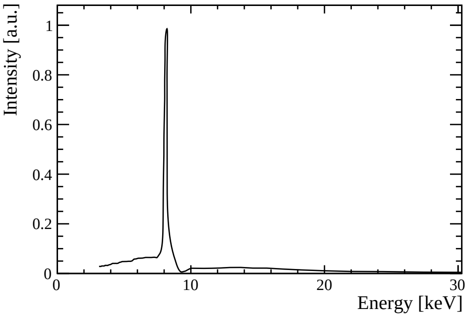

Figure 4.11: Energy distribution of the X-rays emitted by a tube with a copper target. Data taken from [66], modified.

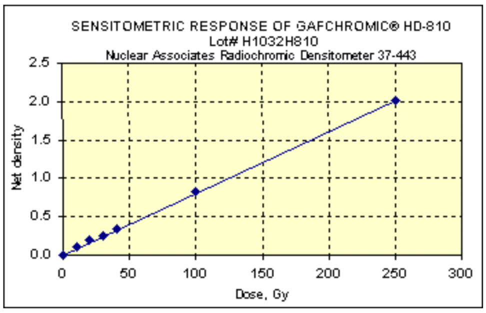

Figure 4.12: Optical density as a function of the dose for Gafchromic HD-810 dosimetric films. Picture taken from the films data sheet, www.gafchromic.com.

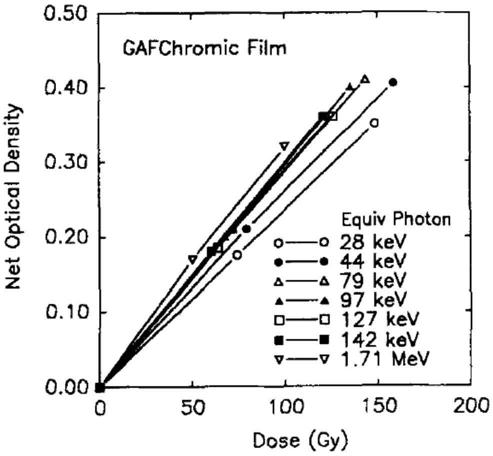

Figure 4.13: Energy response of Gafchromic HD-810 films [68].

samples were irradiated with different tube settings, i.e. different dose rates, and up to different doses. The details of each irradiation were:

Sample 1). Tube: 20 kV, 10 mA. Dose rate: 0.5 Gy/min. Dose: 43 Gy

Sample 2). Tube: 20 kV, 20 mA. Dose rate: 0.8 Gy/min. Dose: 67 Gy

Sample 3). Tube: 30 kV, 40 mA. Dose rate: 3.5 Gy/min. Dose: 415 Gy

The doses and dose rates quoted here are referred to the radiation absorbed by the fibre over its whole length, after the teflon shielding.

No effect could be seen for the samples 1) and 2). In the third sample a degradation of

$$\Lambda'/\Lambda_0 = 0.83 \pm 0.06, \qquad \alpha_{\mathrm{rad}} = (0.5 \pm 0.2) \cdot 10^{-3}\,\mathrm{cm}^{-1}$$

was measured, where Λ_0 is the attenuation length before and Λ' is the attenuation length after the irradiation. The additional absorption induced by the irradiation is defined as $\alpha_{\mathrm{rad}} \equiv \alpha' - \alpha_0 \equiv \Lambda'^{-1} - \Lambda_0^{-1}$.

The samples were stored in a dark room with a constant temperature of 22°C.

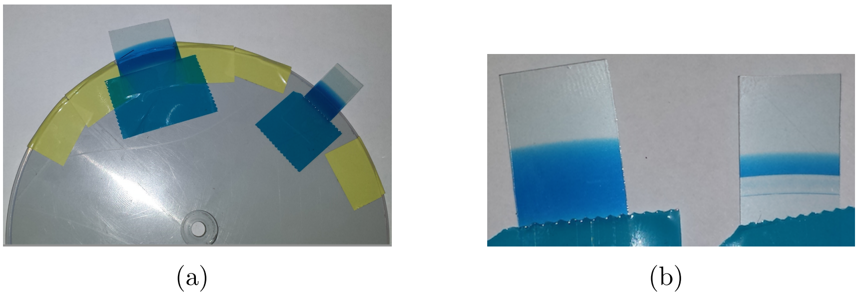
(a)

(b)

Figure 4.14: (a) Pictures of the Gafchromic HD-810 films attached on the plastic wheel during irradiation. (b) The film on the left was taped between the X-ray tube and the teflon tube, while the film on the right was fixed behind the teflon tube.

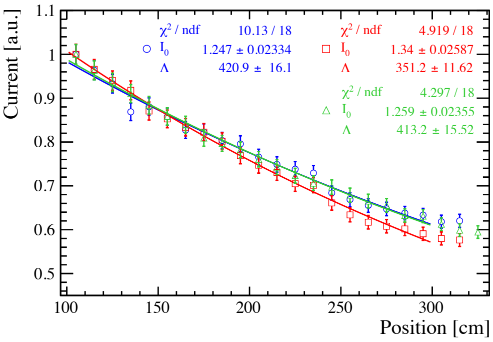

Figure 4.15: Attenuation length of a fibre before (blue circles), 20 minutes after (red squares) and three months after irradiation (green triangles). The irradiation was performed with an X-ray tube with Cu target up to a dose of 415 Gy.

Three months later, when the attenuation length was measured again, sample 3 had completely annealed (Fig. 4.15). To attest the repeatability of this result the annealing of six other fibre samples was studied. Five samples, irradiated to a dose of 1 kGy, recovered within one month from the irradiation. The last sample was exposed to a dose of 10 kGy and still showed a significant reduction of the attenuation length two months after irradiation. More details about these tests can be found in Section 5.2.3.

Discussion

The measurements performed with the Cu target X-ray tube showed that this technology is indeed a suitable choice for the quality assurance tests. The tunable dose rate is high enough to allow high throughput. The damage induced in the fibre after only 400 Gy is measurable with our equipment.
A copper target is however not adequate because the low energy emitted photons induce non-uniformities in the absorbed dose. A molybdenum or tungsten target would be more suitable since higher voltages of 20 - 60 kV are easily reachable.

Furthermore the layout for fibres irradiation need to be modified. The teflon tube should be eliminated to avoid undesired dimming of the X-ray beam and the fibre should be placed in front of the beam outlet in a way that avoid self-shielding of the fibre itself.

4.3.1.2 Tungsten target

After the successful test with the copper target tube, an X-ray tube with a tungsten target of the company PANalytical was bought by the SciFi group. The choice of the target was related to the energy of the emitted photons. Differently from Cu target tubes, which can be powered at most at 20 kV, tungsten target tubes can be operated up to 60 kV. The emission spectrum and dose rate were evaluated and are discussed in the following.

Emission spectrum and dose rate

The emission spectrum was evaluated with the commercial software *SpekCalc* [69]. The software allows to calculate the emission spectrum of an X-ray tube with tungsten target as a function of the applied high voltage and possible filter layers. The thickness and material of each layer are defined by the user. Fig. 4.16 shows the emission spectra for a tungsten tube powered with a high voltage of 40 kV, after a layer of air of 45 mm thickness and layers of aluminium of different thicknesses. The typical spectrum of an X-ray tube shows spikes corresponding to the characteristic lines of the target atoms and a continuous distribution due to bremstrahlung. A thin layer of aluminium can be used to absorb the low energetic X-rays and eventually remove the peak below 10 keV.

The dose rate at a distance of 45 mm from the beam outlet was measured as a function of different tube settings and layers of aluminium with the Gafchromic HD-810 films described previously. Also in this case a 30% correction is applied to the dose estimated from the curve in Fig. 4.12. From the data sheet of the films the uncertainties on the dose rate measurements were estimated to be 8%. The measured dose rates are plotted in Fig. 4.17. The dose rate increases linearly with the anode current and amounts to 23 Gy/min when the tube is operated at 40 kV, 30 mA. The placement of an aluminium layer of 0.17 mm or 0.34 mm thickness reduces the dose rate to 5 Gy/min and 2.5 Gy/min, respectively.

Discussion

The measured dose rates positively confirm the expectations based on the initial test performed with the Cu target tube. Also the energy spectrum of the emitted X-rays is satisfactory. It was therefore decided to use the tungsten target X-ray tube for the QA tests. The whole setup and the result of the tests will be discussed in the following section.

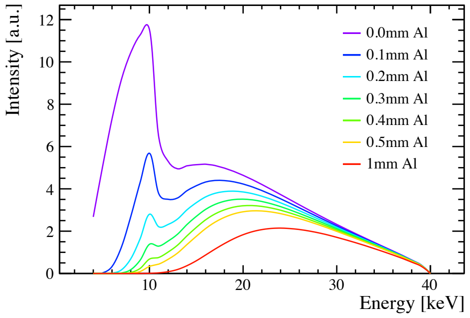

Figure 4.16: Emission spectra of an X-ray tube with tungsten target, powered with a high voltage of 40 kV, at a distance of 45 mm.

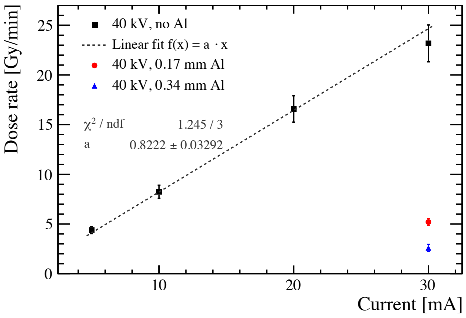

Figure 4.17: Measured dose rate at a distance of 45 mm from the beam outlet wit the tube operated at 40 kV.

4.3.2 X-ray test for fibre QA

This section presents the QA radiation test, which is regularly performed to monitor the radiation resistance of SCSF-78 fibres.

Setup

The setup is described in detail in Ref. [70] and summarised here. The X-rays are generated by an XRD glass tube with a tungsten target produced by the company PANalytical. It can be powered up to a maximum high voltage of 60 kV and a maximum power of 2.4 kW, so that the maximum anode current at 60 kV is 40 mA. The company GNR[8], who provided the power supply and the tube housing, suggested to operate the tube at a maximum setting of 40 kV, 30 mA to ensure a longer lifetime of the tube. The tube is positioned in a shielded housing, provided with two electromagnetic and mechanical safety shutters. When the shutters are closed, the radiation outside the tube shield is less than 1 mSv/year (full safety shielding according to the international guidelines) even when the X-ray tube is operated at its maximum power. The tube shield is installed in a custom-made shielding box shown in the picture in Fig. 4.18. Its side walls, facing the X-ray outlets, are made of 5 mm thick lead plates, sandwiched between aluminium sheets. The top and bottom walls are fabricated from 6 mm thick copper sheets, while the back wall and front double doors are fabricated from 5 mm thick copper sheets. Structural stability is assured by a framework of Bosch profiles.

The high voltage is provided by a power supply of type GNR C3K6PC-RS232, located below the shielding box. The power supply can provide a maximum power of 3 kW and a maximum high voltage of 60 kV. The tube requires to be cooled by chilled water, which circulates in a closed loop with a refrigeration cooler (Julabo FL2503). The temperature of the water must be kept between

---

[8] http://www.gnr.it

20° C and 26° C and the pressure between 4 and 8 bars.
The X-ray setup is equipped with several safety devices. The power supply is interlocked with two door switches on the shielding box, with a flow switch and the X-ray warning lamp. Furthermore the power supply is interlocked in case of overload, overvoltage or overcurrent.

Figure 4.18: Custom-made shielding box containing the X-ray tube. The power supply is placed below the shielding box.

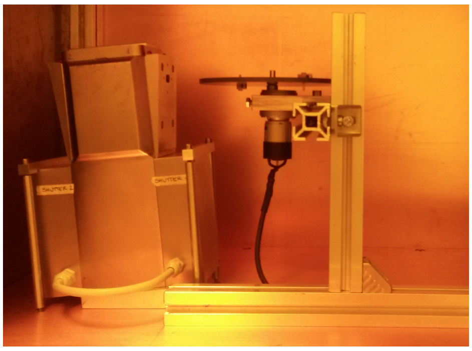

Figure 4.19: Zoom on the setup inside the shielding box. The fibre under test is coiled around a plastic rotating wheel facing the X-ray outlet.

The scintillating fibre under test is typically 3 - 3.5 m long. In this way its attenuation length can be measured as described in Section 4.1. The fibre is wound on a 15 cm diameter and 5 mm high plastic wheel, equipped with a spiraling groove (Figs. 4.20 and 4.21). The wheel can be placed in the setup so that the coiled fibre faces the beam outlet. The wheel is connected to a motor and rotates with constant speed, to ensure uniform irradiation over the whole fibre length. The setup inside the shielding box is shown in Fig. 4.19.
Dosimetry is carried out with the previously described Gafchromic HD-810 dosimetric films (Section 4.3.1.1). The maximum energy of the X-rays generated in this setup is 40 keV and the mean energy 16 keV (no aluminium filter is used for the QA tests). Therefore the already mentioned 30% correction is applied to the dose estimated from the curve in Fig. 4.12. Since the used X-ray beam is not monochromatic, the presence of a systematic error on the dose evaluation can not be excluded. Nevertheless, in order to compare different fibres for quality assurance purposes, it is sufficient to measure the effects of the irradiation under defined and stable experimental conditions.
A dosimetric film is fixed to the rotating wheel before every irradiation as shown in Fig. 4.22 and then measured with a Model 37-443 Nuclear Associates densitometer. From the data sheet of the films the uncertainties on the dose rate measurements are estimated to be 8%. A picture of a Gafchromic HD-810 film after irradiation is shown in Fig. 4.23.

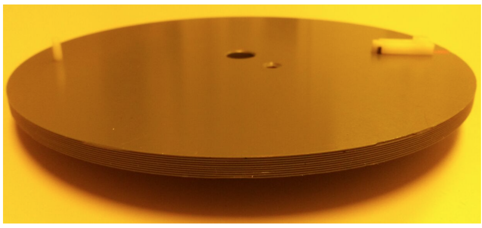

Figure 4.20: The plastic wheel.

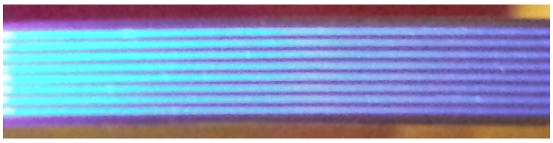

Figure 4.21: The fiber under test coiled around the plastic wheel. In this picture the fibre is excited with UV-light in order to improve visibility.

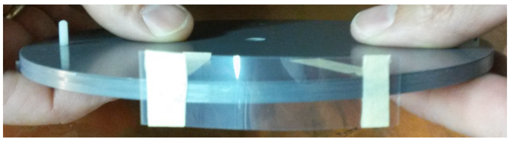

Figure 4.22: A picture of a transparent Gafchromic HD-810 dosimetric film fixed on the plastic wheel before irradiation.

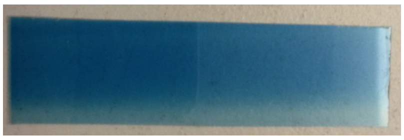

Figure 4.23: A Gafchromic HD-810 dosimetric film after irradiation: the active component reacted to form a blue polymer. The central region, where the fibres are located, has received a uniform dose.

Results

X-ray irradiation tests are carried out with the tube operated at 40 kV and 30 mA. With these settings the fibre under test, placed at a distance of 4.5 cm from the beam outlet, receives a dose rate of about 23 Gy/min.

The plots in Fig. 4.24 show the results of some of the tested fibres. As discussed in Section 4.1, the attenuation length is measured with an uncertainty of 5%. To evaluate the deterioration induced by irradiation, the attenuation length has to be measured twice, before and after the irradiation. The error assigned to each data point in Fig. 4.24 is the result of the uncertainty propagation. All the irradiated samples keep an attenuation length between 65% and 78% of the original value. The average values over all the tested fibres amount to $\Lambda'/\Lambda_0 = 0.72$ and $\alpha_{\mathrm{rad}} = 1.1 \cdot 10^{-3}\,\mathrm{cm}^{-1}$.

Both the intrinsic attenuation, α_0, and the induced absorption, α_{rad}, are wavelength dependent. The spectral attenuation lengths of all the SCSF-78 samples tested with the X-ray setup for quality assurance purposes were measured as described in Section 4.1.1 both before and after irradiation. An example is shown in Fig. 4.25, where both $\alpha_0(\lambda)$ and $\alpha_{\mathrm{rad}}(\lambda)$ are plotted. The wavelength distribution of the induced absorption after 1 kGy shows a minimum at about 500 nm and a wide absorption band in the range 600 - 700 nm. Several tests were performed to study the dependency of α_{rad} on the dose, dose rate, radiation source and gas environment. They are illustrated and discussed in detail in the following chapters.

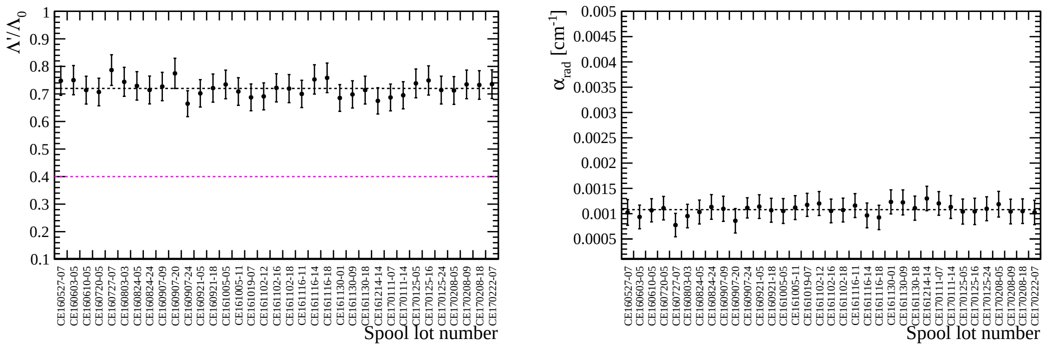

(a) (b)

Figure 4.24: Results of the X-ray radiation test up to 1 kGy with a dose rate of 23 Gy/min. $\Lambda_0 = \alpha_0^{-1}$ is the attenuation length before and $\Lambda' = \alpha'^{-1}$ is the attenuation length after irradiation, while $\alpha_{\text{rad}} = \alpha' - \alpha_0$ is the induced absorption. For clarity purposes only 30 samples are shown in this plot. The chosen subset is representative for all the tested samples. A discussion about the assigned errors can be found in the text. The magenta dashed line corresponds to the required limit of $\Lambda'/\Lambda_0 = 0.4$. The black dashed lines corresponds to the average values over all the tested samples.

Discussion

The requirement on the radiation hardness is that, after being exposed to X-rays to an ionizing dose of up to 1 kGy, the attenuation length of a 3 m long fibre shall not decrease to less than 40% of its original value. The choice of this limit is derived from the hadron irradiation tests presented in Section 3.4.1. The results of the measurements are stable and all the tested fibre samples are well above the required limit of 40%.

As outlined in Section 2.3, the damage of ionizing radiation to plastic material is known to depend on radiation type, energy, rate and environmental parameters. X-ray irradiation can therefore not be used to validate the hardness of fibres in a high energy hadron radiation field. Nevertheless the X-ray setup described in this section offers the major advantages of being accessible at any time and allowing high throughput. In particular, a 3.5 m long fibre sample can be irradiated up to 1 kGy within 45 minutes. The X-ray test aims at the detection of possible anomalies in the degradation of the attenuation length, when exposed to X-ray irradiation, which may hint to chemical or other problems (e.g. polluted ingredients). X-ray irradiation tests are therefore considered a useful complement to the optical QA tests.

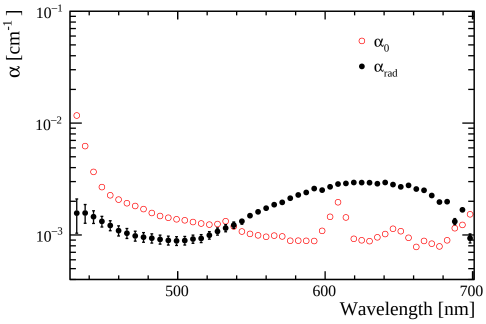

Figure 4.25: Spectral resolved absorption coefficient. The red empty dots represent $\alpha_0(\lambda)$, i.e. the intrinsic absorption of the fibre. The black full dots correspond to $\alpha_{\text{rad}}(\lambda)$, i.e. to the induced absorption due to X-ray irradiation up to 1 kGy.

4.4 Diameter measurement and bump shrinking procedure

The geometrical specifications of the fibres are crucially important for the SciFi project. In order to have an even pattern when they are staggered in the six-layer configuration, the fibres should have a circular cross-section and a regular diameter. Local variations in the diameter are defined as “bumps” or “necks” if the diameter exceeds the nominal value of 250 µm by ±25 µm. Such fluctuations usually have a length scale of a few centimetres, or even millimetres. They are created during the fibre production and can be attributed to non-uniformities in the core and cladding material or to the presence of extraneous material in the fibre, like a splinter of glass or a dust particle. The diameter is measured with a fibre scanner machine [71]. During this measurement, the whole length of a fibre is unwound from the original spool it was delivered on (so called “source” spool) and wound on another “target” spool. Between the two spools there are several elements shown in Fig. 4.26 and described in detail in Ref. [71]. In particular, the AccuScan Laser Micrometer performs a precise measurement of the diameter along two orthogonal axes with a rate of 2400 Hz and an accuracy of better than 0.1 µm.
The fibre scanner typically runs at full speed (1 m/s). If a bump or a neck are detected by the lump&neck detector the speed is reduced to 15% of the full speed.

The presence of a bump creates local deformations in the six-layer pattern (Fig. 4.27). If the diameter is bigger than 350 µm, the distortion is such to have an impact on the spatial resolution of the detector, therefore those bumps must be removed. The bump shrinking procedure [72, 73] provides a method to reduce the diameter up to the acceptable limit of 350 µm. The method consists in drawing the fibre through a drawing tool with a conical profile and a minimum diameter of 350 µm (Fig. 4.28). The tool is mounted in a cylindrical heating element which keeps it at the constant temperature of 100°C (Fig. 4.29). The drawing tool is

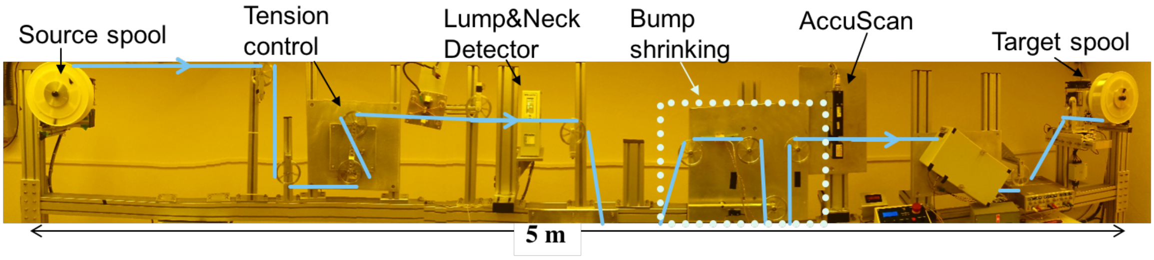

Figure 4.26: A panoramic picture of the fibre scanner machine.

integrated in the fibre scanner machine as illustrated in Fig. 4.26 and 4.30. When a bump exceeding 350 µm reaches the drawing tool, it is not able to pass through the hole and it gets temporarily stuck into the tool. The tension created by the motor connected to the target spool makes the pivoting arm lift up. The arm is connected to a switch, which is open if the arm is lifted by more than about 10 mm. Opening the switch stops the target motor. The mass of the lifted arm creates a tension on the fibre of 100 cN directed downwards. The bump in the tool is locally heated and the plastic materials of which the fibre is composed soften thanks to their thermoplastic nature. As soon as the fibre has softened sufficiently to creep through the tool, the arm lowers and the motor restarts. The whole shrinking process takes typically about 1 s.

The bump shrinking procedure has a very high success rate, close to 100% for bumps smaller than 500 µm. However it can fail if the bump is very big, or if the excess of diameter extends along a particularly long segment (several centimetres), or if the bump is due to the presence of a solid particle like for example a splinter of glass. In these cases the fibre eventually breaks under the tension created by the lifted arm. The scanning process needs then to be interrupted and the “cut&glue” procedure is implemented. It consists in manually cutting away the bump and gluing the two fibre ends together. Before gluing, the two fibre ends are treated with a guillotine-like fibre cutter which produces orthogonal cuts of reproducible quality. They are then carefully aligned with the help of a 2-stage x-y table and a USB microscope (Fig. 4.31). A small amount of UV curing glue[9] is applied to both fibre ends, which are then gradually brought in contact. The amount of glue and its distribution as well as the alignment of the fibre ends are controlled with the microscope and can still be corrected (within 1 - 2 minutes). The curing of the glue is obtained by exposing it to a 300 mW UV light source[10], emitting at 365 nm. The typical exposure time is 12 - 15 s at a distance of about 1 cm. A typical gluing sequence is shown in Fig. 4.32. The cut&glue station is positioned before the bump shrinking setup, so that the glued extremities still need to pass through the drawing tool. This choice allows to avoid the accidental introduction of a new bump due to excess of glue. The scanning of the fibre can be restarted immediately after curing. The whole cut&glue procedure usually takes about

---

[9] Loctite 4305 LC

[10] APM UV Cure (LED 365 nm), APM Technica, CH-9435 Heerbrugg, Switzerland

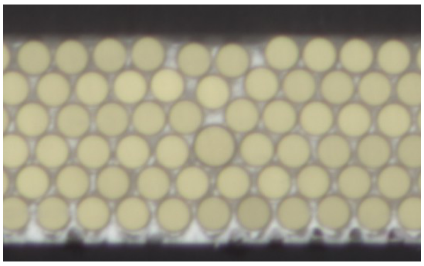

Figure 4.27: Local deviation from the regular six-layer pattern due to the presence of a bump.

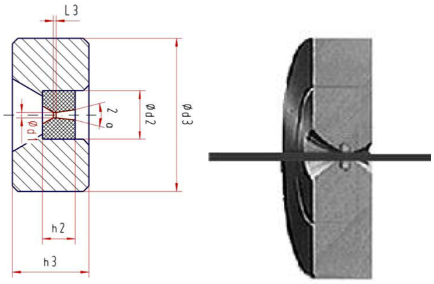

Figure 4.28: Geometry of the drawing tool. The smallest diameter is $d_1 = 350\,\mu m$.

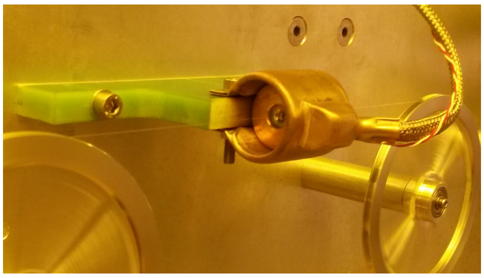

Figure 4.29: A picture of the drawing tool in the fibre scanner.

10 - 15 minutes. In average only 1.0 cut&glue intervention per spool is required.

4.4.1 Validation of the bump shrinking procedure

Light losses across shrunk bumps and glue joints

The presence of a bump or a shrunk bump implies that the geometry of the fibre is locally modified. Therefore photons, which should be totally reflected inside the fibre, might escape. The amount of photons lost due to geometrical irregularities depends on the bump size and type. The light leaks across shrunk bumps were assessed by performing an attenuation length measurement with the setup decribed in Section 4.1. For this purpose three fibre samples of 3 m length were selected which contained a shrunk bump each with an original (before shrinking) diameter above 350 µm. The plot in Fig. 4.33(a) shows the measured photocurrent as a function of the excitation distance for one of the three samples. The exponential fit was performed as usual between 100 cm and 300 cm. In each plot the points between 100 cm and the shrunk bump were fitted with one exponential and the points between the shrunk bump and 300 cm were fitted with another exponential:

$$f(x) = \begin{cases} \mathrm{I}_1 \cdot e^{-x/\Lambda}, & 100 < x < \text{bump} \\ \mathrm{I}_2 \cdot e^{-x/\Lambda}, & \text{bump} < x < 300. \end{cases} \tag{4.2}$$

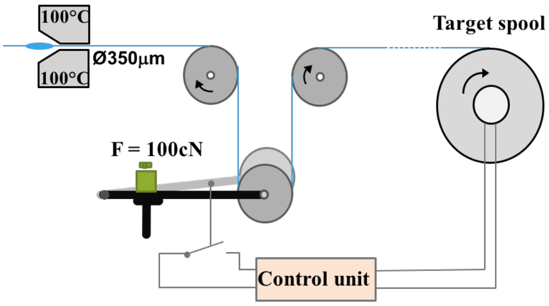

Figure 4.30: Sketch of the bump shrinking setup. The drawing direction is from left to right.

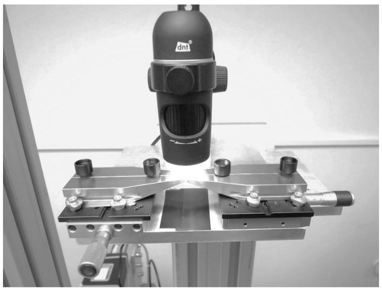

Figure 4.31: Gluing station consisting of two translation tables (in x-y configuration) and a USB microscope. The fibres are held by soft magnets in the V-grooves of the two mounting plates.

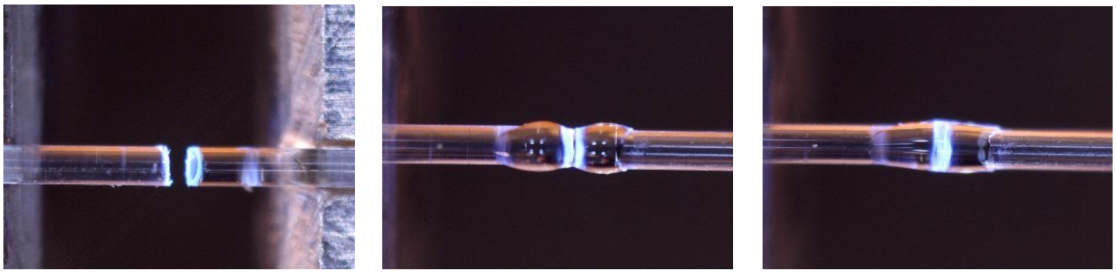

Figure 4.32: Alignment and glue distribution at the glue joint. The slight glue excess leads to a formation of a sleeve-like reinforcement, which improves the stability. In order not to act as bump, its total diameter must stay below 350 µm. These pictures are taken with the USB microscope in the gluing station.

The requirement on the two exponentials was that they have the same slope, since the intrinsic absorption of the fibre is not affected by the presence of the bump. The light leak Δ at the position of the bump was derived from the percent difference of the photocurrent values extrapolated from the two fitted curves before and behind the bump. The resulting light losses were consistently found smaller than 20%, which corresponds to a light transmission bigger than 80%. The ligh absorption of a glue joint was also assessed with the same procedure. The result is shown in Fig. 4.33(b). In this case the trasmitted light amount to 18%.

Radiation hardness of bumps and shrunk bumps

The radiation hardness of a bump and of a shrunk bump were tested with the X-ray setup used for the QA tests. Two fibre samples were prepared: both of them were 3.3 m long, one sample containing a bump, the other sample containing a shrunk bump. Both samples were irradiated up to a dose of 1 kGy with a dose rate of 23 Gy/min. The settings for the X-ray tube are chosen to be the same as for the QA test, so that a comparison with bump free samples is possible. The

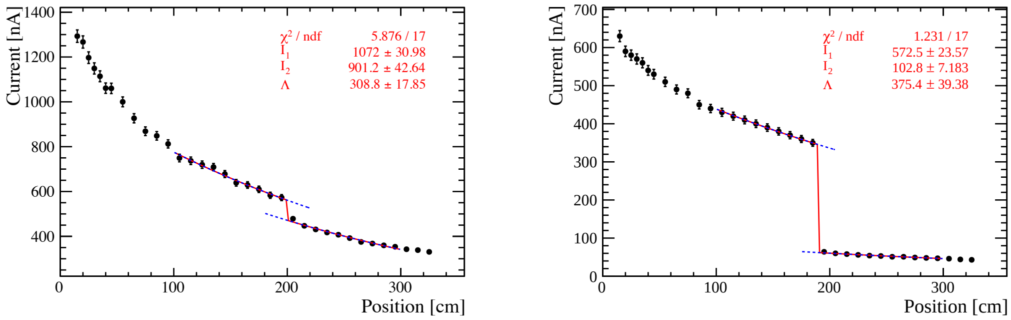

(a) Shrunk bump (b) Glue joint

Figure 4.33: Result of the attenuation length measurement for a sample containing a shrunk bump (a) and a sample containing a glue joint (b). The light leak results in a drop in the current measured by the PIN-diode, clearly visible at position 200 cm (a) and 190 cm (b) .

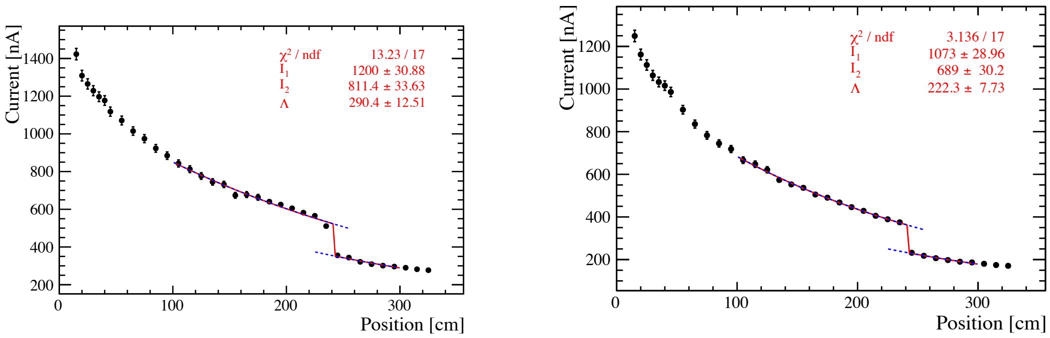

(a) Before irradiation (b) After 1 kGy

Figure 4.34: Attenuation length of a sample containing a bump before and after X-ray irradiation.

attenuation length of both samples was measured before and after the irradiation. The light loss Δ due to the presence of the (shrunk) bump is evaluated from the attenuation length measurement as explained above. The results are shown in Figs. 4.34 and 4.35 and listed in Table 4.1. The reduction of the attenuation length due to irradiation is about 25 - 30%, as expected from previous irradiations of samples without bumps and the light loss due to the (shrunk) bump does not increase significantly after irradiation. It can be concluded that bumps and shrunk bumps do not affect the radiation resistance of the fibre.

Mechanical stability

Several samples containing either a shrunk bump or glue joint were used to test the mechanical stability of the fibre after the bump shrinking or the cut&glue

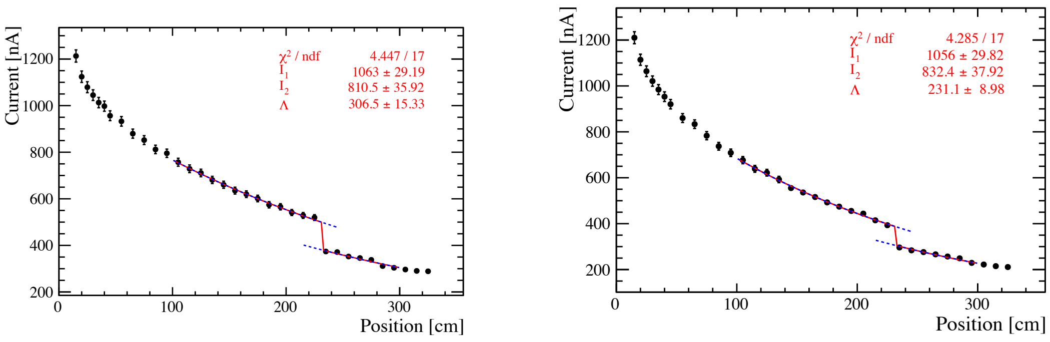

(a) Before irradiation

(b) After 1 kGy

Figure 4.35: Attenuation length of a sample containing a shrunk bump before and after X-ray irradiation.

	Bump		**Shrunk Bump**	
	Before	After	Before	After
Attenuation length [cm]	290 ± 15	222 ± 11	307 ± 15	231 ± 12
Light leak Δ	32%	35%	24%	21%

Table 4.1: Values of the attenuation length and light leak for a sample containing a bump and a sample containing a shrunk bump before and after X-ray irradiation up to 1 kGy.

procedure. The tests were performed using a mechanical fine-scale force gauge with 10 cN resolution. The fibre under test was fixed on a spool at one extremity and on the force gauge on the other extremity. A force was applied on the force gauge until the fibre broke. The minimum force needed to break a bump is expected to be higher than for a normal sample because a fibre with a bigger diameter is more resistant against pulling. In addition, as pointed out by the fibre producer, the combined application of heat and tension might further increase the stability, by inducing the polystyrene chains to align themselves to the fibre axis and de facto locally changing the structure of the bumpy section into an S-type fibre[11] [74]. Indeed, while the breakage force for fibres with nominal diameter of 250 µm is about 220 cN, samples containing a bump never broke before applying at least 300 cN. The series of pull tests carried on with samples containing a glue joint revealed an average force at break of about 130 cN. This represents a reasonable safety margin considering the standard pull force during scanning and fibre mat winding of 50 cN.

---

[11] The S-parameter ($0 \leq S \leq 1$) describes the degree of alignment of the polystyrene chains along the fibre axis. A high S-parameter ($S > 0.7$) leads to better mechanical stability at the cost of lower transparency. The 250 µm fibres from Kuraray have an S-parameter of about 0.4.

Effect of the bump shrinking setup on the fibre

The integration of the bump shrinking setup in the fibre scanner machine implies that the fibre passes through the hot drawing tool over its full length. Sections of the fibre with a diameter smaller than 350 μm should not get in touch with the hot walls. However, even with a perfect alignment of the tool with the fibre axis, the nominal distance between the cladding and the walls is 50 μm. Several studies in the literature report temperature dependent degradation of the optical properties of plastic fibres. Therefore it was necessary to demonstrate that the non-bumpy sections of the fibre are not damaged when passing through the drawing tool. Several measurements were performed to test the attenuation length, light yield, diameter, mechanical stability and integrity of the cladding after the fibre run through the hot tool with the nominal speed of 1 m/s, with a very low speed of 3 cm/s and with the speed of 15 cm/s. The latter is the velocity to which the fibre is slowed down whenever the lump&neck detector reveals a bump. Also the regions of about 1 m before and after the bump pass through the tool with this speed. The length of the contact zone (L3 in Fig. 4.28) is of the order of 1 mm, therefore the contact time at 15 cm/s is below 10 ms. No degradation of any of the tested properties were seen. The details of the performed tests can be found in Ref. [73].

4.5 Decay time

This section describes the setup to verify a further characteristic of SCSF-78 fibres, i.e. their decay time. The requirement for the SciFi detector on this value is not as stringent as for other properties, therefore this test is not regularly performed. The goal is to confirm the correctness of the nominal value given by the producer[12]. Deviations could give hints on changes in the chemical composition or impure ingredients.

In order to measure the decay time a fibre is laterally excited by a fast pulsed LED at 15 cm distance from the readout, performed with a fast PMT (Hamamatsu H7826). The light intensity is adjusted such that the PMT detects primarily single photons. The LED (PicoQuant PLS370, $\lambda = 375\,\mathrm{nm}$, $\sigma \sim 220\,\mathrm{ps}$ pulse width) is powered by a PDL-800 (Pulsed Diode Laser Driver) and triggered by a fast pulse generator, which also provides the start signal. The stop signal is given by the amplified and discriminated PMT signal. The events are recorded with a LeCroy LT344 digital oscilloscope. The resulting time distribution is shown in Fig. 4.36. The fitting function is

$$f(x, \mu, \sigma, \tau) = \frac{1}{2\tau} \exp\left[\frac{1}{2\tau}(2\mu + \frac{\sigma^2}{\tau} - 2x)\right] \operatorname{erfc}\left(\frac{\mu + \frac{\sigma^2}{\tau} - x}{\sqrt{2}\sigma}\right) \tag{4.3}$$

where erfc is the complementary error function. It is the convolution of an exponential, containing the decay time constant τ of the scintillation light, with a

---

[12] Kuraray catalogue: http://kuraraypsf.jp/psf/index.html

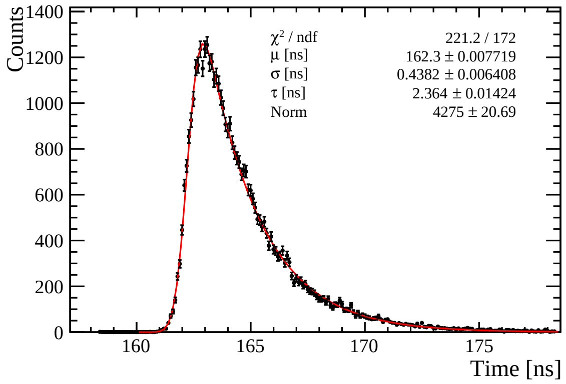

Figure 4.36: Decay time of a SCSF-78 fibre.

Gaussian, whose width σ accounts for the overall time jitter of the experimental setup. In our setup the width of the Gaussian amounts to $\sigma \sim 450\,\text{ps}$. The measured decay time constant of SCSF-78 fibres amounts to 2.4 ns.
Since the fibre is excited with a UV-LED, the measured value correspond to the decay time of the sole wavelength shifter. However, as discussed in Chapter 2, this is assumed to be the dominating contribution to the overall decay time of the scintillating fibre.
The decay time of SCSF-78 reported on the Kuraray catalogue amounts to 2.8 ns. It should be noted that this value is not based on a direct measurement of a fibre, but is derived from the decay time of the wavelength shifter dye of this fibre in solution.

4.6 Samples storage and measurements repetitions

All the fibre samples taken for the QA tests are stored in a dark room with a constant temperature of about 22° C. A picture of the stored samples is shown in Fig. 4.37. Those samples can be measured again at any time to make sure that the performances of the fibres do not degrade with time.
It should also be mentioned that the fibres are covered by full warranty for a period of two years. The requirement is that the optical performances of the samples, stored in a controlled environment and protected against any adverse condition such as exposure to UV light, radiation, heat or mechanical mishandling, shall not drop by more than 10% during this period.
An example is shown in Fig. 4.38. The attenuation lengths of some spools were measured again after about 7 months and compared to the measurements performed just after delivery. For all the spools the measured values are compatible within 1σ and no time dependent degradation is seen. More spools will be tested in the future.

Figure 4.37: Stored QA samples in the dark room.

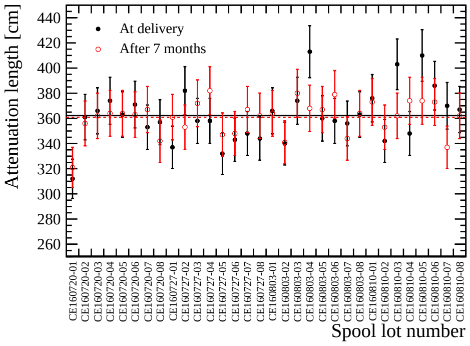

Figure 4.38: Attenuation length per spool measured at the delivery (black full markers) and after 7 months (red empty markers). The black line corresponds to the average attenuation length of these selected spools at delivery (362 cm), while the red dashed line represents the average attenuation length after 7 months (361 cm).

4.7 Summary of QA tests

The setups used to assure the quality of 11′000 km of scintillating fibres for the LHCb detector were presented in this chapter. They were almost continuously in use from May 2016[13]. A total of 6′700 km of fibres were analysed until the time this thesis was written. Another 4′300 km of fibres will be delivered until the end of 2017.

The regularly monitored performances are the attenuation length, the light yield, the resistance to X-ray radiation and the diameter profile. The optical performances and the degradation after X-ray exposure are stable and above the requirements requested for the SciFi detector. In particular the average attenuation length amounts to 351 cm, the average light yield to 13.8 photoelectrons and the average reduction of the attenuation length after a dose of 1 kGy to $\Lambda'/\Lambda_0 = 0.72$. The fibre is scanned by the scanner machine with a typical speed of 1 m/s. Irregularities in the fibre diameter are thermally treated, so that the diameter is shrunk to the maximum accepted limit of 350 µm. This procedure is fully automatic and does not delay the scanning of the fibres. Only once every 12.5 km the bump shrinking procedure fails. In this case a manual intervention is necessary and a delay of about 10 - 15 minutes is introduced.

All the setups run smoothly and required only minor maintenance interventions. No showstoppers are expected and the fibre quality assurance is foreseen to be completed by the beginning of 2018.

---

[13] the fibre scanner machine typically runs 10 hours per day, 5 days per week (holidays excluded), whilst the other setups are more sporadically used.

Chapter 5

Irradiation studies with X-ray tubes

The aim of the measurements presented in this chapter is to gather knowledge on the response of SCSF-78 fibres after X-ray irradiation. Several tests were performed exposing SCSF-78 fibres to X-ray radiation. The measurements were done with two different setups. In the first case a commercial X-ray setup was used, made available from the Heidelberg SciFi group. The second setup used is the one built for the QA tests.
The spectral damage was evaluated and compared to the one induced by hadrons irradiations. The behaviour of SCSF-78 fibres was studied when irradiated or stored under various conditions, i.e. different dose, dose rate and gas atmosphere. Finally the degradation of the scintillation light yield was investigated at different doses.

5.1 Irradiations with the setup in Heidelberg

The goal of this irradiation campaign was to define the lowest dose that causes a visible damage in the fibres. For this reason a fibre sample was irradiated from a dose of 10 Gy up to 60 Gy in steps of 10 or 20 Gy.

Setup

The setup was conceived and arranged by the SciFi group in Heidelberg.
One 251 cm long fibre sample was coiled around a 3D printed cylinder in a narrow groove and bonded with glue as shown in Fig. 5.1. The cylinder was 15 cm high and had a diameter of 20 cm.
The fibre was irradiated with X-rays from a tungsten tube in a commercial device[1] operated at 35 kV with an anode current of 1 mA. The cylinder was placed as shown in Fig. 5.2(a) with its lateral wall facing the X-ray outlet at a fixed distance

---

[1] Phywe, XR 4.0 X-ray system, https://www.phywe.com/

Figure 5.1: A 251 cm long fibre coiled in narrow groove and bonded with glue around a 3D printed cylinder. The fibre is highlighted in black.

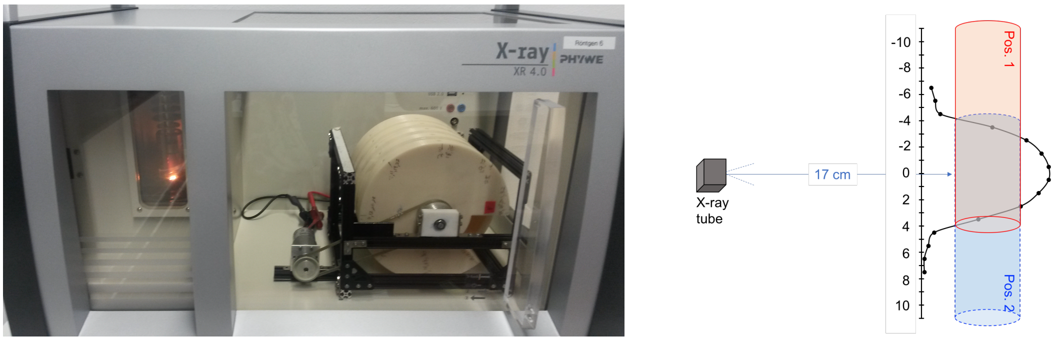

(a) (b)

Figure 5.2: Setup for the X-ray irradiation. (a) The cylinder is located at a distance of 17 cm from the X-ray tube and rotated at a couple turns per minute. (b) To ensure a uniform dose rate along the whole fibre length first the right side of the cylinder is irradiated (position 1) and then the left side (position 2). The dose rate profile is also drawn for illustrative purposes.

of 17 cm from the tube. During the whole irradiation the cylinder was rotated at a couple of turns per minute. The dose rate profile along the cylinder's axis was measured by the Heidelberg SciFi group with a calibrated plastic foil (Fig. 5.3, [75]). It has a semi-gaussian shape with a FWHM of about 7 cm. In order to get a uniform dose rate of 3.65 Gy/h along the whole fibre, first the right side and then the left side of the cylinder were irradiated with the cylinder centred 7 cm apart, as illustrated in the schematic in Fig. 5.2(b).

The attenuation length was measured before and after each irradiation. A UV-LED was mounted in a box provided with two legs, which could be fixed in holes along the lateral wall of the cylinder. The LED could thus be placed at regular and reproducible distances from the fibre and from the photodetector. A Newport UV-818 calibrated photodiode was placed at either end of the coil to measure the light output. The current output was measured with a Keithley picoammeter.

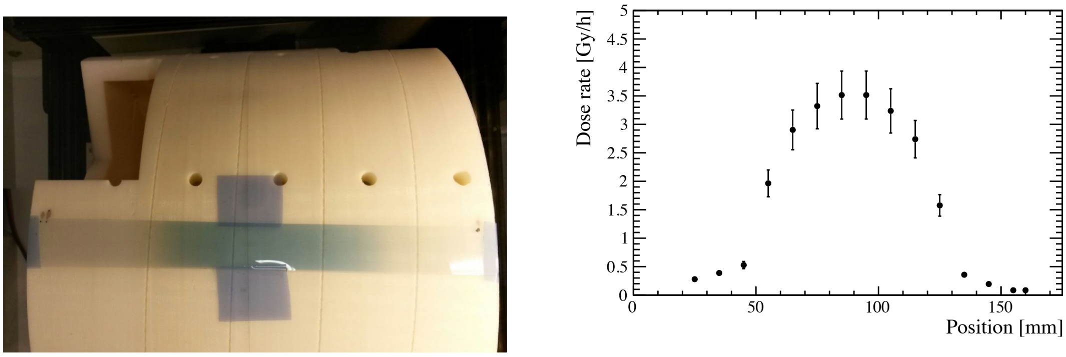

(a) (b)

Figure 5.3: (a) Dosimetric foil fixed with tape on the cylinder. (b) Dose rate profile along the cylinder's axis [75].

Analysis and results

The choice of the setup, with the fibre glued on the cylinder, requires a different procedure to extract the attenuation length than the one described in Section 4.1. The non-uniformity of the glue thickness along the fibre introduces local attenuation factors of the UV photons emitted from the LED. As a result, the curve of the photocurrent as a function of the distance between the photodetector and the excitation point deviates from the exponential function $I(x) = I_0 e^{-x/\Lambda}$. The attenuation length can still be obtained by measuring the photocurrent twice, with the photodiode placed at either extremity of the fibre ("forward" and "backward" measurement). The local effects c_i cancel out when taking the ratio between forward and backward measurement:

$$R(x) = \frac{\mathrm{I_F} \cdot c_i \cdot e^{-x/\Lambda}}{\mathrm{I_B} \cdot c_i \cdot e^{-(\ell - x)/\Lambda}} = \mathrm{I}_R \cdot e^{-(2x-\ell)/\Lambda} \tag{5.1}$$

where $\ell = 251$ cm is the length of the fibres. Pictures of the forward and backward measurements are shown in Fig. 5.4. The plots in Fig. 5.5 show one example of a forward and backward measurement and the fit to the ratio. Since the fibre is only 251 cm long the fits are performed between 70 cm and 251 cm. In the time at disposal, the attenuation length before the irradiation and after a dose of 10 Gy, 20 Gy, 40 Gy and 60 Gy were measured. No degradation of the fibre's performances were seen. Further irradiations with this setup were not performed due to time limitations.

5.2 Irradiations with the QA setup

The measurements presented in this section were performed with the X-ray setup used for the quality assurance tests described in Section 4.3.2.

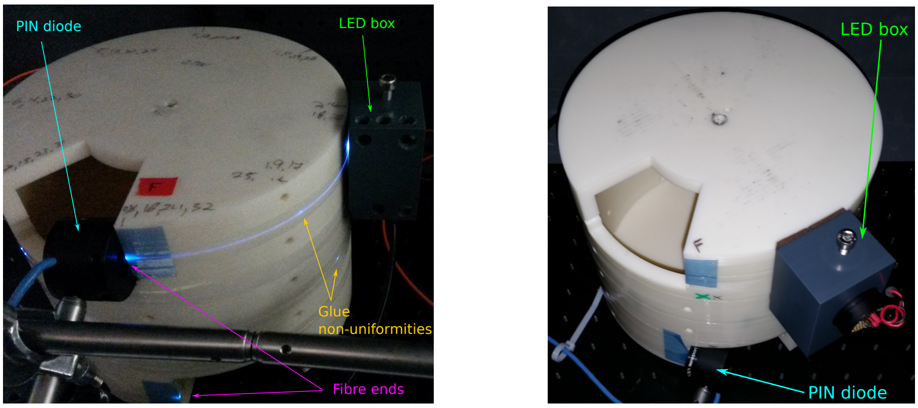

(a) Forward (b) Backward

Figure 5.4: Picture of the setup to measure the attenuation length in the forward (a) and in the backward (b) direction. The fibre is laterally excited with a UV-LED and the light output is measured with a photodiode at either end of the fibre. The two bright blue spots along the fibre (left picture) correspond to regions where the glue was thinner.

5.2.1 Dose dependent degradation

The dependency of the induced damage on the total absorbed dose was studied in the dose range 220 Gy - 10 kGy. All the tested samples were irradiated with the tube powered at 40 kV, 30 mA and a dose rate of 23 Gy/min. The maximum energy of the X-rays is 40 keV and the mean energy 16 keV. The attenuation length measurements before and after irradiation were performed using both the PIN-diode and the spectrometer.

The plot of the integral $\alpha_{\rm rad}$ as a function of the dose is shown in Fig. 5.6(a). The measured data are fitted with different curves, linear and power functions. It should be noted that, since $\alpha_{\rm rad}$ is defined as the additional absorption induced by the irradiation, its value should be equal to zero for any unirradiated fibre. Therefore any meaningful curve of $\alpha_{\rm rad}$ as a function of the dose should fulfil the requirement $\alpha_{\rm rad}(D = 0) = 0$, where D indicates the dose. The linear fit in Fig. 5.6(a) fails to have a physical meaning, because it is not possible to fit the data with a straight line passing through the origin. The best fit seems to be a power function ($\alpha_{\rm rad}(D) = 9 \cdot 10^{-4} \cdot \mathrm{D}^{0.47}$). The slope of this function is then essentially proportional to $1/\sqrt{D}$, i.e. it is initially large and it ultimately tends to zero. This behaviour implies that some annealing processes are taking place already during irradiation.

From Fig. 5.6(b) it is however clear that different wavelengths are differently affected by the irradiation. In particular, $\alpha_{\rm rad}$ is dose independent for wavelengths higher than ~ 550 nm. For higher energy photons the dose dependency is very strong and it increases with decreasing wavelength. The induced absorptions after different total absorbed doses differ by about one order of magnitude for photons with wavelengths smaller than 500 nm.

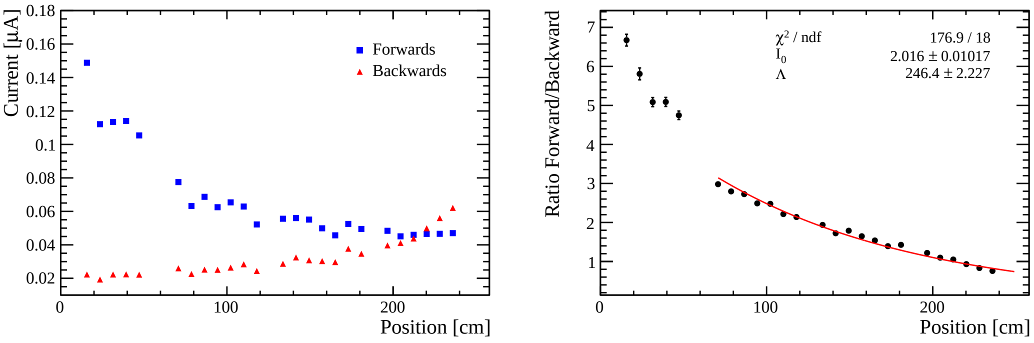

(a) (b)

Figure 5.5: (a) The measured photocurrent as a function of the distance from the PIN diode for the "forward" and "backward" direction. (b) The ratio between the "forward" and "backward" measurement. Because of the layout of the setup, the current could not be measured for some positions (around 50 cm and 190 cm).

The dose dependency of the induced absorption for photons with $\lambda = 450\,\text{nm}$ is shown in Fig. 5.7(a). Those are the most important photons for the SciFi project, since the emission spectrum of SCSF-78 fibres for photons generated at a distance of 2.5 m from the photodetector peaks at 450 nm. The data are fitted with the same curves as in Fig. 5.6(a), with the difference that the linear fit can now be forced to intercept the origin. The fitting curves are plotted in Fig. 5.7(b), where the x-axis extends till the maximum dose in the SciFi detector, $D_{\max} = 35\,\text{kGy}$. In the plot also the curve $f(\mathrm{x}) = 0.04 \cdot \mathrm{x}^{0.8}$ is shown, which is the prediction of $\alpha_{\text{rad}}(\lambda = 450\,\text{nm}, D)$ for SCSF-78 fibres extrapolated from the irradiation campaigns described in Section 3.4.1. It is clear that the degradation induced by 40 keV X-rays is smaller than the one caused by hadrons.

A comparison between the effect of irradiation with X-rays and hadrons is shown in Fig. 5.8. The dose dependency of α_{rad} normalised by the dose after X-ray irradiation is presented in Fig. 5.8(a). Fig. 5.8(b) shows α_{rad}/D for SCSF-78 fibres after irradiation at KIT with 22.9 MeV protons, at the PS with 24 GeV protons and after AAA irradiation with 0.6 MeV positrons (see Table 3.3). To guide the eye, also two of the curves obtained from the X-ray irradiation (at 0.22 kGy and 8 kGy) are reported in Fig. 5.8(b). It should be noted that the curves displayed in Fig. 5.8 correspond to the initial damage, i.e. just after the irradiation, for the X-ray tests and to the permanent damage, i.e. after the maximum recovery, for the protons and positrons irradiations.
From the comparison of these curves, the following conclusions can be drawn:

- for both X-rays and high energy irradiations, α_{rad}/D seems to be dose independent for doses higher than 8 kGy (at least for wavelength smaller than about 520 nm). On the other hand at lower doses ($D < 8\,\text{kGy}$), α_{rad}/D increases with decreasing dose.

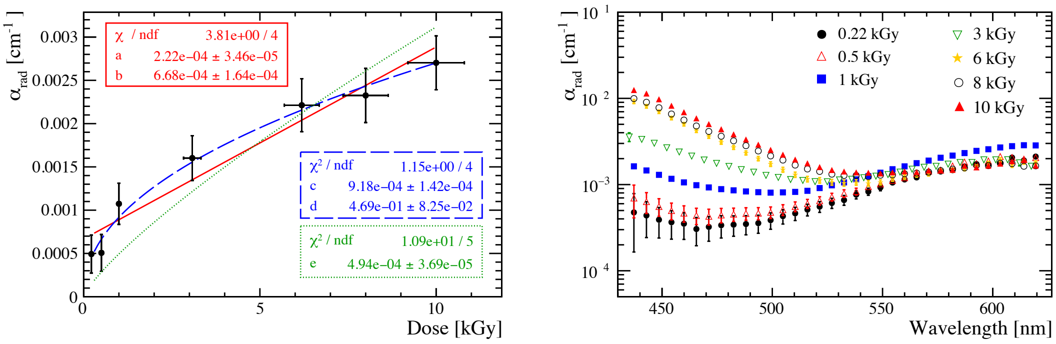

(a) (b)

Figure 5.6: Dose dependency of the induced absorption. (a) The values of α_{rad} extracted from the PIN-diode measurements are plotted against the dose and fitted with a linear curve ($f(\mathrm{x}) = a \cdot \mathrm{x} + b$), with a power function with free parameters ($f(\mathrm{x}) = c \cdot \mathrm{x}^d$) and with a power function with the exponent fixed to 0.8 ($f(\mathrm{x}) = e \cdot \mathrm{x}^{0.8}$). (b) Induced damage as a function of the wavelength. The different curves correspond to different doses absorbed by the fibre sample.

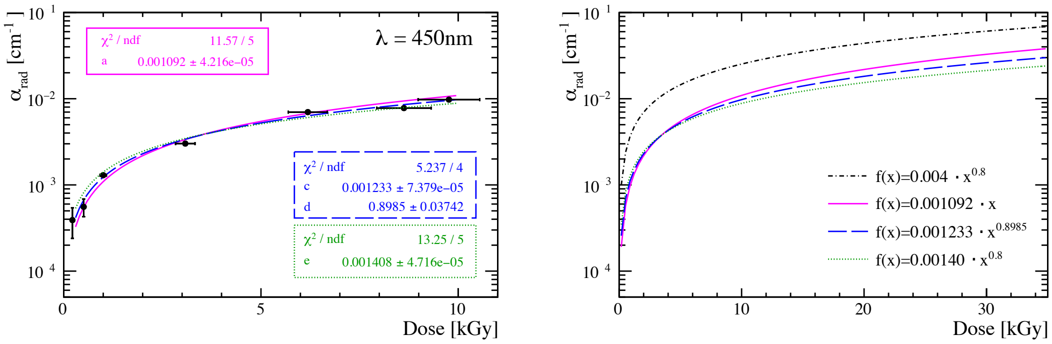

(a) (b)

Figure 5.7: Dose dependency of the induced absorption. The values of $\alpha_{\text{rad}}(\lambda = 450\,\text{nm})$ are plotted against the dose and fitted with a linear curve ($f(\mathrm{x}) = a \cdot \mathrm{x}$), with a power function with free parameters ($f(\mathrm{x}) = c \cdot \mathrm{x}^d$) and with a power function with the exponent fixed to 0.8 ($f(\mathrm{x}) = e \cdot \mathrm{x}^{0.8}$). (b) Extrapolation of the fitting curves for $\alpha_{\text{rad}}(\lambda = 450\,\text{nm}, \text{X-rays})$ up to 35 kGy. The predicted evolution of the induced absorption at 450 nm for the SciFi project ($\alpha_{\text{rad}}(\lambda = 450\,\text{nm}) = 0.004 \cdot \mathrm{D}^{0.8}$) is also shown.

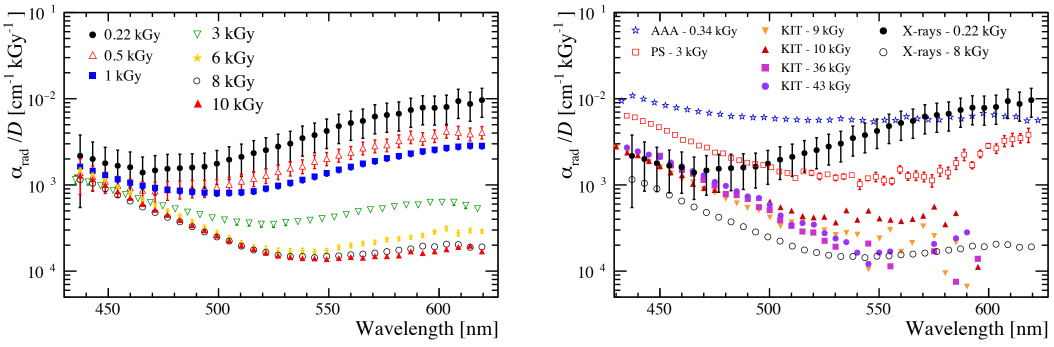

(a) (b)

Figure 5.8: Dose dependency normalised by the dose for (a) 40 keV X-rays irradiations and (b) 0.6 MeV positrons (AAA), 24 GeV protons (PS) and 23 MeV protons (KIT) irradiations.

- As already asserted, the damage caused by X-rays is smaller than the one induced by high energy protons. This statement can be verified in Fig. 5.8 for the dose range 8 - 10 kGy and for the dose of 3 kGy (see also Section 6.1). Looking at the trend of α_{rad}/D, it seems reasonable to assume that this would still be true for all dose ranges.

5.2.2 Dose rate dependent degradation

The X-ray tests for the quality assurance are performed with a dose rate of 23 Gy/min. Two fibre samples were irradiated with a lower dose rate of 5 Gy/min. This was achieved by introducing a 0.17 mm thick layer of aluminium between the beam outlet and the fibre under test. As shown in Fig. 4.16 the main consequence of introducing an aluminium filter is the absorption of low energy photons. Therefore also the energy distribution of the X-rays incident on the fibre is shifted towards higher energies. The maximum energy of the X-rays is always 40 keV, whereas the mean energy changes from 16 keV (no aluminium filter, dose rate 23 Gy/min) to 21 keV (0.17 mm aluminium filter, dose rate 5 Gy/min).
The degradations of these two samples after a dose of 1 kGy were

$$\Lambda'/\Lambda_0 = 0.74 \pm 0.05,\ \alpha_{\text{rad}} = (1.0 \pm 0.2) \cdot 10^{-3}\,\text{cm}^{-1} \text{ and}$$

$$\Lambda'/\Lambda_0 = 0.73 \pm 0.05,\ \alpha_{\text{rad}} = (1.0 \pm 0.2) \cdot 10^{-3}\,\text{cm}^{-1},$$

respectively. Those results are perfectly compatible with the QA irradiation tests (see Section 4.3.2).

Also the irradiations to very small doses ($D \leq 500\,\text{Gy}$), presented in Sections 4.3.1.1 and 5.2.1, provided compatible results:

$$220\,\text{Gy},\ 23\,\text{Gy/min:}\ \Lambda'/\Lambda_0 = 0.85 \pm 0.06,\ \alpha_{\text{rad}} = (0.5 \pm 0.2) \cdot 10^{-3}\,\text{cm}^{-1},$$

415 Gy, 3.5 Gy/min: $\Lambda'/\Lambda_0 = 0.83 \pm 0.06$, $\alpha_{\text{rad}} = (0.5 \pm 0.2) \cdot 10^{-3}\,\text{cm}^{-1}$,

500 Gy, 23 Gy/min: $\Lambda'/\Lambda_0 = 0.84 \pm 0.06$, $\alpha_{\text{rad}} = (0.5 \pm 0.2) \cdot 10^{-3}\,\text{cm}^{-1}$.

An additional test on dose rate dependency for hadrons irradiations will be discussed in Chapter 6.

5.2.3 Annealing

Five fibre samples were used to study the time evolution of α_{rad} after irradiation with X-rays up to a dose of 1 kGy. Three of the these samples were exposed to a dose rate of 23 Gy/min, with the same settings as for the QA tests. For the other two samples an aluminium layer of 0.17 mm was placed between the beam outlet and the fibre to reduce the dose rate to 5 Gy/min. The irradiation of the fibres and the consequent annealing took place in normal laboratory atmosphere at constant room temperature. Differently from the case of hadrons irradiations, which induce a permanent damage, the samples completely recovered with a time scale of about one month. No significant difference was seen between the five tested samples. A typical time evolution of the induced absorption is shown in Fig. 5.9. An extremely rapid annealing can be seen in the very first minutes after irradiation. Within less than 10 minutes, the attenuation length increases from $\Lambda' = 0.51 \cdot \Lambda_0$ to $\Lambda' = 0.71 \cdot \Lambda_0$ and the additional damage decreases from $\alpha_{\text{rad}} = 2.7 \cdot 10^{-3}\,\text{cm}^{-1}$ to $\alpha_{\text{rad}} = 1.1 \cdot 10^{-3}\,\text{cm}^{-1}$. Afterwards, the recovery slows down and the absorption remains stable for several hours. Therefore the values of α_{rad} as a function of time are fitted with a double exponential:

$$\alpha_{\text{rad}}(t) = p \cdot e^{-t/\tau_1} + (1-p) \cdot e^{-t/\tau_2} \tag{5.2}$$

For the tested samples, τ_2, which is the time constant accounting for the fast recovery, amounts to 1.3 - 1.8 minutes, while τ_1, which accounts for the slow recovery, amounts to 11 - 16 days.
The initial recovery is so fast that it can not really be measured with the described setup (Section 4.1), because the fibre is annealing faster than the attenuation length measurement is performed. Throughout this thesis, whenever a measurement of the attenuation length “just after the irradiation” is quoted, it is implied that the fibre was measured as soon as the short term annealing was completed. For QA fibres “just after the irradiation” corresponds to about 10 minutes after irradiation.

It should be noted that the time scale for the annealing shows a strong dependency on the total absorbed dose. For example, a fibre sample irradiated with the same tube settings as for the QA tests, but up to a total dose of 10 kGy, was measured two months after irradiation and the fibre was still significantly damaged. The measured values were:

$\Lambda'/\Lambda_0 = 0.51 \pm 0.04$, $\alpha_{\text{rad}} = (2.7 \pm 0.3) \cdot 10^{-3}\,\text{cm}^{-1}$ just after irradiation and

$\Lambda'/\Lambda_0 = 0.64 \pm 0.05$, $\alpha_{\text{rad}} = (1.6 \pm 0.3) \cdot 10^{-3}\,\text{cm}^{-1}$ after two months.

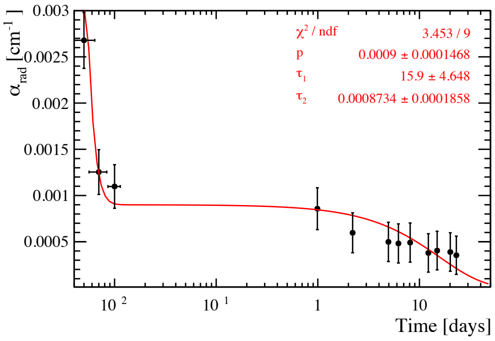

Figure 5.9: Time evolution of the induced damage after irradiation up to a dose of 1 kGy.

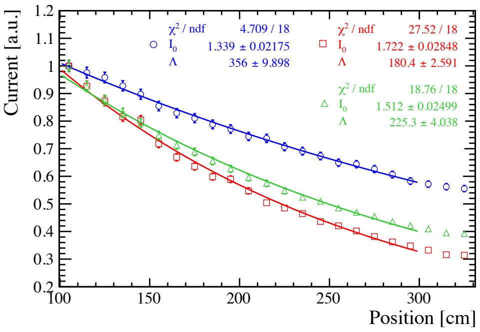

Figure 5.10: Attenuation length after irradiation up to a dose of 10 kGy. The blue circles correspond to the data measured before the irradiation, the red squares just after irradiation and the green triangles after 2 months.

The results of the attenuation length measurements are shown in Fig. 5.10. At this stage it can not be excluded that 40 keV X-rays can induce a permanent damage in the fibre, if the total absorbed dose is high enough.

5.2.4 Annealing in vacuum

Two fibre samples were used to test the contribution of oxygen to the annealing. For this purpose the samples were stored in vacuum atmosphere just after the irradiation. However both the irradiation and the measurements of the attenuation length had to be performed in normal laboratory atmosphere, i.e. the presence of oxygen could not be completely excluded. For both samples, as expected from the literature (see Section 2.3), the annealing was slower than if the samples were stored in normal atmosphere.

Both samples were stored in vacuum just after the irradiation. The first sample was kept in vacuum continuously for 34 days. The second sample stayed in vacuum for a total time of 61 days, interrupted to measure the attenuation length after 10, 19, 34 and 61 days. After each measurement the sample was immediately put back in vacuum atmosphere. The results of the measurements are shown in the plots in Fig. 5.11.

After 34 days the two samples had an attenuation length of $\Lambda' = (0.82 \pm 0.06) \cdot \Lambda_0$, corresponding to $\alpha_{\text{rad}} = (0.6 \pm 0.2) \cdot 10^{-3}\,\text{cm}^{-1}$, and $\Lambda' = (0.85 \pm 0.06) \cdot \Lambda_0$, corresponding to $\alpha_{\text{rad}} = (0.5 \pm 0.2) \cdot 10^{-3}\,\text{cm}^{-1}$, respectively. As discussed in Sections 4.1 and 4.3.2, the attenuation length is measured with an uncertainty of 5% and the error on the deterioration induced by irradiation is the result of the uncertainty propagation.

As a comparison, after 34 days the samples stored in normal lab atmosphere had $\Lambda' \geq 0.9 \cdot \Lambda_0$ and $\alpha_{\text{rad}} \leq (0.3 \pm 0.2) \cdot 10^{-3}\,\text{cm}^{-1}$, which is compatible with zero within 1.5σ. After 61 days the attenuation length of the second sample still

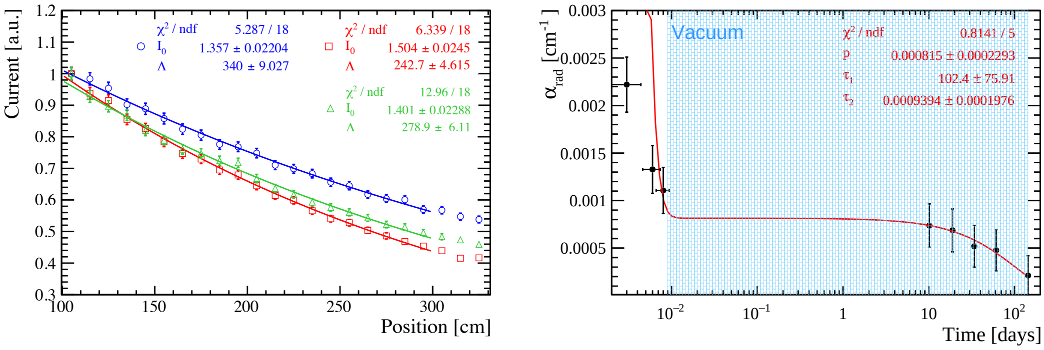

(a)

(b)

Figure 5.11: Time evolution of the induced damage after irradiation up to a dose of 1 kGy. The annealing took place in vacuum, while the irradiation and the attenuation length measurement were performed in normal lab atmosphere. The first sample (a) was kept in vacuum continuously for 34 days (the blue circles correspond to the data measured before the irradiation, the red squares just after irradiation and the green triangles after 34 days). The second sample (b) was stored in vacuum for a total time of 61 days, interrupted by attenuation length measurement.

amounted to $\Lambda' = (0.86 \pm 0.06) \cdot \Lambda_0$ and $\alpha_{\text{rad}} = (0.5 \pm 0.2) \cdot 10^{-3}\,\text{cm}^{-1}$, which is still more than 2σ away from zero.

5.2.5 Effect of the irradiation on the light yield

The effect of the X-ray irradiation on the light yield has been studied with two different tests, discussed in detail in the following.

For the first test a light yield sample composed by three 3.5 m long fibres was prepared and measured as described in Section 4.2. The resulting value for the light yield was 12.2 ± 0.5 p.e.. The three fibres were then individually irradiated in the X-ray setup, before being measured again for their light yield. The dose absorbed by each fibre was 1 kGy and the dose rate 23 Gy/min. The attenuation length of each fibre was measured before and after the irradiation: the induced decrease of the attenuation length was in line with the expectations (on average from the quality assurance tests: $\Lambda'/\Lambda_0 \sim 72\%$). The light yield measurement was repeated some days after the irradiation, to allow for a partial annealing of the fibres.

The three fibres were not irradiated simultaneously. However they were irradiated one after the other with a delay of only 45 minutes, which is the time needed to reach a dose of 1 kGy. The dose and dose rate were chosen so that:

- at any time the three fibres have similar attenuation lengths
- the attenuation length of each fibre does not change by more than 3% due

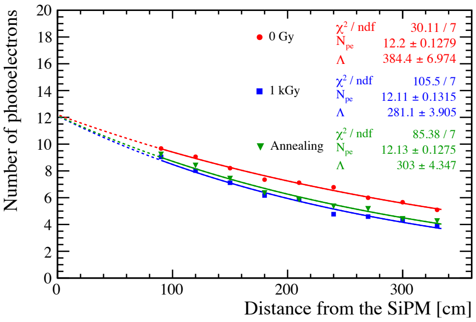

Figure 5.12: Fit to determine the light yield for a sample of three fibres before irradiation (red circles), directly after irradiation up to 1 kGy (blue squares) and after some days of annealing (green triangles).

to annealing during the time needed for the light yield measurement (about 6 hours)

The result is shown in Fig. 5.12. As expected, the attenuation length of the sample, i.e. the slope of the exponential curve, is affected by the irradiation. Nevertheless the extrapolation to a distance $d = 0$, which corresponds to the value of the light yield, remains constant.

The second test was performed with one sample composed by three 40 cm long fibres. The three fibre ends were glued together in a connector and machined with the diamond tool as for the light yield test. The number of photoelectrons at 30 cm was measured with the light yield setup. The fibres were locally irradiated with the X-ray setup. Only a 8 mm long segment was irradiated. Four irradiations were performed up to a total dose of 10 kGy, 20 kGy, 40 kGy and 250 kGy. The light output at 30 cm was measured after each irradiation. Only the fibres' segments at 30 cm from the readout extremity were exposed to the X-ray beam, while the rest of the fibres did not absorb any dose. In this way the damage to the scintillation mechanism could be evaluated, without any contribution from the degradation of light transport. A sketch of the layout is shown in Fig. 5.13(a).
In order to locally irradiate with very high dose rates, whilst sparing the rest of the fibres, the sample was directly fixed on the shielding of the X-ray tube as shown in the picture in Fig. 5.13(b). Dosimetry was carried out with Gafchromic HD-810 films. A picture of the film directly facing the beam outlet can be seen in Fig. 5.13(c). The beam spot has an oval shape, 8 mm high and 15 mm long. Other dosimetric films were placed in contact with the parts of the fibres that should not absorb any dose. The dose rate was (21.7 ± 2.6) Gy/s on the irradiated segment and compatible with zero on the remaining length of the fibre.
The result of the test is shown in the plot in Fig. 5.14, where the light output after each irradiation is normalised to the value before irradiation. The error on the number of measured photoelectrons is about 4%. Even after 250 kGy the light yield mechanism is not significantly damaged.

(a) (b) (c)

Figure 5.13: Light yield test after local irradiation up to 250 kGy. (a) Sketch of the layout. (b) A picture of the fibre sample fixed on the X-ray tube during irradiation. (c) A picture of a irradiated dosimetric HD-810 film. The film was fixed on the tube shielding in correspondence with the beam outlet.

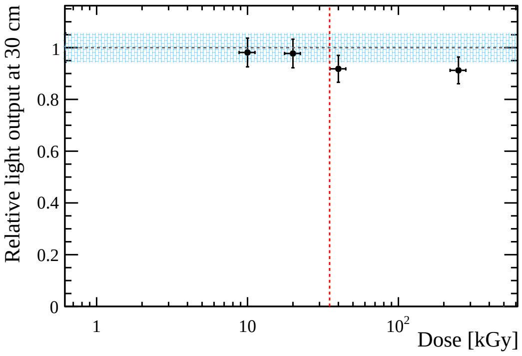

Figure 5.14: Light output at 30 cm at various doses, normalised to the value measured before irradiation. The horizontal grey line and the light blue dashed area represent the light yield before irradiation and its error. The vertical red line corresponds to the maximum dose in the SciFi Tracker after 50 fb^{-1}.

Chapter 6

Low dose irradiations

Most of the tests mentioned in Section 3.4.1 to estimate the radiation hardness of SCSF-78 fibres were performed at accelerators and therefore with very high dose rates. A high dose rate is clearly necessary in order to reach, within a manageable amount of time, the very high doses expected in the SciFi Tracker after 10 years of operations. However, the real dose rate at the LHCb will be smaller by several orders of magnitude. Some of the several studies about radiation resistance of plastic scintillators reported that high dose rate tests might underestimate the damage induced by low dose rate experiments (see Chap. 2). It was therefore mandatory to evaluate the response of SCSF-78 fibres to low dose rate irradiations. Two tests are described in this chapter: the first took place in the LHCb tunnel, whilst the second used ^{106}Ru plaques, normally used to treat eye cancer.

6.1 *In situ* irradiation

Several fibres were left close to the beam pipe in the LHCb tunnel in order to study the effect of low dose irradiation from hadrons. The *in situ* irradiation provides a measurement of the degradation after the exposure to the correct particle type and energy (multi-GeV hadrons) and to a similar dose rate as in the real LHCb detector. It is therefore an important test to study the radiation hardness of the SciFi Tracker. The drawback is that only relatively small doses can be obtained within an acceptable amount of time. In this case after about one year close to the beam pipe, the average dose absorbed by the fibres was about 3 kGy, i.e. about a factor 12 smaller than the maximum dose of 35 kGy in the SciFi Tracker.

This section describes the setup used to measure the attenuation length after the irradiation and the procedure followed to analyse the data. Finally the obtained damage is compared to other irradiation campaigns up to the same dose, but with different conditions.

Figure 6.1: A sketch and a picture of the two bundles of 1.3 m long fibres glued on a light support. For clarity purposes, only 3 fibres per bundle are drawn in the sketch. In reality each bundle consists of a dozen of fibres.

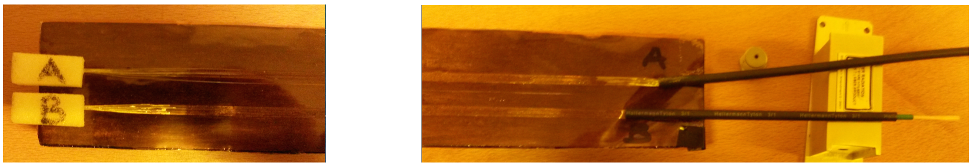

Figure 6.2: The fibres are loose at one extremity (right picture), while at the other extremity they are glued in a polystyrene foam end piece (left picture).

Sample description

Two bundles of 1.3 m long fibres were glued on a light support in a previous work [76]. The bundles are shown in Fig. 6.1. At one extremity the fibres are glued in polystyrene foam end pieces, at the other extremity they are loose (Fig. 6.2). The two bundles were labelled “A” and “B” for clarity purposes. During the irradiation an alanine dosimeter was glued at each extremity of the support. The bundles were placed along the beam pipe in the LHCb tunnel as in Fig. 6.3 from February 2012 till March 2013. After this period the alanine dosimeters were removed from the support and read out. They recorded a dose of 3.0 kGy and 3.6 kGy respectively. In September 2015 the fibres were studied in order to quantify the damage due to the irradiation. It is possible that some annealing processes took place during this more than two years long waiting period. The values of α_{rad}, determined with the analysis described in the following, correspond to the permanent damage induced on the fibres.

Setup to measure the attenuation length

Since the fibres were glued together on a support, the setup described in Section 4.1 could not be used to measure the attenuation length. Moreover, the presence of the polystyrene endpiece implies that all the fibres in one bundle had to be read out at the same time. In order to perform this measurement a UV-LED (390 nA) was fixed on a metal support, so that it could be moved both in the transversal and in the longitudinal direction with respect to the fibres. The distance between the LED and the fibres was about 2 cm, which resulted in a light spot on the fibres

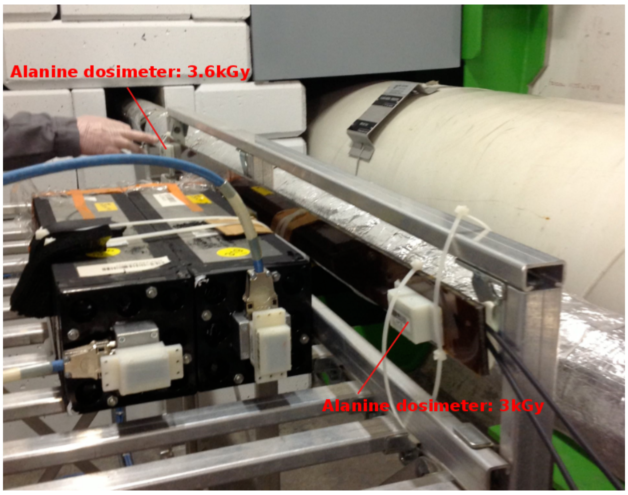

Figure 6.3: The location of the fibres and of the two alanine dosimeters along the beam pipe in the LHCb tunnel.

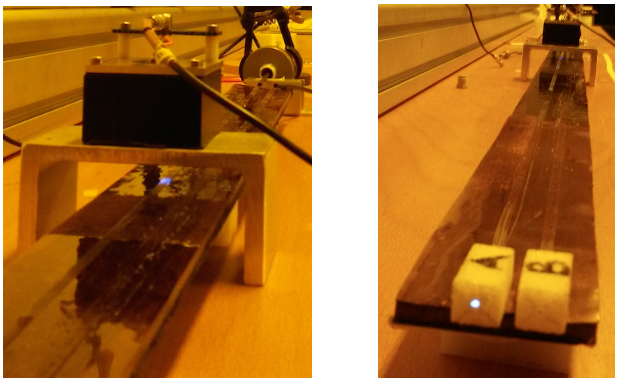

Figure 6.4: Two pictures of the setup to measure the attenuation length. The UV-LED is mounted on a movable metal support at 2 cm distance from the fibres. The light spot has a diameter of about 5 mm, so that all the fibres in a bundle are excited at the same time.

of about 5 mm diameter. This was enough to excite all the fibres in a bundle at the same time (Fig. 6.4). For each excitation point the LED was moved transversally to the fibres in order to have the LED centred with respect to the bundle. Only the highest value of the intensity was recorded.

Analysis

To measure the attenuation length the same procedure described in Section 5.1 is used. The plots in Figs. 6.5 and 6.6 show the result from the forward and backward measurement and the fit to the ratio. The sections of the fibres which are not covered by glue are highlighted in Fig. 6.5 with green shaded areas. In these sections the measured photocurrent is higher because the UV photons are

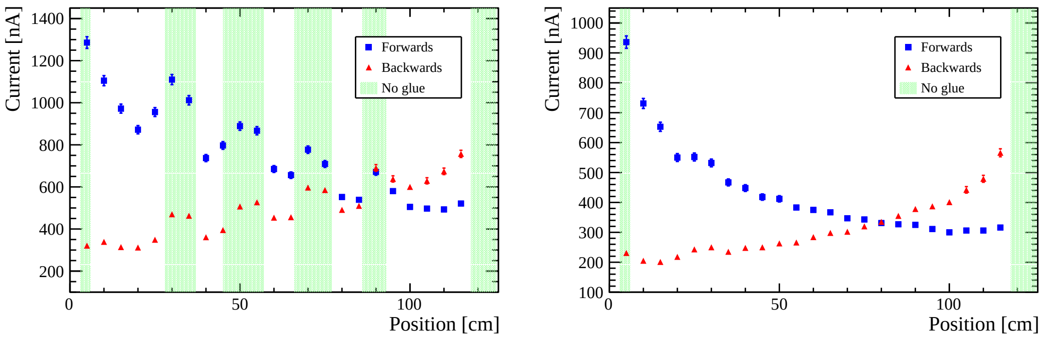

(a) Bundle A

(b) Bundle B

Figure 6.5: The measured photocurrent as a function of the distance from the PIN diode for the “forward” and “backward” direction for bundle A (a) and bundle B (b). The green shaded areas represent the sections of the fibres which are not covered with glue.

not dimmed by the glue. In the regions covered by glue the curves are not perfect exponentials, neither for bundle A nor for bundle B, because the thickness of the glue layer is not uniform along the length of the bundle. Nonetheless when taking the ratio the exponential behaviour is recovered and the attenuation length can be evaluated as in equation 5.1. Since the fibres are only 133 cm long the fit is performed between 15 and 115 cm. The resulting absorption coefficients amount to $\alpha'_A = (7.5 \pm 0.4) \cdot 10^{-3}\,\mathrm{cm}^{-1}$ and $\alpha'_B = (7.8 \pm 0.4) \cdot 10^{-3}\,\mathrm{cm}^{-1}$, for bundle A and bundle B respectively.
There is a complication arising from the used fitting ranges. As discussed in Chapter 2 and Section 4.1, there are photons which travel through the fibre following helicoidal paths. With respect to meridional rays produced from the same excitation point, the helicoidal photons cover a longer path and are subject to a higher number of reflections at the cladding surface before they reach the photodetector. In SCSF-78 fibres at a distance of 1 m from the readout extremity, they are already so attenuated that their contribution to the slope of the exponential curve is negligible. This is the reason why the fit is usually performed between 1 and 3 m from the photodetector. In this case, however, the length of the fibres is too short to avoid the contribution of the helicoidal photons. As shown in the following (Fig. 6.7) also fitting a double exponential in the range 15 - 115 cm does not help in retrieving the real attenuation length. A single exponential is therefore used, and the value obtained from the fit is an effective attenuation length, shorter than the real one.

In order to determine the value of α_{rad} the attenuation length before the irradiation would be needed. Unfortunately, it was not possible to perform this measurement in the time at disposal. For this reason another fibre had to be used for the analysis. A non irradiated reference fibre from the same production year

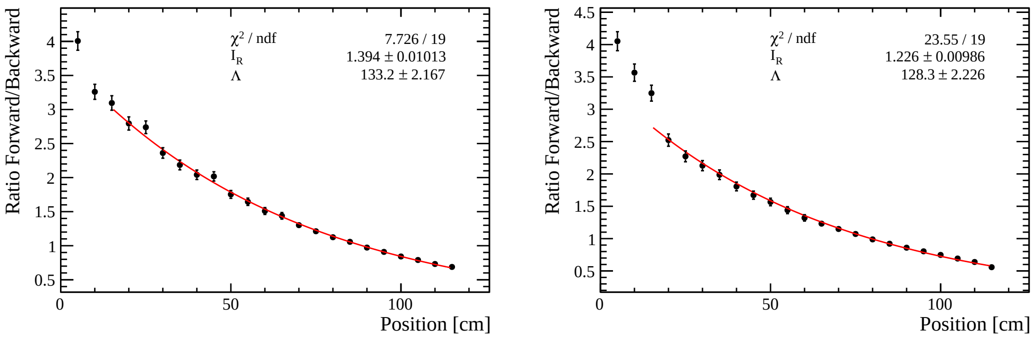

(a) Bundle A (b) Bundle B

Figure 6.6: The ratio of the "forward" and "backward" measurement for bundle A (a) and bundle B (b). The value of the attenuation length is obtained fitting the data with the function in equation 5.1.

was considered.

The attenuation length of this reference fibre, with the non-readout extremity blackened with Aquadag and the fit performed between 100 and 300 cm, amounts to 357 cm (Fig. 6.7). As discussed above, the result is affected by the choice of the fit ranges. The same fibre fitted in the range 15 - 115 cm provides a value of 206 cm when fitted with a single exponential (Fig. 6.7(a)) and of 256 cm when fitted with a double exponential (Fig. 6.7(b)). In both cases the effective attenuation length is significantly shorter than the real one.

Also the presence or not of the Aquadag have an influence on the fit, because the blackening of the non-readout extremity avoids rear reflection of photons into the fibre. In order to have a good comparison to the irradiated bundles, the reference fibre was cut to a length of 133 cm and measured without using Aquadag. The result of a single exponential fit is an attenuation length of 286 cm as shown in Fig. 6.7(a). This is the value used as α_0 in the following analysis.

An error of 15% is assigned to the attenuation length of the reference fibre in order to take into account the fact that different samples are considered for the evaluation of α_{rad}. The additional absorption coefficients due to the irradiation are:

$$\begin{aligned} \alpha_{\text{rad}}(\text{bundle A}) &= (4.0 \pm 0.6) \cdot 10^{-3}\,\text{cm}^{-1} \\ \alpha_{\text{rad}}(\text{bundle B}) &= (4.3 \pm 0.7) \cdot 10^{-3}\,\text{cm}^{-1} \end{aligned} \tag{6.1}$$

The spectral analysis was also performed, although the evaluation of the damage is not straightforward. The complication arises because only the loose fibres could be easily measured with the spectrometer, while the alignment between the bundle glued in the polystyrene endpiece and the lens in front of the clear fibre would have been too inaccurate. For this reason only two fibres of bundle B were measured with the spectrometer placed at the loose end. Contrary to the

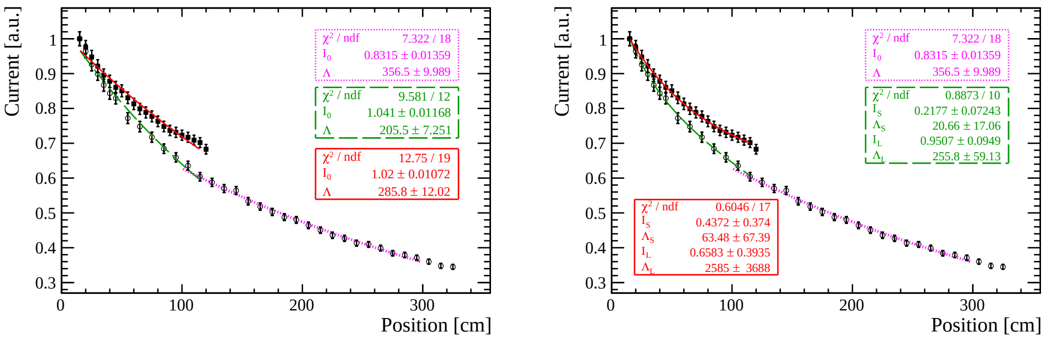

(a) (b)

Figure 6.7: Current as a function of the distance from the PIN diode for a 350 cm long reference fibre with Aquadag (black empty dots). The black full squares represent the current as a function of the distance from the PIN diode for the same fibre after cutting it to a length of 133 cm and without Aquadag. Both curves are normalized, so that the current at 15 cm is equal to 1. (a) A single exponential fit is performed in the ranges 100 - 300 cm (dotted magenta line) or 15 - 115 cm (dashed green line and straight red line). (b) A double exponential fit ($\mathrm{I}(x) = \mathrm{I}_S \cdot e^{-x/\Lambda_S} + \mathrm{I}_L \cdot e^{-x/\Lambda_L}$) is performed in the ranges 15 - 115 cm (dashed green line and straight red line).

measurement with the PIN diode, the fibres were read out individually. Bundle B was chosen over bundle A, because of the better uniformity of the glue. In fact, fitting a single exponential individually to the forward and backward curves of bundle B is still possible, although less accurate than considering the ratio. In order to account for this an additional error of 10% is assigned on top of the errors described in Section 4.1.1. To evaluate $\alpha_{\mathrm{rad}}(\lambda)$ the same non irradiated reference fibre was used as for the integral measurement. The result is shown in Fig. 6.8(b).

Comparison with other irradiation tests

The damage induced by irradiation to the scintillating fibres may depend on several factors. Not only the final absorbed dose, but also the dose rate, the type of radiation and the presence or not of oxygen during irradiation might play an important role. Fixing one of the several free parameters may be helpful to better understand the fibres' response in different environments. In this case a comparison could be done between fibres irradiated up to the same dose of about 3 kGy, but with very different dose rates and different radiation sources. One of the considered sample, mentioned in Table 3.3, was irradiated in the PS beam with a dose rate of $2.3 \cdot 10^4$ Gy/h. The first measurement of this sample was performed seven days after the irradiation and then repeated several times within a period of a year. No significant trend was seen, therefore the measured damage is considered to be permanent.

The second sample was irradiated with the X-ray setup described in Section 4.3.2

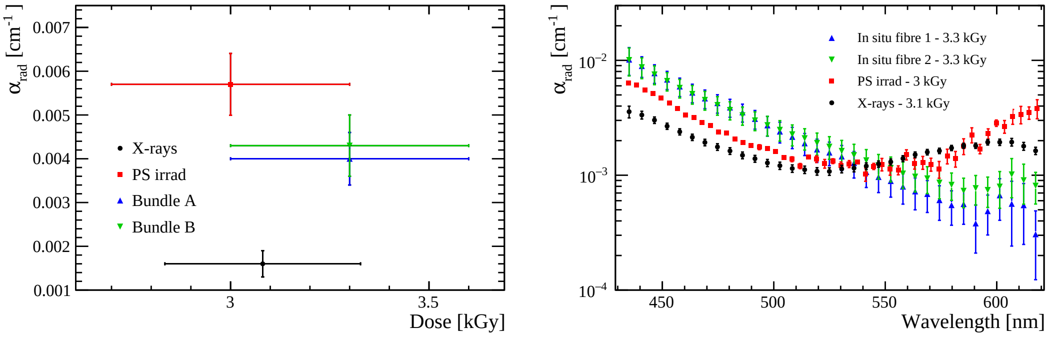

(a) PIN diode (b) Spectrometer

Figure 6.8: Comparison of the results of three different irradiation campaigns up to a dose of about 3 kGy.

with a dose rate of $1.4 \cdot 10^3$ Gy/h. In this case the value of α_{rad} presented here corresponds to the initial damage, measured just after the irradiation.

The results are presented in Fig. 6.8 and summarised in Table 6.1.

Two information can be extracted from the comparison of these tests. First of all it is once again confirmed that the damage caused by exposure to X-rays is smaller than the one induced by hadrons. In Section 5.2.3 it was shown that the time evolution of the damage caused by hadron or X-rays is different. The numbers in Table 6.1 reveal that also the severity of the deterioration is not comparable.

Furthermore this comparison gives an insight into the question of the dose rate effect raised in Section 2.3. The only dissimilarity between the irradiation in the PS and in the LHCb tunnel concerns the dose rates, which are 5 orders of magnitude apart. The challenges faced during the analysis of the *in situ* irradiated sample (shortness of the fibres, pollution with glue, impossibility of performing a forward-backward measurement with the spectrometer, lack of pre-irradiation measurement) should not be forgotten. The lack of pre-irradiation measurement was accounted for by attributing an error of 15% to Λ_0, instead of the usual 5%. Also the impossibility of performing a forward-backward measurement with the spectrometer is taken into account by assigning an additional error of 10%. The compatibility of the results of bundle A and bundle B suggests that the glue pollution is negligible when the ratio between forward and backward measurement is considered. It is however difficult to quantify the effect given by the shortness of the fibres, i.e. by the contribution of the non-meridional photons. Therefore this last source of uncertainty is not accounted for in the final results. Despite these complications, the compatibility of the permanent damages induced by the PS and *in situ* experiments suggests that no significant dose rate effect exists for SCSF-78 fibres exposed to high energetic hadrons irradiation.

Radiation source	**Dose** [kGy]	**Dose rate** [Gy/h]	α_{rad} [cm^{-1}]	α_{rad}(450 nm) [cm^{-1}]
24 GeV/c protons	3.0 ± 0.3	$2.3 \cdot 10^4$	$(5.7 \pm 0.7) \cdot 10^{-3}$	$(4.7 \pm 0.3) \cdot 10^{-3}$
40 keV X-rays	3.1 ± 0.2	$1.4 \cdot 10^3$	$(1.6 \pm 0.3) \cdot 10^{-3}$	$(2.7 \pm 0.2) \cdot 10^{-3}$
mostly MIP hadrons	3.3 ± 0.3	$\sim 2 \cdot 10^{-1}$	$(4.0 \pm 0.6) \cdot 10^{-3}$ $(4.3 \pm 0.7) \cdot 10^{-3}$	$(6.6 \pm 1.2) \cdot 10^{-3}$ $(6.8 \pm 1.2) \cdot 10^{-3}$

Table 6.1: Summary of the irradiation campaigns up to 3 kGy. It should be kept in mind that the values reported in the table correspond to the permanent damage for the hadrons irradiations (PS and *in situ*) and to the initial damage, before annealing, for the X-ray irradiation.

6.2 ^{106}Ru irradiation

The aim of this experiment was twofold. The first goal was to test the absorption induced in SCSF-78 fibres after exposition to a low dose rate source and compare it to the effect from high dose irradiations. In addition, the idea was to study the transmission loss during irradiation.

At first it was proposed to use an isotropic ^{90}Sr source. However, irradiating a 3 m long fibre with a punctual source up to a dose of about 100 Gy would require a huge amount of time. A solution to this problem was found in the field of medical applications. Ophthalmic plaques, used to treat eye tumours, have a semi-spherical shape with diameters from 12 to 20 mm. The sources and their dose rate distribution, together with the experimental setup and the obtained results, are described in the following.

Sources

Four eye applicators of type CCB and CCD produced by the company Bebig[1] were used. Their geometry is optimised to treat eye cancers, in particular uveal and choroidal melenomas. Their shape is semi-spherical as shown in Fig. 6.9. CCB and CCD applicators only differ in their size: the firsts have a diameter $D = 20.2$ mm and a height $h = 5.4$ mm, while the latters have $D = 17.9$ mm and $h = 4.3$ mm. For both types the curvature radius R amounts to 12 mm.

The applicators consist in a thin film of ^{106}Ru, encapsulated in silver. The radioactive layer is deposited on the concave surface of a 0.2 mm thick silver foil. The radiation window on the concave side is a 0.1 mm thick silver foil. The 0.7 mm thick silver backing acts as a shield, absorbing 95% of the radiation in the backward direction and easing the handling of the plaque.

Ruthenium-106 is a β-emitter through the decay $^{106}\mathrm{Ru} \rightarrow ^{106}\mathrm{Rh} + e^- + \overline{\nu}$, with a half-life of 374 days. Those electrons have a maximum energy of 39 keV and can

---

[1] Eckert&Ziegler BEBIG, www.bebig.com

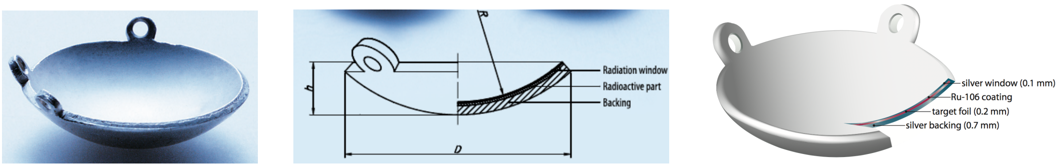

(a) (b) (c)

Figure 6.9: Representation of an ophthalmic plaque of type CCB or CCD.

not escape the silver window in the applicator. The β particles used for cancer treatment come from the decay of ^{106}Rh to the stable isotope ^{106}Pd with a half-life of 30 seconds. The β distribution extends till a maximum energy of 3.5 MeV, with a mean energy of 1.4 MeV [77].

Dose rate distribution

At the time of the fibre irradiation test the four applicators had an overall activity of about 32 MBq. The dose rate distribution was measured with a dosimeter based on plastic scintillating fibres BC-400 produced by Bicron [78]. The maximum dose rate was registered in the middle point of the semi-sphere in contact with the applicator. It amounted to (69 ± 1) mGy/min and (64 ± 1) mGy/min for the CCB applicators and (101 ± 2) mGy/min and (76 ± 2) mGy/min for the CCD applicators, respectively.

The plots in Fig. 6.10(a) and 6.11(a) show the relative dose rate along the central axis of the semi-sphere as a function of the distance from the inner surface of the applicator. The plots in Fig. 6.10(b) and 6.11(b) show the relative dose rate distribution in steps of 1.5 mm on a plane normal to the semi-sphere axis at a distance of 9 mm from the inner surface of the applicator. In both cases the dose rate diminish when going further away from the middle point of the semi-sphere. On the plane at 9 mm distance the distribution is symmetrical around the central axis and still amounts to about 40 - 45% of the highest value in a circular spot with a diameter of about 10 mm, but it rapidly decreases to 15 - 20% at a distance of 10 mm from the centre.

Setup

Nine 7 m long fibres were wound on a plastic wheel provided with 9 grooves along the external surface (Fig. 6.12). The fibres were labelled with numbers from 1 to 9. The wheel was 5 cm high and with an external diameter of 25 cm. Each groove was 0.2 mm deep and 2.2 mm wide, so that exactly one fibre would fit in each groove. The wheel was provided with two holes, so that the two extremities of each fibre could be guided away from the wheel. It was immediately noted that the sharp edges on the wheel would damage the fibres creating kinks. Before starting the irradiation test

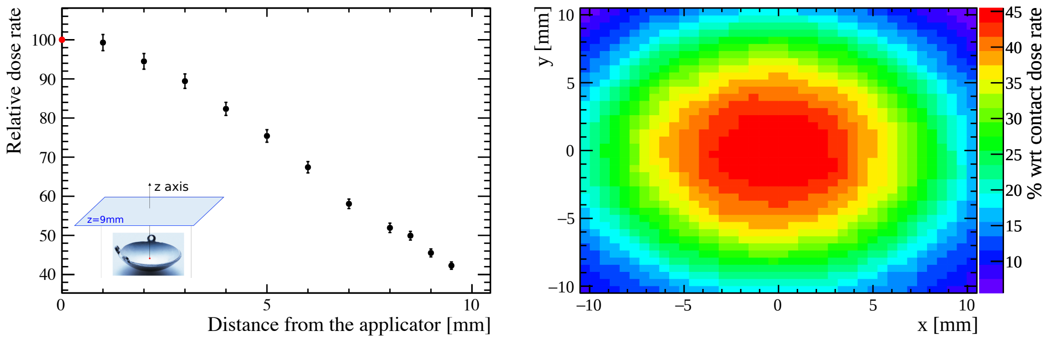

(a) Along the z axis

(b) On the plane at z = 9 mm

Figure 6.10: Dose distribution of one of the CCB applicators. All the values are normalised to the highest dose rate, measured in the middle point of the semi-sphere in contact with the applicator. The sketch shows the coordinate system valid for both plots.

the edges were smoothed with sandpaper. Unfortunately even after polishing, the fibres, tensioned on the wheel, were damaged in correspondence with the holes.

At one extremity the fibres were glued together in one bundle and read out with a spectrometer (Fig. 6.13). On the other side, the fibres extremities were glued on a plastic support at 3 cm distance from another. A UV LED was connected to a motor and moved along the support to alternatively excite each fibre. The distance between the fibre extremities on the support was such that the LED could only excite one fibre at a time, i.e. only one fibre at a time was read out by the spectrometer.

The four applicators were placed into two holders, with each holder carrying two applicators. They were then fixed to a rotating arm as in Fig. 6.14. The length of the arm, and therefore the height of the applicators with respect to the wheel, was chosen so that only the fibres 4 to 9 would be exposed to radiation, while fibres 1 to 3 were not irradiated and were used as reference fibres. The CCB applicators were centred in the vertical direction so that the centre of the semi-sphere would be halfway between fibre 6 and fibre 7. The CCD applicators, which have a slightly smaller diameter, were originally supposed to be centred at ±1 mm, respectively, with respect to the CCB plaques. They were however accidentally aligned both at +1 mm.
The applicators were placed at minimal distance from the surface of the wheel, in order to maximise the dose absorbed by the fibres. Due to the presence of 3 mm long eyelets on the applicators (originally meant to be sutured to the sclera) the minimal distance between the inner surface of the applicators in the middle point of the plaque and the fibres amounted to 9 mm. Based on the measurements described in the previous section, the fibres were exposed to the following dose

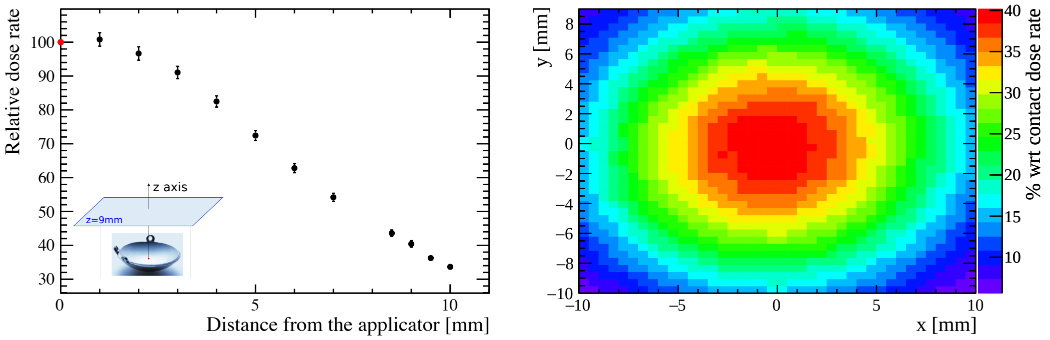

(a) Along the z axis

(b) On the plane at z = 9 mm

Figure 6.11: Dose distribution of one of the CCD applicators. All the values are normalised to the highest dose rate, measured in the middle point of the semi-sphere in contact with the applicator. The sketch shows the coordinate system valid for both plots.

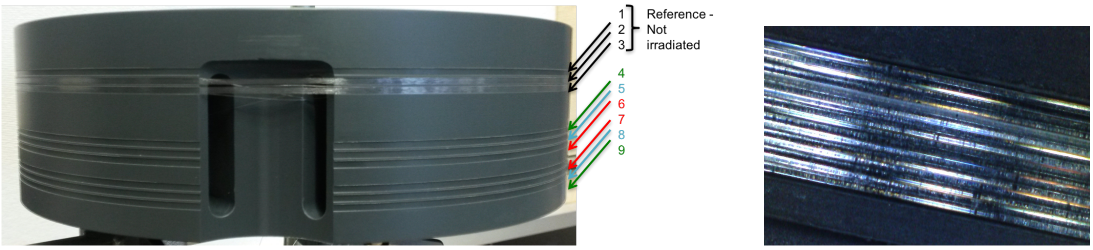

(a)

(b)

Figure 6.12: (a) The plastic wheel with 9 grooves. In this picture only two fibres (fibre 2 and fibre 3) are coiled around the wheel. (b) Detail of one fibre wound in a groove.

rates: 1.2 mGy/min (fibre 4), 1.7 mGy/min (fibre 5), 2.2 mGy/min (fibre 6), 2.1 mGy/min (fibre 7), 1.5 mGy/min (fibre 8) and 1.1 mGy/min (fibre 9).
Four cylindrical alanine dosimeters, with a length of 20 mm and a diameter of 4 mm, were set in ad hoc cavities dug in the wheel. Their readout after irradiation was used to cross-check the effective dose absorbed by the fibres. One of the dosimeters can be seen in the picture in Fig. 6.13(a).

The whole setup was placed in a closable wooden box. When closed, the box was completely light tight, so that the transmission loss measurement could be performed during irradiation without external background sources. In addition, a curtain made of heavy black tissue was placed between the LED and the wheel to avoid the incidental excitement of the fibres wound on the wheel. The position of the curtain in the wooden box is indicated by the dashed line in Fig. 6.13(b).

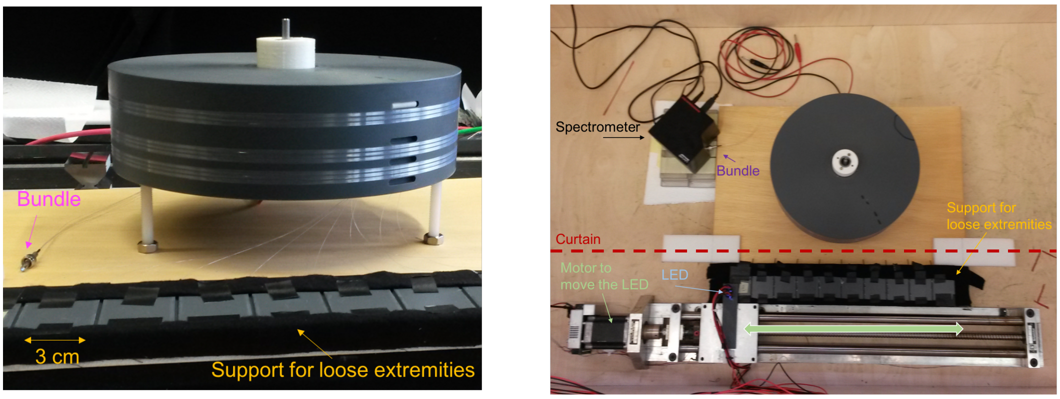

(a) Front view (b) Top view

Figure 6.13: At one extremity the fibres were glued in a bundle to be read out from the spectrometer. At the other extremity they were left loose and glued on a support at 3 cm distance from another. A UV LED, connected to a motor, excited each fibre singularly.

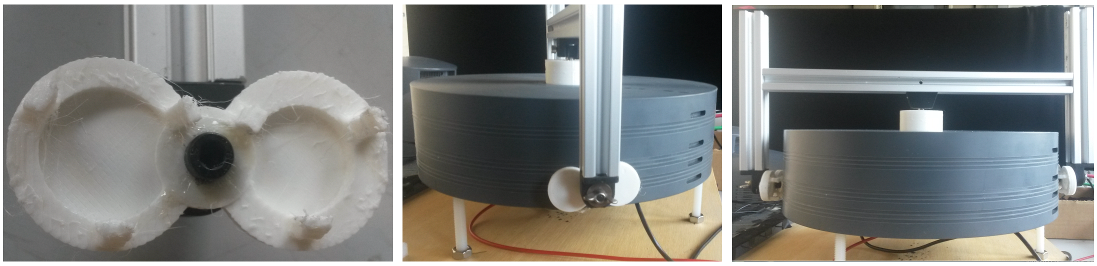

(a) (b) (c)

Figure 6.14: The applicators, placed into 3D-printed holders, were connected to a movable arm, rotating with constant speed around the wheel.

Results

The fibres were irradiated for 547 consecutive hours (approximately 23 days). At the end of this time they absorbed the following doses: 38 Gy (fibre 4), 56 Gy (fibre 5), 73 Gy (fibre 6), 69 Gy (fibre 7), 50 Gy (fibre 8) and 35 Gy (fibre 9).

The transmission loss was measured online during irradiation. As explained in the previous section, a LED alternatively excited every fibre at the fixed distance of 7 m from the spectrometer. The measurements were performed every hour and the obtained spectra saved in a laptop connected to the spectrometer. The original idea was to evaluate the transmission $\mathrm{T_x}$ of each fibre ($\mathrm{x} = 1, 2, \ldots 9$):

$$\mathrm{T_x}(\lambda, t) = \frac{\mathrm{I_{x,rad}}(d, \lambda, t)}{\mathrm{I_{x,b}}(d, \lambda)} = \frac{\mathrm{I_0}\, e^{-[\alpha_0(\lambda)+\alpha_{\mathrm{rad}}(\lambda,t)]d}}{\mathrm{I_0}\, e^{-\alpha_0(\lambda)d}} = e^{-\alpha_{\mathrm{rad}}(\lambda,t)d} \tag{6.2}$$

where $\mathrm{I_b}$ is the intensity before the irradiation, $\mathrm{I_{rad}}$ the intensity at any time

t during irradiation and d is the fixed distance between excitation point and spectrometer. In this way the evolution of α_{rad} as a function of time, i.e. of the absorbed dose, could have been measured. For the three reference fibres, which were not exposed to radiation, equation 6.2 should read $\mathrm{T}_{\mathrm{x}=1,2,3}(\lambda, t) = 1$ at any time t.
It was already mentioned that the fibres were damaged in correspondence with the wheel edges. Unfortunately, since the fibres were tensioned on wheel, the light loss at the kinks increased as the hours passed by. An example of the deterioration of one non irradiated fibre is shown in Fig. 6.15. As a consequence, equation 6.2 can no longer be used, because the kinks contribute to the transmission loss. However, it can be assumed that the degradation due to the mechanical damage alone is uniform for all the fibres. The validity of this assumption can be tested comparing the transmission of the reference fibres, which should be equal at any time:

$$\mathrm{T}_{\mathrm{ref}}(t) = \mathrm{T}_1(t) = \mathrm{T}_2(t) = \mathrm{T}_3(t) < 1, \text{ at any time } t \tag{6.3}$$

This is shown in Fig. 6.16(a), where $\mathrm{T}_3/\mathrm{T}_2$ is plotted at different times after the beginning of the irradiation. Then the normalised transmission

$$\mathrm{T}_{\mathrm{x,norm}}(t) = \frac{\mathrm{T}_{\mathrm{x}}(t)}{\mathrm{T}_{\mathrm{ref}}(t)} \tag{6.4}$$

only depends from the radiation damage. The results are shown in Fig. 6.16(b)-(d). For some fibres the intensity measured by the spectrometer was too small to perform a reasonable analysis, therefore only fibre 3 - 6 are shown. All the plotted fibres are normalised with respect to fibre 2. The intensity of all the fibres decreased with time. Therefore the curves measured after 23 days show stronger fluctuations than the ones measured after a few hours.
One hour after the start of the irradiation the absorbed dose is vary small (< 0.2 Gy) and $\mathrm{T}_{\mathrm{norm}}$ is very close to 1. As the time passes by, $\mathrm{T}_{\mathrm{norm}}$ of the irradiated fibres decreases until it saturates after 6 days. From this moment the transmission remains constant, or even recovers, denoting the presence of an annealing process.
The induced damage is wavelength dependent: in the region 450 - 470 nm no deterioration is recorded, but the transmission losses steadily increase with increasing wavelength till a local minimum at about 590 - 600 nm. The minimum normalised transmission amounts to 0.4 for fibre 4 and to 0.3 for fibre 5 and fibre 6. At any given time t, fibre 4, which is exposed to the smallest dose rate, is less damaged than fibre 5 and fibre 6.

The spectral attenuation length was measured 3 weeks after the end of the irradiation. As shown in Fig. 6.17, also in this case the analysis is affected by the presence of the kinks. Due to the light leaks at the kinks, the measured intensity as a function of the distance from the spectrometer results in a step function. The attenuation length can still be evaluated fitting with a step exponential function, with the requirement that the slope is always the same along the length

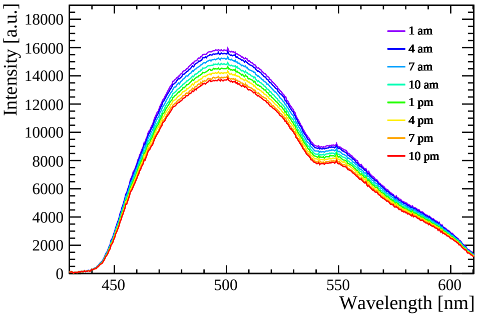

Figure 6.15: Time evolution of the emission spectrum for one of the reference fibre (fibre 2). The spectra were measured every hour. For clarity purposes in this plot only one measurement every 3 hours is shown. The reference fibres were not irradiated, i.e. the deterioration is purely due to mechanical damages of the fibre.

of the fibre. However the validity of this method strongly depends on the size and quantity of the light leaks. At a kink the photons are deflected from the original trajectory: some photons will leave the fibre and some photons can be reflected back into the fibre. If a kink is big enough, the fraction of reflected photons might be big enough to influence the slope of the exponential. Several tests were performed with flawless fibres, measured before and after intentionally damaging the fibre. In the worst cases, the attenuation length determined with the step function differ up to 30% from the real value.

Due to the light losses at the kinks, the intensity measured at big excitation distances ($\lesssim 3.5\,\mathrm{m}$) might become very weak. Therefore, although the fibres are 7 m long, the fits to extract the attenuation length are always performed between 1 and 3 m. A picture of a fibre after being removed from the irradiation wheel is shown in Fig. 6.18. Two kinks are clearly visible as bright blue spots.

Unfortunately the fibres used for the irradiation test could not be measured before being wound on the wheel, therefore a direct evaluation of the uncertainty introduced by the kinks is not possible. The absorption coefficient of the three reference fibres is shown in Fig. 6.19. In the following analysis the average and the standard deviation of the reference fibres absorption coefficients are used as α_0 and its error. The additional absorption coefficients for fibres 4, 5 and 6 are shown in Fig. 6.20. It is possible that the fibres further annealed to an almost complete recovery, however the error bars are too big to draw any definitive conclusion.

Discussion

The original idea behind this test was very ambitious, aiming at measurements both during and after the irradiation. The non optimal design of the irradiation wheel prevented from extracting all the desired information. However it could be verified that SCSF-78 fibres are affected by a wavelength dependent degradation: even a very small dose of 1 Gy induces a significant transmission loss at 590 -

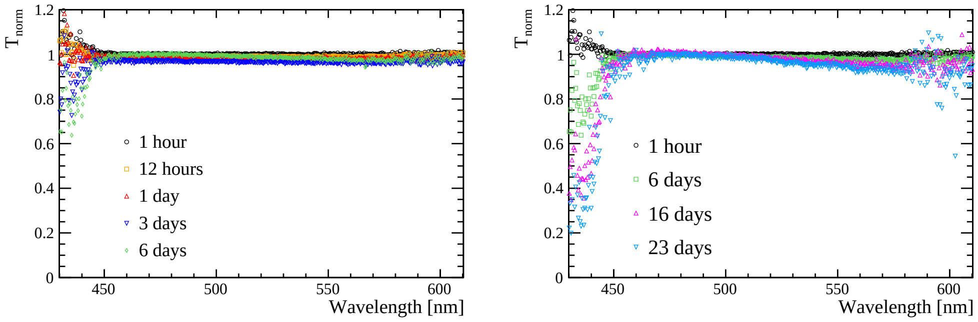

(a) Fibre 3 (reference fibre) normalised to fibre 2

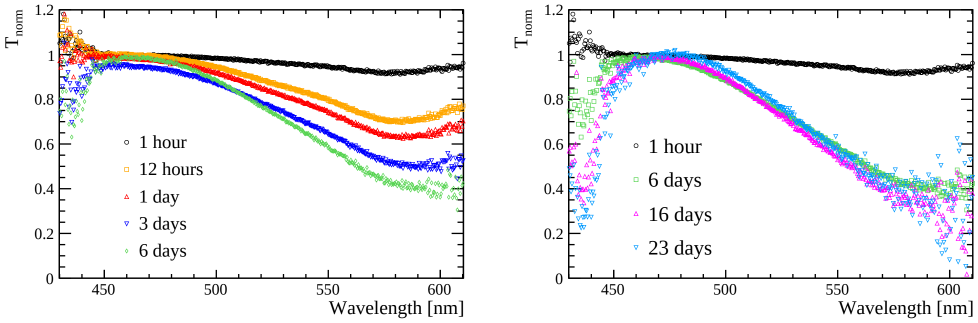

(b) Fibre 4 normalised to fibre 2

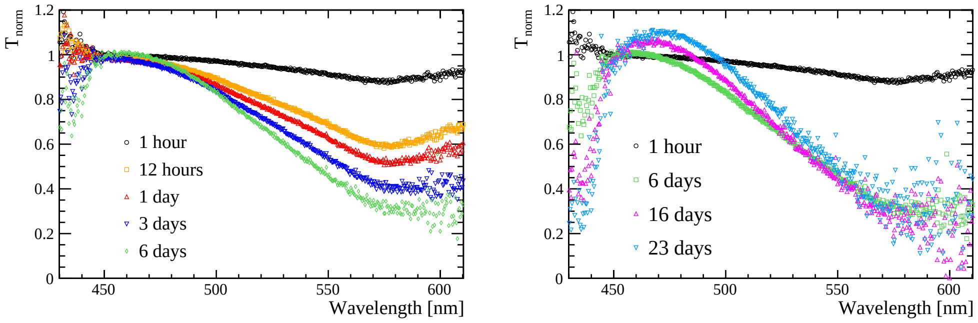

(c) Fibre 5 normalised to fibre 2

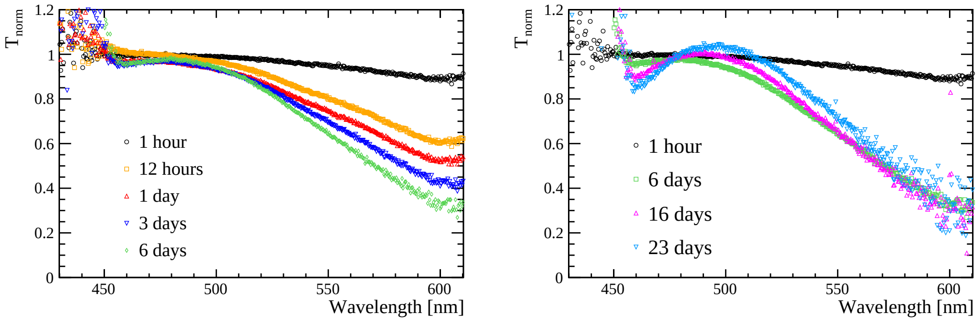

(d) Fibre 6 normalised to fibre 2

Figure 6.16: T_{norm} with respect to fibre 2. Each curve was obtained from the measurements at a time t after the start of irradiation ($t = 1\,\mathrm{h}, 12\,\mathrm{h}, 1\,\mathrm{d}, 3\,\mathrm{d}, 6\,\mathrm{d}, 16\,\mathrm{d}, 23\,\mathrm{d}$). The curves at 23 days correspond to the last measurement before stopping the irradiation.

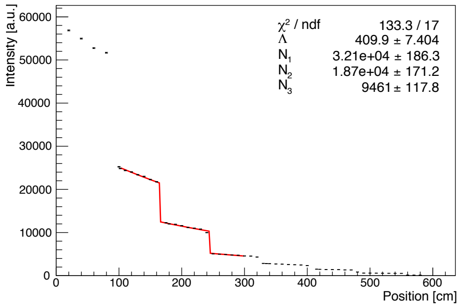

Figure 6.17: Fit to extract the attenuation length for one fibre at $\lambda = 450$ nm.

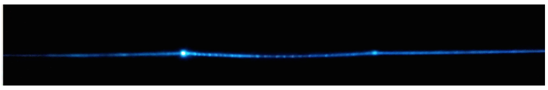

Figure 6.18: Picture of a fibre after removing it from the wheel. The fibre is excited with UV light to highlight the kinks (bright blue spots).

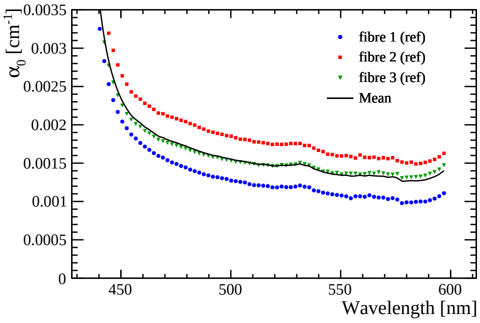

Figure 6.19: Absorption coefficient of the three reference fibres and their average.

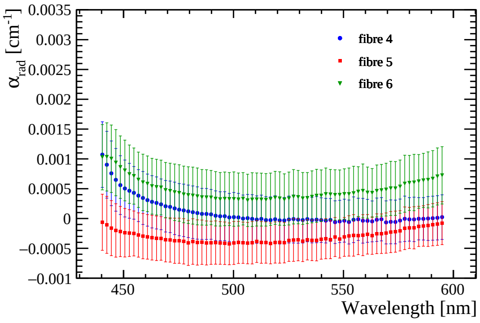

Figure 6.20: Additional absorption coefficient 3 weeks after the end of the irradiation.

600 nm, whilst the transport efficiency of photons with a wavelength of 450 nm seem to be unaffected even after 70 Gy.

The presence of a time dependent recovery process is recorded. As discussed in Chapter 2, the annealing takes place when the induced free radicals annihilate through interaction with other radicals. The more radicals are induced in the fibre, the easier two of them will enter in contact and recombine. It is therefore not surprising that at the beginning the recovery is slower than the induced damage, but it speeds up until eventually the recombination compensates the production rate of free radicals and the damage saturates. The time scale of these processes for SCSF-78 fibres exposed to dose rates of 1 - 2 mGy/min is such that the saturation occurs approximately after 6 days from the beginning of the irradiation, i.e. after a dose of 10 - 20 Gy.

The dose rate in the real LHCb detector ($\sim 10^{-1}$ mGy/min) will be even lower than the one in used in this experiment. Furthermore the particle type and energy are not the correct ones, however papers exist in the literature claiming that no difference was seen between irradiations with protons, electrons or γ-rays from a ^{60}Co source [24, 25]. Despite the fact that the annealing time scale during ^{106}Ru irradiation can not be directly transposed to the case of the SciFi Tracker, it

is reasonable to assume that SCSF-78 fibres in the LHCb detector will show a similar behaviour.
Finally, ophthalmic ^{106}Ru plaques have proved to be a valid option to expose a relatively large surface of about $1\,\mathrm{cm}^2$ to low dose rate β particles, with an energy of up to 3.5 MeV.

Chapter 7

Irradiation of a SciFi Module

As discussed in the previous chapters, several irradiation campaigns were performed on individual fibres and fibres bundles. The samples were irradiated up to different doses and the results were used to evaluate the damage over the full dose range relevant for the SciFi detector.
The aim of the experiment described in this chapter was the exposition of a SciFi module to a dose profile which resembles as much as possible the one in the upgraded LHCb detector after 10 years of operations. The module was characterised in test beams before and after the irradiation. The irradiation took place in one of the irradiation zones at IRRAD, the CERN PS irradiation facility [79]. The irradiation zones are traversed by the 24 GeV/c proton beam and are equipped with translation tables, which can be moved and rotated remotely, i.e. also during the irradiation.
This chapter describes the details of the module irradiation. The technique used to evaluate the effective dose absorbed by the module along its length is discussed in detail. Finally, the results of the dosimetry and of the test beam campaign are presented.

7.1 Layout

The module, consisting of a single six-layer fibre mat, was 2.5 m long and 13 cm wide. The fibre mat was sandwiched between two honeycomb panels reinforced with 200 μm thick carbon fibre sheets. On the readout side, the fibres were glued between two polycarbonate end pieces, held by two aluminium endplugs. On the non-readout side an aluminised mylar mirror was attached to the fibre ends with EPOTEK H301 epoxy glue.

The accelerated protons from the PS are delivered in spills, with each spill containing about $3.6 \cdot 10^{11}$ protons. The intensity of each extracted proton spill is monitored using a Secondary Emission Chamber (SEC) and the beam profile for each spill is visualised with custom-made Beam Profile Monitors (BPMs). Both the SEC and the BPMs are provided by the PS beam instrumentation

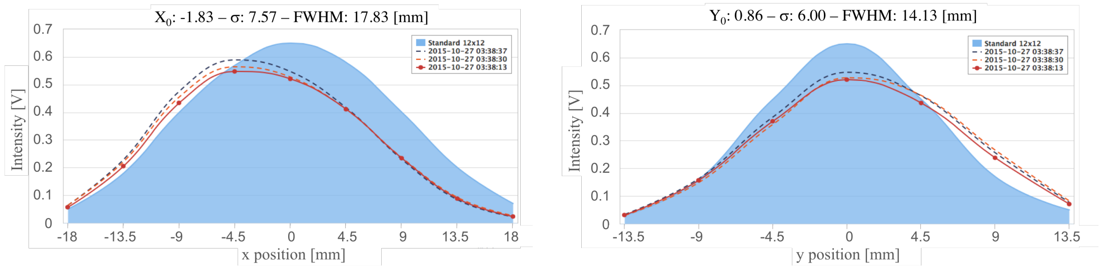

(a) Horizontal beam profile (b) Vertical beam profile

Figure 7.1: Beam profile measured by BPM3, located upstream of the SciFi module. The blue area in the plot shows the standard beam profile, while each line represent the actual beam profile measured by BPM3 for a specific spill.

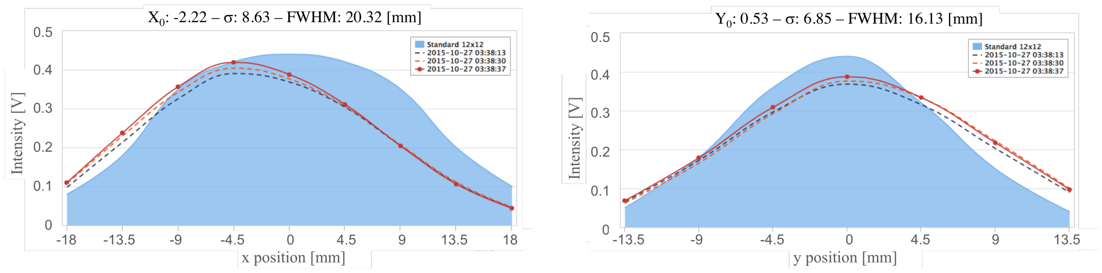

(a) Horizontal beam profile (b) Vertical beam profile

Figure 7.2: Beam profile measured by BPM4, located downstream of the SciFi module. The blue area in the plot shows the standard beam profile, while each line represent the actual beam profile measured by BPM4 for a specific spill.

team. The beam spot, which fluctuates in the range of a few millimetres both in position and in shape, has a roughly Gaussian shape with a width of $\sigma_x \approx \sigma_y = 7$-8 mm. Examples of beam profiles in the horizontal and in the vertical direction as measured by two BPMs, located respectively upstream and downstream of the SciFi module, can be seen in Figs. 7.1 and 7.2.

The space available in the irradiation zone did not allow to place the module orthogonally with respect to the beam. It was therefore placed on a translation table, tilted by 7° as shown in Fig. 7.3. The alignment was carried out with the help of a 3D laser system. In order to reproduce the same dose profile as in the upgraded LHCb detector, the module had to remain in a certain position for a previously determined number of spills. After the required number of protons hit the module, the table was remotely translated by 1 cm, without changing the relative angle between the module and the beam axis. This procedure was repeated until the full length of the module was exposed to irradiation. The determination of the number of spills for each table position relied on the knowledge of the average number of protons per spill ($3.6 \cdot 10^{11}$) and the energy loss of one minimum ionizing

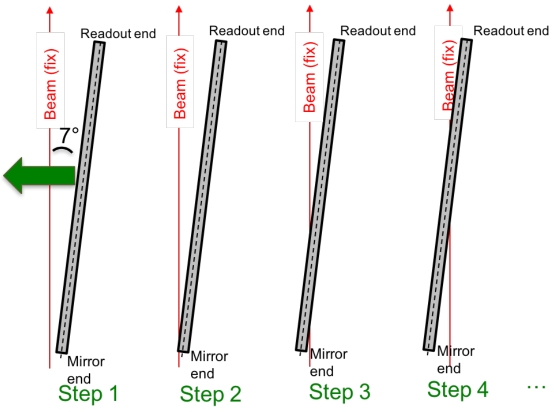

Figure 7.3: Principle of the positioning of the module in the PS beam.

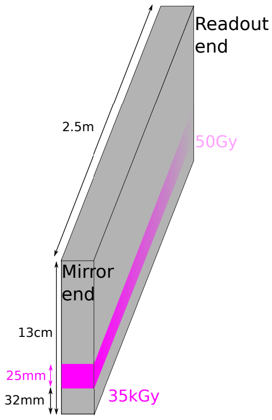

Figure 7.4: Representation of the irradiated zone on the module.

proton in polystyrene (1.936 MeV cm^2/g [80]). The details of the calculation can be found in Ref. [81]. Most of the positions were hold for only a few spills (≤ 5), whilst more than 2000 spills were required to obtain the very high dose at the mirrored end of the module.
As displayed in the sketch in Fig. 7.4, the irradiated zone corresponds to an approximately 25 mm wide band running along the module at 32 mm from its edge. The non irradiated parts of the module were used in the test beam experiment as reference zones.

7.2 Dosimetry

The dosimetry was based on the activation of aluminium and the colourisation of dosimetric films. Six aluminium bars were fixed on the module, three on the readout side and three on the mirrored side. All the bars were placed orthogonally to the beam as shown in Fig. 7.5. They were 35 cm long to cover, in the projection, the whole length of the module. The position along the aluminium strip is related to the position along the module by the relation $x_{\text{module}} = x_{\text{strip}}/\sin\vartheta$, where $\vartheta = 7°$ is the angle by which the module is tilted with respect to the beam.
The two middle strips, 25 mm high, were aligned with the beam and were used after the irradiation to evaluate the dose absorbed by the fibres. The four strips at the top and at the bottom were used to estimate the background. A Gafchromic dosimetric film was placed on top of each middle strip. The films were not used for quantitative dosimetry, but to visually cross-check the correct alignment of the module.

During irradiation the aluminium is activated via the nuclear reactions $^{27}\text{Al}(\text{p},3\text{p}3\text{n})^{22}\text{Na}$ and $^{27}\text{Al}(\text{p},3\text{pn})^{24}\text{Na}$. The produced radioactive isotopes, ^{22}Na and ^{24}Na decay with a half-life of 2.6 years and 15 hours, respectively.
The number of protons which hit the aluminium is related to the Na activity A_0

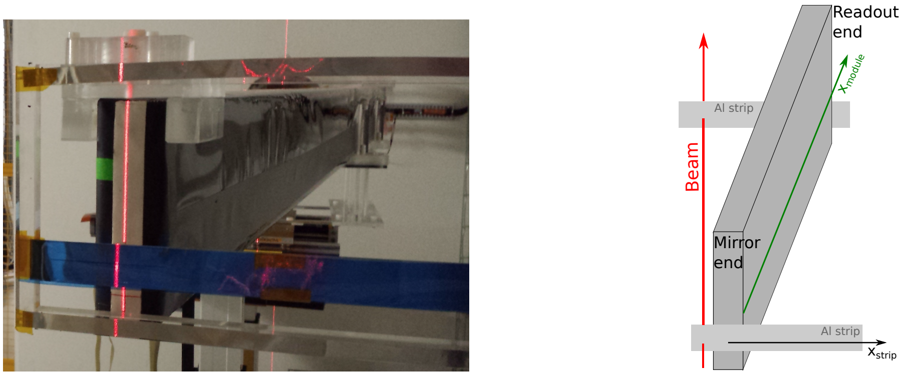

(a) (b)

Figure 7.5: A picture and a sketch of the module during irradiation with the aluminium bars used for the dosimetry. A Gafchromic dosimetric film was attached on top of the middle Al strip. For clarity purposes only the middle Al strips, which cover the irradiated zone, are displayed in the sketch.

at the end of the irradiation by:

$$\mathrm{N} = \frac{A_0\ \Delta t}{\sigma\ \frac{N_{av}\rho}{m}\ d\,(1 - e^{-\lambda \Delta t})} \tag{7.1}$$

where Δt is the duration of the irradiation, $\sigma = 1.1 \cdot 10^{-26} b$ ($8.6 \cdot 10^{-27} b$) is the cross-section for the reaction $^{27}\mathrm{Al(p, 3p3n)}^{22}\mathrm{Na}$ (or respectively $^{27}\mathrm{Al(p, 3pn)}^{24}\mathrm{Na}$), N_{av} is the Avogadro constant, λ is the inverse of the life-time of the considered Na isotope and $m = 26.98\,\mathrm{g/mol}$, $\rho = 2.7\,\mathrm{g/\,cm^3}$ and $d = 200\,\mu\mathrm{m}$ are the molar mass, the density and the thickness of the aluminium.
The dose $\mathcal{D}$ absorbed by polystyrene can then be calculated from the formula

$$\mathcal{D} = \frac{\mathrm{N}\left(\frac{\mathrm{dE}}{\rho\ \mathrm{dx}}\right)_p \rho_p\ d_p}{M_p} = \frac{\mathrm{N}\left(\frac{\mathrm{dE}}{\rho\ \mathrm{dx}}\right)_p \rho_p\ d_p}{\rho_p\ \mathrm{S}_p\ d_p} = \frac{\mathrm{N}\left(\frac{\mathrm{dE}}{\rho\ \mathrm{dx}}\right)_p}{\mathrm{S}_{Al}} = \frac{\mathrm{N}\left(\frac{\mathrm{dE}}{\rho\ \mathrm{dx}}\right)_p \rho_{Al}\ d_{Al}}{M_{Al}} \tag{7.2}$$

where the subscript p refers to polystyrene and the subscript Al refers to aluminium. In equation 7.2, N is the total number of protons that hit the aluminium strip during irradiation, $\mathrm{dE}/\rho\mathrm{dx} = 1.936\,\mathrm{MeV\,cm^2/\,g}$ is the mass stopping power for minimum ionizing protons in polystyrene and ρ is the density, S is the surface, M is the mass and d is the thickness of the considered material.

To obtain spatial information the two middle strips were cut in pieces of 0.5, 1 or 2 cm length as shown in Fig. 7.6. The shortest pieces are the ones corresponding to the high dose region, where the dose profile is very steep. The activity of each piece was measured with a germanium detector and equation 7.2 was evaluated for each piece.
Because of the very short half-life of $^{24}\mathrm{Na}$, its activity must be measured within days after the irradiation. Furthermore the precise knowledge of the irradiation

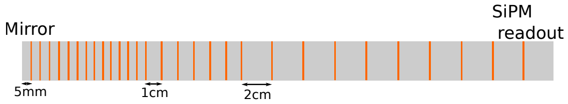

Figure 7.6: The middle Al strips were cut in pieces, which were individually analysed. The segmentation is finer in the high dose region, close to the mirror end.

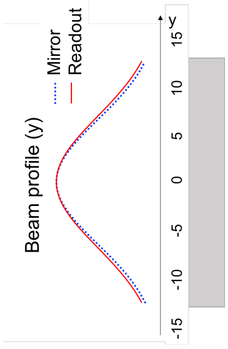

Figure 7.7: Alignment of the aluminium strip with the beam in the vertical direction. Shown are the estimated beam profiles at the mirror end and at the read out end.

time becomes crucial for a correct dose estimate. This is however difficult to achieve because a given aluminium sample can receive dose contributions from different table positions. Therefore the dose evaluation entirely relies on the activity of the longer-lived ^{22}Na, which is still measurable months after the irradiation.

As shown in Figs. 7.1(b) and 7.2(b), the beam has a Gaussian profile in the vertical direction, which slightly widens up from BPM3, located upstream, to BPM4, located downstream of the module. The two middle aluminium strips used for dosimetry are 25 mm high and aligned in a way that the centre of the Gaussian coincide with the centre of the strip as illustrated in Fig. 7.7. Knowing the distance from the Beam Profile Monitors to the Al strips, the beam profiles at the mirror end and at the read out end can be estimated. The so evaluated beam profiles are also shown in Fig. 7.7. The calculation of the dose using equation 7.2 is the average of the dose along the 25 mm. From the estimated beam profiles, the widening of the beam introduces a difference of about 10% in the doses measured with equation 7.2 at the mirror and read out ends. In order to reduce this effect and to compare the absorbed dose with the expected dose, the average dose in a smaller region around zero has to be evaluated. It was chosen to consider the region of ±5 mm around the centre of the Gaussian. The correction factors were derived from the ratio of the integrals under the Gaussians in the ranges $[-5\,\text{mm}, 5\,\text{mm}]$ and $[-12.5\,\text{mm}, 12.5\,\text{mm}]$.

Even after the correction for the beam widening, systematic discrepancies between the corresponding aluminium pieces on the mirror and readout side remained. It was noticed that the discrepancies disappear under the assumption of a small rotational misalignment of the module by 0.5° in the horizontal plane. Considering the difficulty of installing and aligning such a relatively heavy and voluminous object with an asymmetric weight distribution, when the radiation background

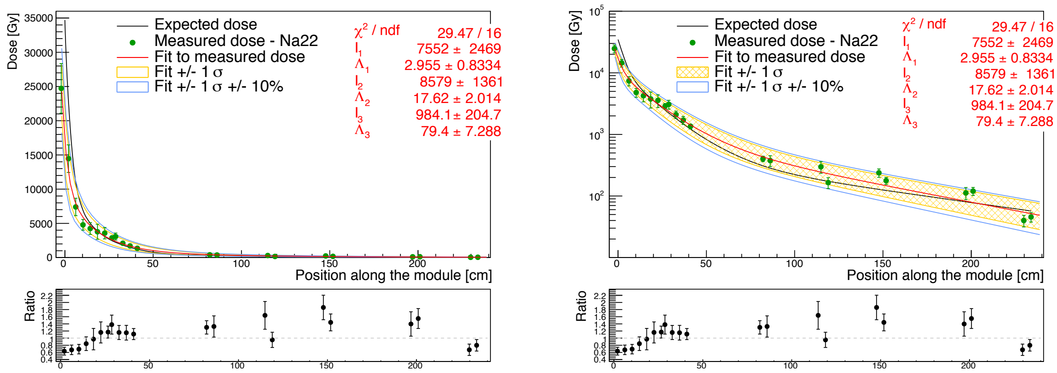

(a) Linear scale

(b) Logarithmic scale

Figure 7.8: Comparison of the expected and measured dose along the module. The black line represents the targeted dose on the module. The data points are the values of the dose measured with ^{22}Na. The data points were fitted with a sum of three exponential functions. The $\pm 1\sigma$ envelope is drawn as a yellow shaded area. The blue lines represent the additional ±10% uncertainty.

(approximately 10 μSv/h) requires to keep the presence of people in the zone as short as possible, it is plausible that such a small misplacement was introduced.

7.3 Results

The dose profile along the module is shown in Fig. 7.8, where the left edge (position $x = 0$) corresponds to the mirror end. All the corrections described in the previous section are included. The data was fitted with a sum of three exponential functions (red line). The plots include also the targeted dose as predicted by the FLUKA calculations (black line). For positions up to 40 cm, the results of the front and back aluminium pieces (0.5 and 1 cm wide) were averaged to a single value per position taking into account the 0.5° rotation. For larger positions the front and back results are plotted individually, with a separation of 4 cm, which corresponds to the 0.5° rotation. The ratio plots at the bottom show the ratio of the measured to target doses.

Due to the CERN end-of-year closure and maintenance needs, not all the aluminium pieces could be analysed on the same Ge spectrometer. Some of the pieces were therefore measured with a second germanium spectrometer. Cross comparisons of a few samples measured on both spectrometers revealed a systematic difference in the resulting activity of 20%, which could neither be resolved nor attributed to one of them. The samples used for the cross-check were representative for the high, low and intermediated dose range. As a pragmatic approach, it was decided to renormalise all measurements by plus or minus 10% to a virtual average spectrometer. To account for this additional uncertainty, the final dose results carry an additional uncertainty of ±10%.

Within the uncertainties, the measured dose profile matches well the targeted

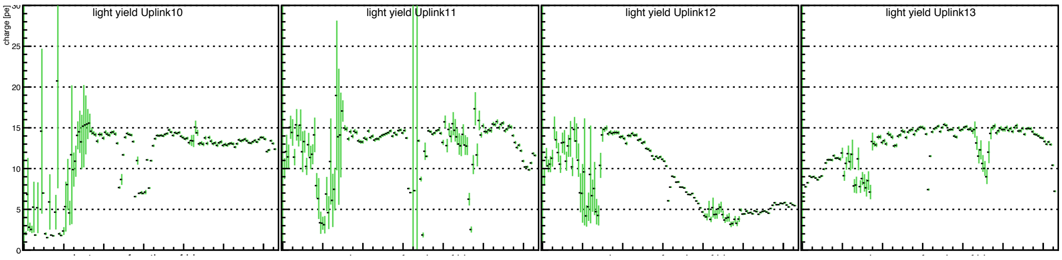

(a) Test beam - One week after

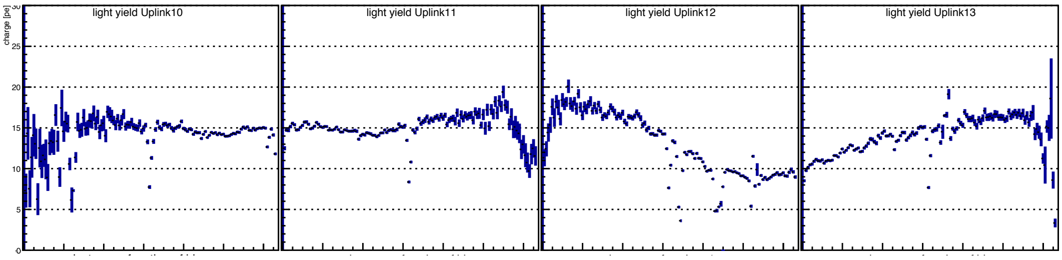

(b) ^{90}Sr - One month after

Figure 7.9: Light yield at the mirror as a function of the SiPM channel [54]. (a) Measurement performed in a test beam about one week after irradiation. (b) Measurement performed in the lab with a ^{90}Sr source about one month after irradiation.

distribution. At positions below 20 cm, the module was under-irradiated by about 20 - 30% while for positions above 50 cm the measured results trend to a 30 - 40% overdose. Overall, the additional absorption experienced by a photon travelling through the whole length of a fibre is expected to be very similar to the one in the upgraded detector at the end of its lifetime. The irradiation can be considered as successful in the sense that it has reproduced a dose distribution which comes very close to the one expected in the final SciFi detector. The biggest limitation for the achievement of the desired dose profile was found to be the instability of the PS beam spot width.

The module was characterised in test beam experiments before and approximately one week after the irradiation [54]. The result of the light yield measurement when the beam was positioned close to the mirror is shown in Fig. 7.9(a). In the non irradiated regions the light yield amounts to about 15 photoelectrons, which is compatible with the result obtained from the same module in a test beam campaign before the PS irradiation. In the irradiated region only about 5 photoelectrons are detected, corresponding to a light loss of approximately 70%. As mentioned in Section 3.4.1, the expected light loss at the mirror, estimated from different irradiation tests on single fibres and fibre bundles, amounts to 40%. The gravity of this result required more investigations. The module was therefore moved to Heidelberg, where it was measured again in the lab using a ^{90}Sr source. This technique had been previously tested and it was found that the beta source provides similar light yield and clusters as the test beam. However the relocation of the module was only possible after the module itself was declared as no more radioactive. Due to the activation of the aluminium endpieces, the ^{90}Sr measurement took place about one month after the irradiation. The resulting light yield is shown in Fig. 7.9(b). The light yield in the non irradiated zone was still about 15 photoelectrons, confirming the validity of the lab measurement. However the irradiated region had recovered and yielded a light loss of about 40%, in agreement with the expectations.

The result of the module irradiation experiment suggested that an annealing of the fibres was occurring with a time scale of about one month. In order to attest this thesis and exclude any other contribution, the radiation resistance of the mirror and glue used to fix the mirror to the fibres were further investigated [82, 83]. Only minor transmission losses in the order of 1 - 2% can be attributed to the glue or mirror degradation. Furthermore, a second module was irradiated again in the PS beam, following the same procedure described above. The dose profile obtained, shown in Fig. 7.10, was very similar to the first irradiation. The instrumentation to measure the light yield with the ^{90}Sr source was setup in the PS IRRAD buffer zone by the Heidelberg SciFi group, so that the measurements could be performed at any time. The plots in Figs. 7.11 and 7.12 [84] summarise the results. One day after irradiation the induced light loss at the mirror amounted to 70%. However a recovery of the fibre is observed and after one month the light loss is reduced to about 40%, as expected from the irradiation tests on single fibres and fibre bundles. The results obtained with the first irradiated module could be exactly reproduced, therefore excluding any external contribution (e.g. a mechanical damage of the module).

In conclusion, after the annealing, the light loss at the mirror in a SciFi module irradiated with a dose profile as in the upgraded LHCb amounts to 40%, as foreseen from the single fibres experiments described in Section 3.4.1. The aim of this experiment was the reproduction, as close as possible, of the conditions in the SciFi Tracker. The geometry of the module was the same and the dose profile very similar as in the SciFi Tracker. Irradiating with 24 GeV/c protons provided the correct particle type and energy range, because the majority of the particles crossing the SciFi detector will consist of multi-GeV charged hadrons. The only big difference between the experiment described in this chapter and the real SciFi Tracker is the dose rate, which will differ by several orders of magnitude. It was shown in Section 6.1 that the permanent damage induced in SCSF-78 fibres after the relatively small dose of 3 kGy is not dose rate dependent. If a dose rate effect might indeed appear when the absorbed dose is augmented by a factor 10 and if the time scale of the recovery is dose rate dependent are questions that still remain unanswered.

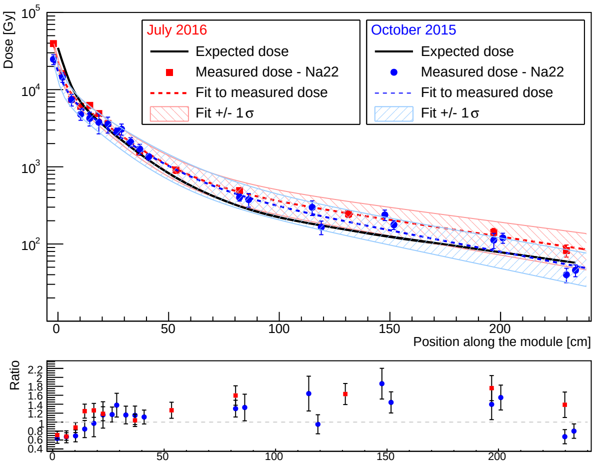

Figure 7.10: Dose profiles for the two irradiated modules. The black line represents the targeted dose. The plot on the bottom shows the ratio of the measured dose along each module with respect to the targeted dose.

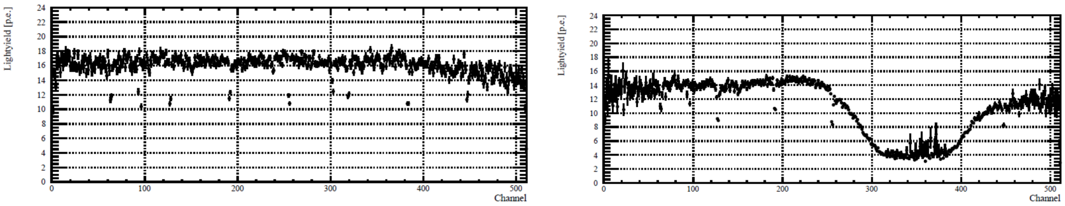

(a) Before

(b) One day after

Figure 7.11: Measurement of the light yield at 2 cm from the mirror as a function of the SiPM channel before (a) and one day after the PS irradiation (b). Plots taken from Ref. [84].

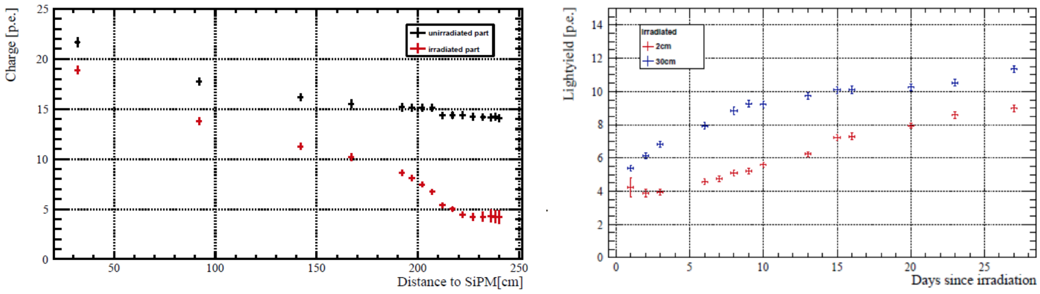

(a)

(b)

Figure 7.12: (a) Measurement of the light yield at different distances from the SiPM for a fixed SiPM channel before the irradiation (black) and one day after the PS irradiation (red). (b) Recovery of the light yield for a fixed SiPM channel at the distance of 2 cm (red) and 30 cm (blue) from the mirror. Plots taken from Ref. [84].

Chapter 8

NOL fibres

An extensive R&D program is ongoing in collaboration with LumInnoTech[1] and Kuraray[2]. The aim is the development of a new class of scintillating fibres based on the Nanostructured Organosilicon Luminophores (NOL) technology. The results presented in this chapter represent the first effort to apply the NOL mechanism to scintillating fibres. After a brief reminder of the scintillation mechanism in conventional scintillating fibres, the NOL principle will be introduced and the latest results of the R&D project will be discussed. Finally an overview on the next steps is given.

A summary of the results presented in this chapter was published in a recent issue of the Journal of Instrumentation [85]. The paper presents the R&D program, focusing on the performances of the best blue and the best green emitting prototype fibres.

8.1 The NOL principle

As briefly discussed in Chapter 2, conventional scintillating fibres are based on a ternary system composed by a solvent, usually polystyrene, an activator (with a concentration of about 1% by weight) and a wavelength shifter (with a concentration of about 0.05% by weight). Activator and wavelength shifter are used to modify the spectrum of the emitted photons, moving it towards longer wavelengths, where the absorption of polystyrene is smaller (Fig. 2.2). Both dyes are randomly distributed into the fibre. The energy transfer between solvent and activator occurs via non-radiative dipole-dipole couplings (Förster transfer). Due to the low concentration of the wavelength shifter, the typical distances between the two dyes amount to ~ 1 - $10\,\mathrm{nm}$. The probability of the non-radiative Förster

---

[1] LumInnoTech LLC, http://www.luminnotech.com. LumInnoTech (Luminescent Innovative Technologies) LLC is a spin-off company of Enikolopov Institute of Synthetic Polymeric Materials of Russian Academy of Sciences.

[2] Kuraray Co. Ltd., http://www.kuraray.com

transfer strongly depends on the distance R between the dyes:

$$P = \frac{1}{1 + (R/R_0)^6} \ . \tag{8.1}$$

In this formula, displayed in Fig. 8.1, R_0 is the distance at which 50% of the energy is transferred via the Förster mechanism and has typical values of a few nanometres [86]. In the case of traditional scintillating fibres the energy transfer between the two luminophores is mostly radiative and the probability for UV photons to escape the scintillating material without being wavelength shifted is higher.

Nanostructured Organosilicon Luminophores (NOLs) are a recently proposed new class of highly efficient organic luminophores [10, 11]. They consist of two types of organic luminophores covalently bonded via silicon atoms. The dendritic structure of a NOL molecule is shown in Fig. 8.2. The silicon bond keeps the distance between activator and wavelength shifter to about 1 - 2 nm and strongly enhances the probability of Förster transfer with respect to traditional scintillating fibres.

Different organic luminophores can be chosen for the synthesis of NOLs, so that both their absorption and emission spectra can be independently tuned to the desired wavelengths regions.

NOLs are compatible with a range of optical polymers such as PMMA, PS or silicones, which in principle allows for the creation of highly efficient scintillating fibres. The simplified concept of light yield increase in NOL fibres with respect to traditional scintillating fibres is shown in Fig. 8.3.

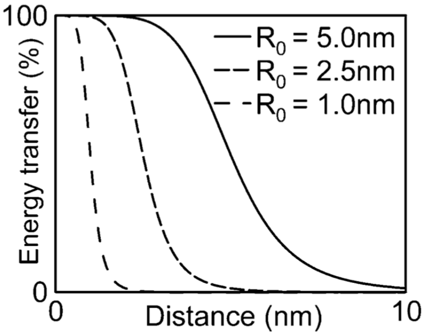

Figure 8.1: Probability of the non-radiative Förster transfer as a function of the distance between two luminophores [86].

8.2 NOL based scintillating fibres

The implementation of the NOL mechanism into scintillating fibres is a non-trivial task. The biggest challenge is related to the ratio between activator and wavelength shifter complexes in pure NOLs, which is not optimal for

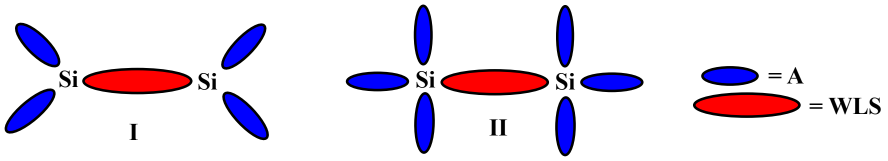

Figure 8.2: Two possible structures of a NOL molecule ([11], modified). Four or six peripheral wavelength shifter (WLS) luminophore units are connected to a central activator (A) unit via silicon atoms.

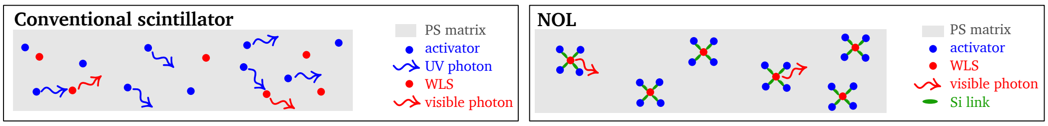

Figure 8.3: Simplified working principle of a conventional scintillating fibre and of a NOL fibre.

scintillating fibres. As discussed in Chapter 2, scintillating fibres necessitate a large concentration of the activator to obtain high light yield, but on the same time a small concentration of wavelength shifter is required to ensure a long attenuation length. Therefore, the prototype fibres discussed in the following consist of a polystyrene base with the addition of a conventional activator and of NOL material, which is used as an efficient wavelength shifter.

The prototype fibres presented in the following contain either NOL11, NOL12 or NOL19[3] in addition to a conventional activator. The concentration of both NOL and activator are varied in order to determine the best combination. The performance of the prototype fibres are characterised in terms of attenuation length, light yield, decay time and radiation hardness. They are then compared to the well-established SCSF-78 and SCSF-3HF fibres from Kuraray. All the produced fibres are circular with a double cladding configuration and a total diameter of 250 µm. The code used to identify the prototype fibres is the following: NOLxx-Yz-w, where xx={11,12,19} is the type of NOL, Y={P,B} is the activator (P=p-Tp, B is another activator, whose type was non-disclosed by Kuraray), z is the activator concentration in percentage by weight and w is the NOL concentration in parts-per-million by weight.

The considered NOLs emit in the blue (NOL11 and NOL12) or in the blue-green wavelength region (NOL19). Figure 8.4 shows the absorption and emission spectra of the individual NOLs measured by LumInnoTech in diluted THF solution. The emission spectra of the prototype fibres measured with the setup described in Section 4.1.1 are shown in Fig. 8.5. As for the SCSF-3HF and SCSF-78 fibres, the emission spectra show a shifting towards longer wavelength when the distance between excitation and detection point increases, i.e. photons

---

[3] LumInnoTech catalogue: http://www.luminnotech.com/index.php/widgetkit

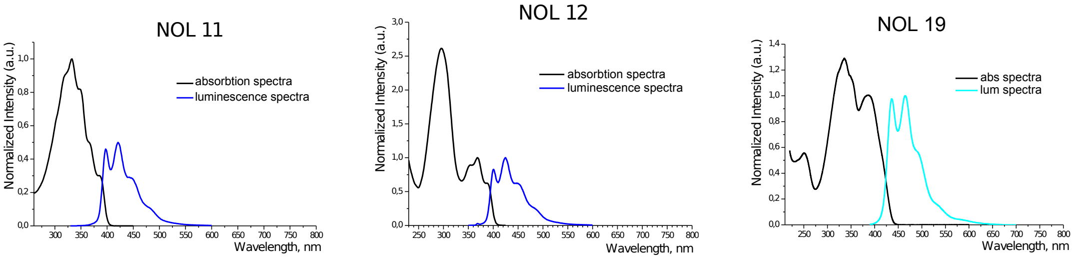

(a) NOL11 (b) NOL12 (c) NOL19

Figure 8.4: Absorption and luminescence spectra of NOL11, NOL12 and NOL19 measured in diluted THF solution. Pictures taken from the LumInnoTech catalogue.

with shorter wavelength tend to be more attenuated than photons with longer wavelengths. This effect is induced by the absorption spectrum of polystyrene (Fig. 2.2) and therefore common to all the fibres discussed in this chapter. Thus, the fact that the emission spectrum of SCSF-78 extends to longer wavelengths with respect to NOL11 and NOL12 (and of SCSF-3HF with respect to NOL19) represents and advantage for the Kuraray fibres.

The tested combination of NOL and activator are summarised in Table 8.1 and graphically represented in Fig. 8.6 together with the attenuation length and light yield measured with the setups described in Chapter 4. The comparison of these values shows that in general the light yield benefits from an increment of the total amount of luminophores. At constant NOL content, increasing the activator by a factor of (about) two results in a 13% (NOL11), 9% (NOL12) or 10% (NOL19) higher light yield. At constant activator content, increasing NOL11 by 200 ppm (NOL12 by 2000 ppm) results in a 14% (29%) higher light yield. At the current stage only NOL11-P2-500 has a light yield comparable to SCSF-78 and SCSF-3HF, although all the fibres containing NOL11 show a good performance. The relatively low values for the samples containing NOL12 and additional activator with respect to NOL11 are probably related to a lower overlapping of the absorption spectrum of NOL12 with the emission spectrum of p-Tp. The photoluminescence quantum yield of the single NOLs in diluted THF solution is reported on the LumInnoTech catalogue: it amounts to 96% for NOL11, 98% for NOL12 and 87% for NOL19. Therefore a lower light yield for the fibres containing NOL19 was expected.

As far as the attenuation length is concerned the three NOLs seem to have a different behaviour. An increment of the activator content does not affect the transport efficiency when the wavelength shifter is NOL11 or NOL12. However this is not the case for NOL19. In addition the longest attenuation length for NOL11 is obtained with a concentration of 400 ppm, whilst for NOL12 the best concentration is 1000 ppm. Several prototype fibres have a transport efficiency comparable to SCSF-78 and SCSF-3HF. Nevertheless the NOL11 samples and one of the NOL19 sample show a non completely satisfactory attenuation length

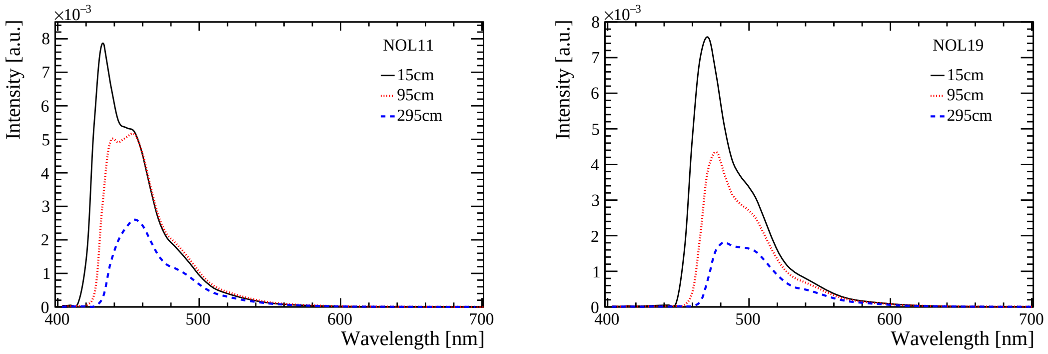

(a) NOL11 (b) NOL19

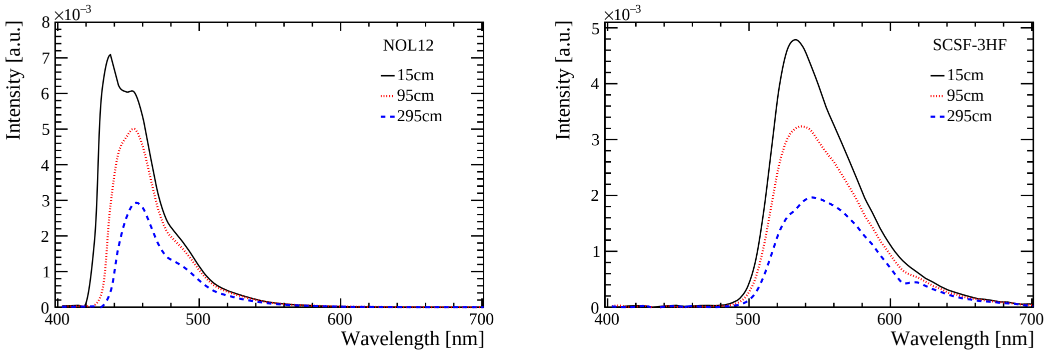

(c) NOL12 (d) SCSF-3HF

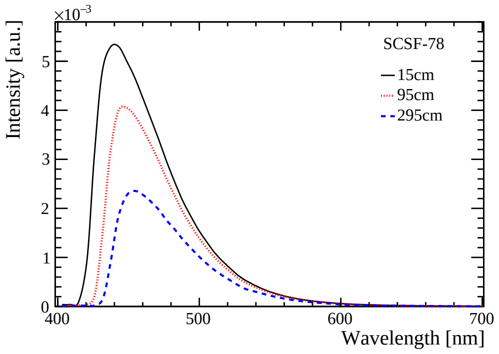

(e) SCSF-78

Figure 8.5: Emission spectra of prototype and reference fibres at distances of 15 cm, 95 cm and 295 cm, respectively, from the spectrometer.

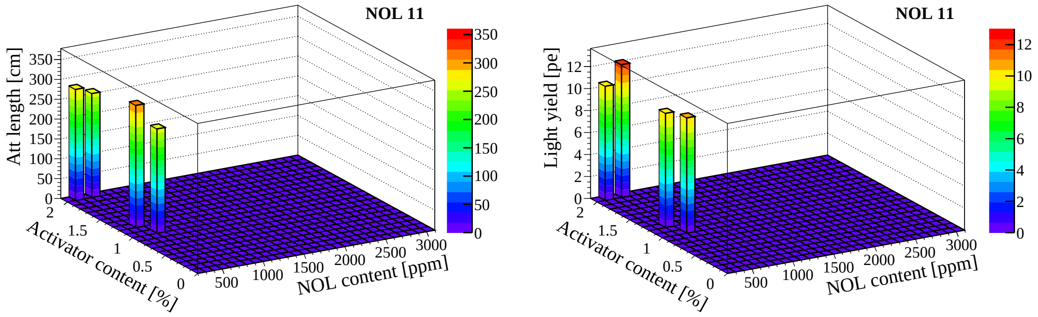

(a) NOL11

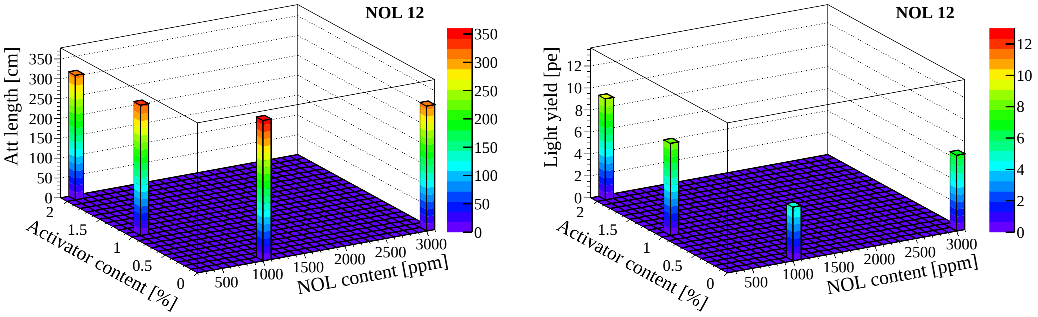

(b) NOL12

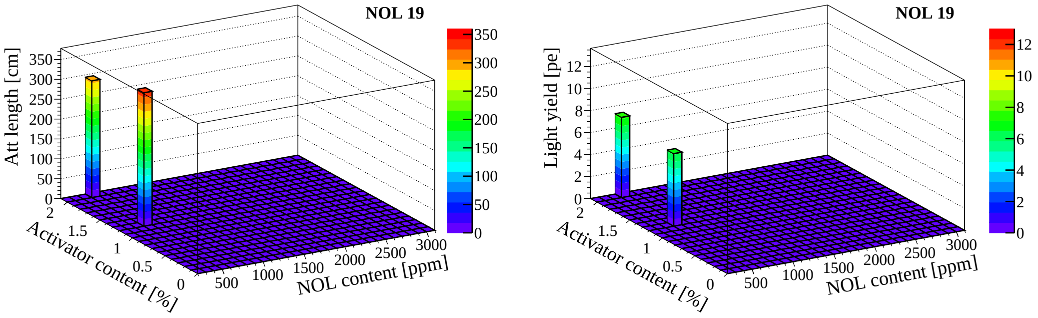

(c) NOL19

Figure 8.6: Attenuation length and light yield of the prototype fibres as a function of the activator's and NOL's concentration.

NOL	Activator	Attenuation length	Light yield
NOL11, 300 ppm	p-Tp, 2%	(280 ± 14) cm	(10.4 ± 0.4) p.e.
NOL11, 400 ppm	p-Tp, 1.2%	(308 ± 15) cm	(10.4 ± 0.4) p.e.
NOL11, 500 ppm	p-Tp, 2%	(263 ± 13) cm	(12.1 ± 0.5) p.e.
NOL11, 500 ppm	$B^{(*)}$, 1%	(262 ± 13) cm	(10.5 ± 0.4) p.e.
NOL12, 300ppm	p-Tp, 1%	(329 ± 16) cm	(8.4 ± 0.3) p.e.
NOL12, 300ppm	p-Tp, 2%	(314 ± 16) cm	(9.2 ± 0.4) p.e.
NOL12, 1000ppm	-	(354 ± 18) cm	(4.9 ± 0.2) p.e.
NOL12, 3000ppm	-	(315 ± 16) cm	(6.9 ± 0.3) p.e.
NOL19, 500ppm	p-Tp, 1.2%	(336 ± 17) cm	(6.6 ± 0.3) p.e.
NOL19, 500ppm	p-Tp, 2%	(294 ± 15) cm	(7.3 ± 0.3) p.e.
SCSF-78$^{(**)}$		(351 ± 18) cm	(13.8 ± 0.6) p.e.
SCSF-3HF		(330 ± 17) cm	(12.2 ± 0.5) p.e.

Table 8.1: Summary of the up to now tested prototype fibres. The details of each fibre's composition and the measured attenuation length and light yield are listed. All the fibres are circular with a double cladding configuration and a total diameter of 250 μm.
$^{(*)}$B is some other conventional activator, different from p-Tp.
$^{(**)}$ The values reported for SCSF-78 correspond to the average of the series production fibres (see Chapter 4).

of $\Lambda \lesssim 300$ cm. This effect can be attributed to the lower purity of the NOL11 with respect to NOL12. When comparing the attenuation lengths of different fibres it should be kept in mind that the response of the PIN-diode is not wavelength-independent. As shown in Fig. 8.7 photons with high wavelength profit from the enhanced sensitivity of the photodiode.

The contribution given by the self-absorption can be evaluated by measuring the emission spectra at very short distances from the excitation point. The distances chosen were ~ 0 mm, 5 mm and 20 mm. The result is shown in Fig. 8.8. For each plot the ratio between the integral of the curves at different distances is reported. The proportion is rather unfavourable for the prototype samples, for which the first peak is absorbed within a few millimetres. On the other end, the intensity of the light emitted by the SCSF-3HF fibre, which exhibits a large Strokes' shift, is almost unaffected in a path-length of 20 mm. The sensitivity of this measurement is not high enough to appreciate the difference among samples with different concentrations of the same NOL type.

In Fig. 8.9 the spectral attenuation lengths of the NOL samples are compared to those of the Kuraray fibres. For clarity purposes only the best sample per NOL type is shown. To simplify the comparison, the wavelength regions on which the emission spectrum of each sample extends are highlighted in the plot. It is thus easy to see that, although SCSF-3HF has a relatively low transport efficiency

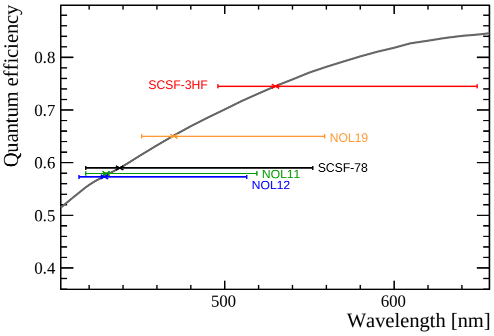

Figure 8.7: Quantum efficiency of the Si-PIN photodiode Newport 818-UV. For each sample the crosses on the horizontal bars correspond to the maximum emission intensity I_{max}, while the bars extend over the wavelength region where $I(\lambda) \geq 0.05 \cdot I_{max}$.

below $\lambda \sim 550$ nm, a big portion of the emitted photons have wavelengths from 550 nm to 650 nm and benefit from much higher attenuation lengths. On the other end, the very high performance of all the other samples at wavelengths above ~ 530 nm concerns only a small fraction of the emitted photons. This is specially true for NOL11 and NOL12. In all samples the enhanced absorption at $\lambda \sim 535$ nm and $\lambda \sim 610$ nm due to vibration levels of polystyrene is visible.

The real breakthrough of these new class of fibres is related to the decay time, since all the prototype fibres are extremely fast. In particular NOL11, NOL12 and NOL19 show decay times of 1.3 ns, 1.4 ns and 1.2 ns, respectively. This is a remarkable result, to our knowledge marking a new record. The prototype fibres are about a factor 6 faster than the green SCSF-3HF ($\tau = 6.2$ ns), about a factor two faster than the blue SCSF-78 ($\tau = 2.4$ ns), which is the fastest commercially available fibre, and about a factor two faster than the fastest fibres produced by Saint-Gobain Crystals[4] ($\tau = 2.7$ ns). The fits to the data, measured with the setup described in Section 4.5, are shown in Fig. 8.10 and Fig. 4.36. The different luminophore concentration affects the decay time by less than 2%, therefore only one sample per NOL type is shown.

The radiation hardness was tested with the X-ray setup described in Section 4.3.2. The dose rate was 23 Gy/min and the total dose 1 kGy. The irradiation of the fibres and the consequent annealing took place in normal laboratory atmosphere at room temperature. The measurement of the attenuation length was performed just after the irradiation and then repeated a week later. The results are shown in Figs. 8.11 - 8.13. The radiation resistance of fibres containing the same luminophores (albeit with different concentrations) is the same, within the error bars. Therefore only one sample per NOL type is shown.
The blue fibres (SCSF-78, NOL11 and NOL12) are less damaged than the green fibres (SCSF-3HF and NOL19). The spectral analysis shows how the resistance

---

[4] Saint-Gobain Crystals, Hiram, Ohio, U.S.A.

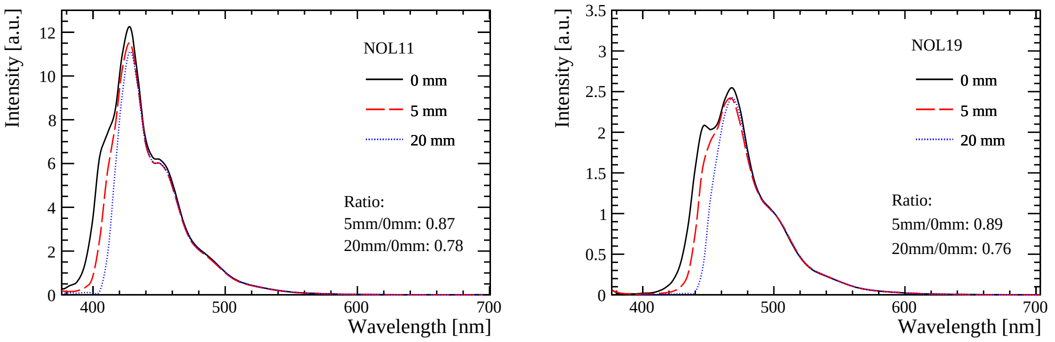

(a) NOL11 (b) NOL19

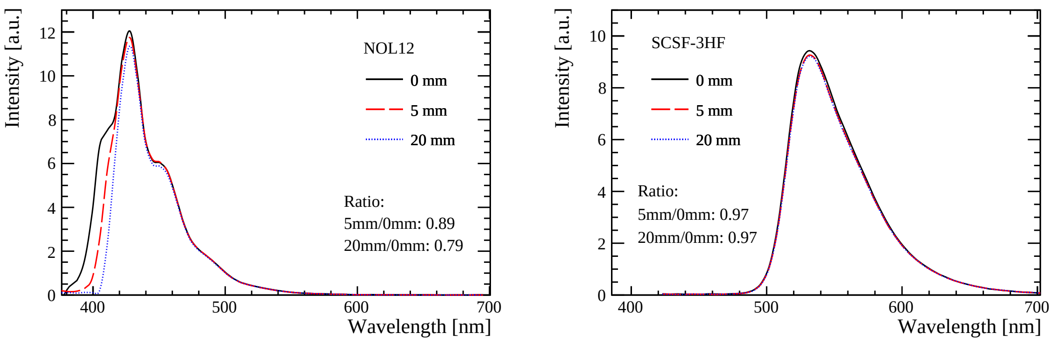

(c) NOL12 (d) SCSF-3HF

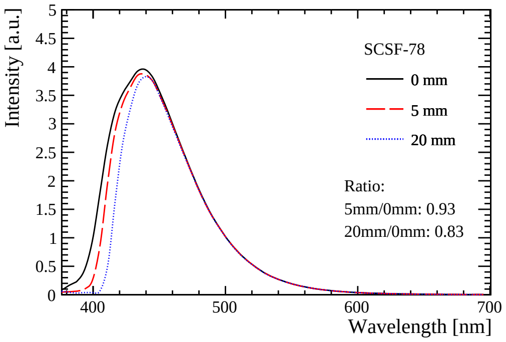

(e) SCSF-78

Figure 8.8: Emission spectra of prototype and reference fibres at distances of ~ 0 mm, 5 mm and 20 mm, respectively, from the spectrometer. The spectra are normalised at either $\lambda = 500$ nm (NOL11, NOL12, NOL19, SCSF-78) or $\lambda = 620$ nm (SCSF-3HF), where no attenuation between 0 and 20 mm is expected.

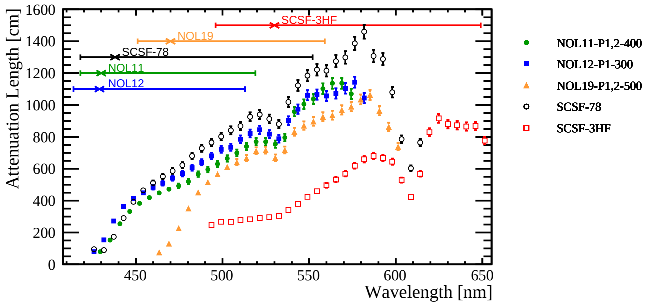

Figure 8.9: Spectral attenuation length of prototype and Kuraray fibres. For each sample the crosses on the horizontal bars correspond to the maximum emission intensity I_{max}, while the bars extend over the wavelength region where $I(\lambda) \geq 0.05 \cdot I_{max}$.

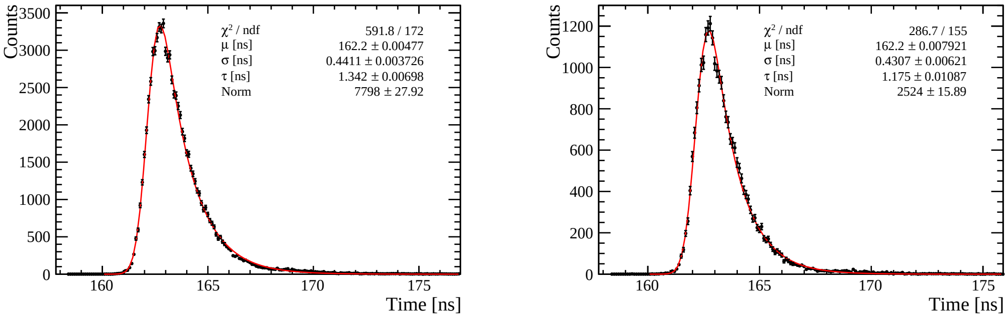

(a) NOL11 (b) NOL19

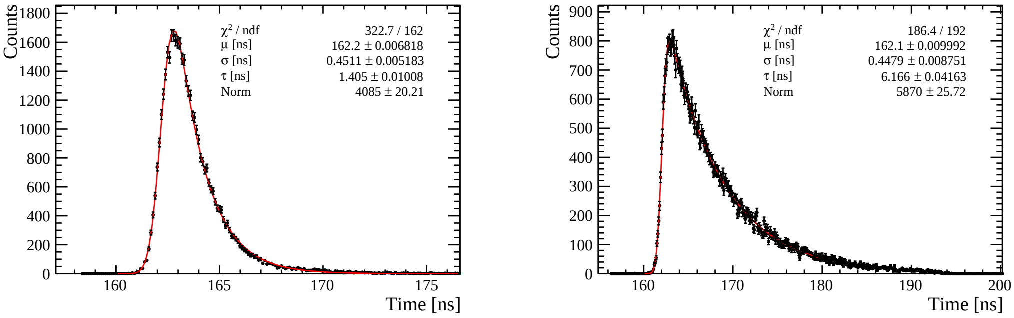

(c) NOL12 (d) SCSF-3HF

Figure 8.10: Decay time of prototype and SCSF-3HF fibres. For comparison, the decay time of SCSF-78 is shown in Fig. 4.36.

to X-rays depends on the chosen dyes. The three blue fibres behave similarly, both after the irradiation and after the annealing, with a more or less pronounced minimum in the wavelength region around 500 nm. The green fibres are equally affected only for wavelengths up to 540 nm, while they exhibit different behaviours in the range 540 - 600 nm. The SCSF-3HF sample shows a faster annealing than the prototype fibre containing NOL19.

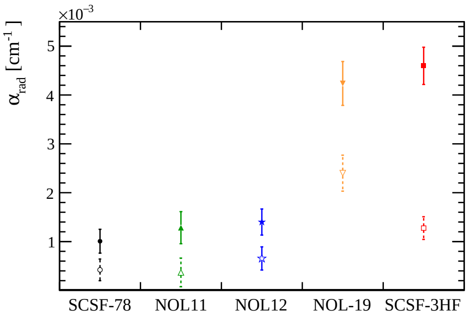

Figure 8.11: Additional attenuation coefficient after X-ray irradiation $\alpha_{\rm rad} \equiv \alpha' - \alpha_0$. For each sample, α_0 has been measured before irradiation, while α' is the attenuation directly after irradiation (filled markers) and after 7 days of annealing (empty markers).

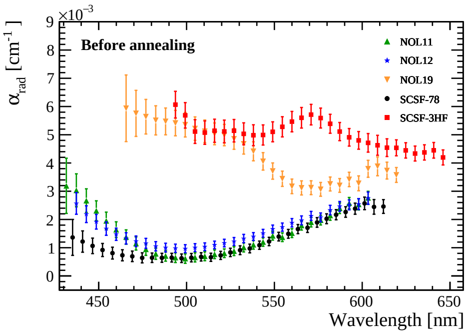

Figure 8.12: Additional attenuation coefficient just after X-ray irradiation.

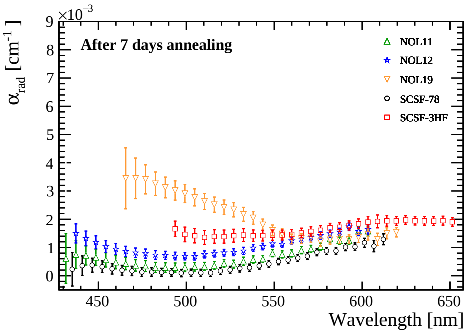

Figure 8.13: Additional attenuation coefficient after 7 days of annealing.

8.3 Discussion and outlook

The comparison of the prototype and Kuraray fibres reveals that the SCSF-78, which is already the default model for the SciFi Tracker, is still the better suited fibre for the LHCb detector. It has the highest light yield and attenuation length. It also shows the highest resistance to X-ray radiation.

All the NOL-based fibres are significantly faster than the SCSF-78 ($\tau_{\rm NOLs} = 1.2$-1.4 ns versus $\tau_{\rm SCSF\text{-}78} = 2.4$ ns). However the requirement of the SciFi Tracker

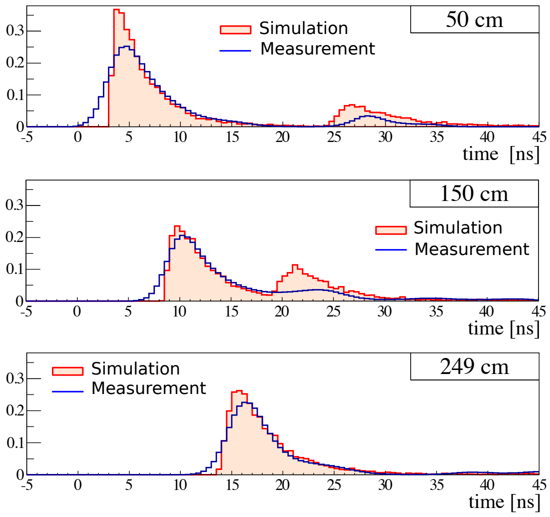

Figure 8.14: Simulation and measurement of the arrival time distribution of photons produced at different distances from the photodetector in a SCSF-78 fibre (∅ = 250 µm). The considered fibre is 2.5 m long and is mirrored at the non-readout extremity. The secondary peak in each distribution is due to the photons reflected at the mirror. In the simulation a decay time of 2.8 ns was considered [87].

on the decay time is not as stringent as for other characteristics like light yield or radiation hardness. Still, a spread of the photon propagation times of up to $2.5\,\mathrm{m} \cdot 6\,\mathrm{ns/m} = 15\,\mathrm{ns}$ has to be taken into account. For photons reflected at the mirror the maximum spread due to the length of the fibres will amount to $2 \cdot 15\,\mathrm{ns} = 30\,\mathrm{ns}$. On top of that, fluctuations due to the decay time of the fibre should be added. The results of a simulation and a measurement of the photons arrival time to the photodetector from different excitation points for SCSF-78 fibres is shown in Fig. 8.14 [87].
Despite their good optical performances, SCSF-3HF fibres can not be considered as an option for the SciFi Tracker because of their relative slowness. With their decay time of about 6 ns a significant fraction of the scintillation light would spill over in the next LHC bunch crossing following with a 25 ns interval.

The analysis of the prototype fibres and the comparison with the performances of the reference fibres lead to a proposal for the next step of the R&D program. The new prototype fibre will contain a new NOL material, based on the same dopants of the SCSF-78 fibres (p-Tp and TPB). This new fibre is currently in production and will likely be ready to be tested at the end of 2017 or beginning of 2018. Through the silicon bond given by the NOL structure, the light yield is expected to significantly increase, whilst the decay time is assumed to decrease with respect to the SCSF-78 fibre. No big differences in the radiation hardness are awaited, neither against X-rays, nor against hadrons irradiations (tests at accelerators shall be performed at a later stage). Such a highly efficient fibre would be well suited for applications in harsh radiation environments and fast readout.

Chapter 9

Conclusions

The LHCb experiment at the LHC is dedicated to the search of physics beyond the Standard Model in the beauty and charm quark sector. It has been collecting data since 2010, providing remarkable results for particle physics.

A major upgrade of the detector will take place in 2019/2020, during the Long Shutdown 2 of the LHC. The upgraded LHCb detector is conceived to take physics data until the end of Run4, foreseen for 2029, collecting data for an integrated luminosity of at least 50 fb^{-1}. It will collect data at an instantaneous luminosity of $2 \cdot 10^{33}\,\text{cm}^{-2}\text{s}^{-1}$, which is a factor 5 higher than the current luminosity. A new full software trigger will increase the readout rate from the current 1 MHz to 40 MHz. Some of the subdetectors will be substituted to cope with the increased occupancy and readout rate. In particular the main tracker, currently consisting of silicon strip detectors in the high η region and straw drift chambers in the low η region, will be replaced by the so-called SciFi Tracker, based on scintillating fibres read out with Silicon PhotoMultipliers. The SciFi Tracker will cover the full acceptance of LHCb after the magnet and will provide a spatial resolution of 85 µm and a detection efficiency of 98.7%.

The fibres chosen for the SciFi Tracker are the SCSF-78 model, produced by the company Kuraray. They are double-cladded, with a nominal diameter of 250 µm and emit in the blue region of the visible spectrum, with a peak at 430 nm. A total of 11′000 km fibres were ordered. They are systematically inspected before being used for the construction of the detector.
The diameter is precisely measured along the whole length of the fibres. A technique was developed to shrink the diameter of occasionally occurring bumps. The shrinking procedure consists in locally heating the fibre over a segment of 1 mm length and pulling it through a tool with a conical shape. This technique reduces the diameter to the acceptable limit of 350 µm, without harming the fibre. The bump shrinking procedure was efficaciously applied to 6′700 km of fibres, with a success rate close to 100% for bumps smaller than 500 µm. Cutting out the bump and joining the extremities with glue is only necessary when the

shrinking procedure fails, on average once every 12.5 km of scanned fibre. In this case a UV curing glue is used.

The optical properties, attenuation length and light yield, are also monitored. The averaged values after 61% of delivered fibres amount to an attenuation length of 351 cm and a light yield of 13.8 photoelectrons.

The degradation of 3.5 m long fibre samples after exposure to 40 keV X-rays is also regularly checked. After a dose of 1 kGy and a dose rate of 23 Gy/min, the attenuation length is reduced on average to 72% of the original value.

In general the properties of the tested fibres are stable and well above the minimum requirements for the LHCb detector.

One of the major challenges for the SciFi Tracker is given by the moderate radiation hardness of plastic scintillators. The literature on this topic is extremely wide, although unfortunately scarce about SCSF-78 fibres. Nevertheless the analysis of the existing literature clearly reveals that the results are strongly dependent on a variety of factors, including the choice of dopants, the dose, the dose rate and the type of particles used to irradiate. To be able to predict the damage induced on a specific plastic scintillator, customized tests should be performed, which reproduce the desired environment.

In the case of the SciFi Tracker, it is extremely difficult to reproduce the exact radiation environment. The 2.5 m long fibres will be exposed to a dose profile, which rapidly changes along the length of the fibre. The highest dose will be registered in the region close to the beam pipe. After 50 fb^{-1} the peak dose will amount to 35 kGy, while the fibres extremities close to the SiPMs will have absorbed only 40 Gy.

Several irradiation campaigns were performed by the SciFi group. Every fibre sample was irradiated to a different dose, covering as much as possible the relevant dose range. Based on these measurements, a signal loss of about 40% is expected in the most irradiated region at the end of the SciFi Tracker's lifetime. The resulting hit efficiency in this region is then foreseen to vary between about 90% and about 99%, depending on the selected threshold to discriminate the signal from the noise.

Some of the irradiation tests were performed in a low dose rate regime. The comparison between fibres irradiated with similar conditions except for the dose rate ($\sim 10^4$ Gy/h in the first case versus $\sim 10^{-1}$ Gy/h in the second case) suggests that the degradation of SCSF-78 is not dose rate dependent.

A full SciFi module was irradiated with 24 GeV protons from the Proton Synchrotron at CERN. The achieved dose profile was very similar to the one in the real SciFi Tracker after 50 fb^{-1}. Characterisation of the module in test beams and in the lab confirmed, after the annealing, a signal loss of about 40% in the most irradiated region.

An R&D program to develop a new class of highly efficient scintillating fibres is currently ongoing. The prototype fibres exploit the NOL technology, in which the dyes are covalently bond via silicon atoms. The new fibres are extremely fast, with decay times of about 1 ns. As far as the light yield and attenuation length are concerned, so far none of the prototype fibres outperforms the SCSF-78, although some of them show similar performances. Therefore the default SCSF-78 fibres remain the most suitable choice for the LHCb detector.

The new prototype fibres, currently under development, will apply the NOL principle to the same dopants as in the SCSF-78 fibres. A significant increase in the speed and light yield with respect to SCSF-78 fibre is excepted, with no loss in the attenuation length and radiation hardness. If successful, this program will deliver fibres suitable for extremely harsh environments.

Recently, the LHCb collaboration has published a proposal for a second major upgrade of the detector (renamed Phase II upgrade, to be distinguished from the Phase I upgrade taking place during Long Shutdown 2). The Phase II upgrade [88] is proposed to be installed during Long Shutdown 4 of the LHC in 2030, aiming at the full exploitation of the flavour physics potential of the High Luminosity (HL) era of the LHC. The construction of a tracker covering a surface of $360\,\mathrm{m}^2$, providing good performances at the conditions of the HL-LHC (luminosity of $2 \cdot 10^{34}\,\mathrm{cm}^{-2}\mathrm{s}^{-1}$, read out at 40 MHz) is an ambitious project. An option to be considered would be a combination of a silicon tracker in the high η region and a SciFi detector in the low η region [89]. Although it is too late to include the novel NOL-based fibres in the Phase I upgrade of the LHCb detector, they might still be appealing for the Phase II upgrade and other experiments in the future.

Bibliography

[1] G.T. Reynolds and P.E. Condon,"*Filament Scintillation Counter*", Rev. Sci. Instrum. 28 (1957) 1098.

[2] S.R. Borenstein,"*Scintillating optical fibres for fine grained hodoscopes*", IEEE Trans. Nucl. Sci., Vol. NS-29, No. 1, February 1982.

[3] Ph. Rebourgeard et al.,"*Fabrication and measurement of scintillating fibres*", Nucl. Instr. and Meth. A 427 (1999) 543-567.

[4] R.E. Ansorge et al.,"*Performance of a scintillating fibre detector for the UA2 upgrade*", Nucl. Instr. and Meth. A 265 (1988) 33-49.

[5] V.M. Abazov et al.,"*The upgraded D∅ detector*", Nucl. Instr. and Meth. A 565 (2006) 463-537.

[6] The Mu3e Collaboration, "*The Mu3e Experiment*", Nucl. Phys. (Proc. Suppl.) B 248-250 (2014) 35.

[7] E.C. Stone et al., "*The Cosmic Ray Isotope Spectrometer for the Advanced Composition Explorer*", Space Science Reviews, Vol. 86, 1998.

[8] The LHCb Collaboration, "*Letter of Intent for the LHCb Upgrade*", CERN-LHCC-2011-001.

[9] The LHCb Collaboration, "*LHCb Tracker Upgrade Technical Design Report*", CERN-LHCC-2014-001.

[10] S.A. Ponomarenko et al., "*Nanostructured organosilicon luminophores and their application in highly efficient plastic scintillators*", Sci. Rep. 4 (2014) 6549.

[11] T.Yu. Starikova et al., "*A novel highly efficient nanostructured organosilicon luminophore with unusually fast photoluminescence*", J. Mater. Chem. C 4 (2016) 4699-4708.

[12] C. Patrignani et al. (Particle Data Group), "*2016 Review of Particle Physics*", Chin. Phys. C, 40, 100001 (2016).

[13] R.C. Rutchi,“*The use of scintillating fibres for charged-particle tracking*”, Ann. Rev. Nucl. Part. Sci. 1996, 46, 281-319.

[14] T. Förster,“*Transfer mechanisms of electronic excitation*”, Discuss. Faraday Soc. 27 (1959) 7.

[15] Y. Li et al.,“*Synthesis and characterizations of benzothiadiazole-based fluorophores as potential wavelength-shifting materials*”, Journal of Photochemistry and Photobiology A: Chemistry 231 (2012) 51-59.

[16] C. DAmbrosio et al., “*Organic scintillators with large Stokes shifts dissolved in polystyrene*”, Nucl. Instrum. Meth. A 307 (1991) 430.

[17] D.Yu. Akimov et al.,“*Development of VUV wavelength shifter for the use with a visible light photodetector in noble gas filled detectors*”, Nucl. Instr. and Meth. A 695 (2012) 403-406.

[18] T. Coffey, S.G. Urquhart, H. Ade,“*Characterization of the effects of soft X-ray irradiation on polymers*”, Journal of Electron Spectroscopy and related Phenomena 122 (2002) 65-78.

[19] J. Blaha et al.,“*Scintillating fibres for particle physics experiments - on-line-induced absorption measurements in gamma radiation field*”, Radiation Measurements 38 (2004) 805-808.

[20] B. Bicken, U. Holm, T. Marckmann, K. Wick,“*Recovery and permanent radiation damage of plastic scintillators at different dose rates*”, IEEE Trans. Nucl. Sci., 38 (2) (1991) 188.

[21] W. Busjian, K. Wick, T. Zoufal,“*Shortlived absorption centers in plastic scintillators and their influence on the fluorescence light yield*”, Nucl. Instr. and Meth. B 152 (1999) 89-104.

[22] A. D. Bross and A. Pla-Dalmau,“*Radiation Damage of Plastic Scintillators*”, IEEE Trans. Nucl. Sci., 39 (5) (1992) 1199.

[23] L. A. Harrah,“*ESR of radicals produced in* ^{60}*Co Gamma-irradiated polystyrene*”, Molecular Crystal, 9 (1969) 197-210.

[24] H.A. Klose et al.,“*On the measurement of degradation and recovery of scintillating plastic fibres*”, Nucl. Instr. and Meth. B 135 (1998) 555-559.

[25] H.B. Dreis, F. Eisele, M. Hildebrandt, B. Schmidt, A. Sponsel, M. Ziegler,“*Development of a Scintillating Fibre Detector for HERA-B*”, DESY 98-049.

[26] G. Buss, A. Dannemann, U. Holm, K. Wick,“*Radiation Damage by Neutrons to Plastic Scintillators*”, Nuclear Science Symposium and Medical Imaging Conference, 1994 IEEE Conference Record.

[27] A. D. Bross and A. Pla-Dalmau,“*Radiation-induced hidden-absorption effects in polystyrene-based plastic scintillators*”, ACS-Symposium Series: Radiation effects on polymers, 1991, p. 475.

[28] J. S. Wallace, M. B. Sinclair, K.T. Gillen, R. L. Clough, “*Color center annealing in* γ*-irradiated polystyrene, under vacuum and air atmospheres*”, Rad. Phys. Chem., 41 (1993) 85.

[29] K. Wick, T. Zoufal,“*Unexpected behaviour of polystyrene-based scintillating fibres during irradiations at low doses and low dose rates*”, Nucl. Instr. and Meth. B 185 (2001) 341-345.

[30] K. Hara et al.,“*Radiation hardness and mechanical durability of Kuraray optical fibers*”, Nucl. Instr. and Meth. A 411 (1998) 31-40.

[31] U. Holm, K. Wick,“*Radiation stability of plastic scintillators and wavelength shifters*”, IEEE Trans. Nucl. Sci., 36 (1) (1989) 579.

[32] M. M. Hamada, P. R. Rela, F. E. da Costa, C. H. de Mesquita,“*Radiation damage studies on the optical and mechanical properties of plastic scintillators*”, Nucl. Instr. and Meth. A 422 (1999) 148-154.

[33] AR. Ziegler, U. Holm, N. Latuske, K. Wick, T. Zoufal, “*In situ measurement of radiation damage in scintillating fibres*”, Advanced Technology and Particle Physics, 2002, pp. 826-830.

[34] K.F. Johnson, H.L. Whitaker, “*Temperature treatment of plastic scintillator affects radiation hardness*”, Nucl. Instr. and Meth. A 301 (1991) 372-375.

[35] The LHCb collaboration, “*The LHCb detector at the LHC*”, JINST 3, 2008, S08005.

[36] S.L. Glashow, “*Partial-symmetries of weak interactions*”, Nucl. Phys. 22, 579 (1961).

[37] A. Salam, J.C. Ward, “*Electromagnetic and weak interactions*”, Phys. Lett. 13, 168 (1964).

[38] S. Weinberg, “*A Model of Leptons*”, Phys. Rev. Lett. 19, 1264 (1967).

[39] The CMS Collaboration, “*Observation of a new boson at a mass of* 125 GeV *with the CMS experiment at the LHC*”, Phys. Lett. B 716, 30 (2012).

[40] The ATLAS Collaboration, “*Observation of a new particle in the search for the Standard Model Higgs boson with the ATLAS detector at the LHC*”, Phys. Lett. B 716, 1 (2012).

[41] L. Evans and P. Bryant, “*LHC machine*”, JINST 3, 2008, S08001.

[42] D. R. Tovey, “*The LHC: Past, Present and Future*”, ATL-PHYS-PROC-2014-129.

[43] The LHCb Collaboration, Public web page:
http://lhcb-public.web.cern.ch/lhcb-public/, Post dated September 7, 2017.

[44] The LHCb Collaboration, “*First Evidence for the Decay* $B_s^0 \to \mu^+\mu^-$”, Phys. Rev. Lett. 110 (2013) 021801.

[45] CMS Collaboration & LHCb Collaboration, “*Observation of the rare* $B_s^0 \to \mu^+\mu^-$ *decay from the combined analysis of CMS and LHCb data*”, Nature 522, 68-72 (2015).

[46] The LHCb Collaboration, “*Observation of* $J/\psi p$ *Resonances Consistent with Pentaquark States in* $\Lambda_b^0 \to J/\psi K^- p$”, Phys. Rev. Lett. 115, 072001 (2015).

[47] M.Gell-Mann, “*A schematic model of baryons and mesons*”, Phys. Lett. 3, 214 (1964).

[48] Ken H. Hicks, “*On the conundrum of the pentaquark*”, Eur. Phys. J. H 37 (2012) 1.

[49] The LHCb Collaboration, “*Implications of LHCb measurements and future prospects*”, Eur. Phys. J. C (2013) 73: 2373.

[50] The LHCb Collaboration, “*LHCb Trigger and Online Upgrade Technical Design Report*”, CERN-LHCC-2014-016.

[51] The LHCb Collaboration, “*LHCb Particle Identification Upgrade Technical Design Report*”, CERN-LHCC-2013-022.

[52] The LHCb Collaboration, “*LHCb VELO Upgrade Technical Design Report*”, CERN-LHCC-2013-021.

[53] LHCb collaboration,“*LHCb Scintillating Fibre Tracker Engineering Design Review Report: Fibres, Mats and Modules*”, CERN-LHCC-2015-008.

[54] The LHCb Scintillating Fibre Tracker Collaboration (including L. Gavardi), “*LHCb Scintillating Fibre Tracker: Test Beam Report 2015*”, LHCb-PUB-2015-025.

[55] S. Nieswand, PhD. thesis, thesis in preparation.

[56] N. Lopez March and M. Karacson, “*Radiation studies for the LHCb tracker upgrade*”, CERN-LHCb-PUB-2014-022.

[57] T.T. Böhlen et al., “*The FLUKA Code: Developments and Challenges for High Energy and Medical Applications*”, Nuclear Data Sheets 120 (2014) 211-214.

[58] A. Ferrari et al., “*FLUKA: a multi-particle transport code*”, CERN-2005-10 (2005), INFN/TC_05/11, SLAC-R-773.

[59] C. Joram et al.,“*Measurements and radiation tests on scintillating fibres for the LHCb SciFi project*”, CERN-LHCb-INT-2013-002.

[60] B. Leverington, C. Joram and S. Baker,“*Scintillating Fibre Irradiation with* 22.9 MeV *Protons*”, CERN-LHCb-PUB-2014-024.

[61] R. Ekelhof, “*Studies for the LHCb SciFi Tracker*”, PhD thesis, CERN-THESIS-2016-098.

[62] C. Joram, SciFi General Meeting, CERN, December 1, 2014.

[63] C. Alfieri, A.B. Cavalcante, C. Joram,“*A set-up to measure the optical attenuation length of scintillating fibres*”, CERN-LHCb-PUB-2015-011.

[64] A. Hiramoto,“*Measurements of SciFi for LHCb upgrade*”, CERN-STUDENTS-Note-2015-163.

[65] C. Alfieri et al.,“*An experimental set-up to measure Light Yield of Scintillating Fibres*”, CERN-LHCb-PUB-2015-012.

[66] PANalytical, XRD Glass Tube Brochure, download at:
http://www.panalytical.com/XRD-Glass-Tube/Features.htm.

[67] NIST database, J. H. Hubbell and S. M. Seltzer, “*X-Ray Mass Attenuation Coefficients*”, https://www.nist.gov/pml/x-ray-mass-attenuation-coefficients.

[68] Muench et al.,“*Photon energy dependence of the sensitivity of radiochromic film and comparison with silver halide film and LiF TLDs used for brachytherapy dosimetry*”, Medical Physics 18 (1994) 769-775.

[69] G. Poludniowski et al.,“*SpekCalc: a program to calculate photon spectra from tungsten anode x-ray tubes*”, Phys Med Biol. 2009 Oct 7;54(19):N433-8.

[70] L. Gavardi et al.,“*A setup to perform X-ray irradiation tests on scintillating fibres for the SciFi project*”, CERN-LHCb-PUB-2017-008.

[71] A.B. Cavalcante et al.,“*Scanners for the quality control of scintillating plastic fibres*”, CERN-LHCb-PUB-2015-009.

[72] A.B. Cavalcante et al. (including L. Gavardi),“*Shrinking of bumps by drawing scintillating fibres through a hot conical tool*”, CERN-LHCb-PUB-2016-010.

[73] A.B. Cavalcante et al. (including L. Gavardi),“*Quality of scintillating fibres after hot bump shrinking*”, CERN-LHCb-PUB-2016-009.

[74] O. Shinji, Kuraray Co. LTD, Private communication, May 2016.

[75] B. Leverington, Private communication.

[76] R. Ekelhof, LHCb SciFi Upgrade Tracker Meeting, CERN, February 16, 2012.

[77] National Nuclear Data Center, Brookhaven National Laboratory, "*Chart of Nuclides*", http://www.nndc.bnl.gov/chart.

[78] M. Eichmann, "*Development of a high precision dosimetry system for the measurement of surface dose rate distribution for eye applicators*", Medical Physics 36 (10) (2009), 4634-4643.

[79] F. Ravotti et al., "*A new high-intensity proton irradiation facility at the CERN PS east area*", Procedings of the TIPP conference, 2-6 June 2014, Amsterdam, PoS(TIPP2014)354.

[80] Particle Data Group (PDG), Atomic and Nuclear Properties of Materials, http://pdg.lbl.gov/2017/AtomicNuclearProperties/.

[81] A.B. Cavalcante et al. (including L. Gavardi), "*Irradiation of a* 2.5 m *long SciFi module with* 24 GeV/c *protons to the dose profile expected in LHCb*", CERN-LHCb-PUB-2016-001.

[82] C. Joram and T. Schneider, "*Mirroring of fibre ends for the LHCb SciFi project*", CERN-LHCb-PUB-2014-020.

[83] C. Joram et al. (including L. Gavardi), "*Irradiation test of mirror samples for the LHCb SciFi tracker*", CERN-LHCb-PUB-2016-006.

[84] B. D. Leverington, SciFi Testbeam meeting, CERN, August 31, 2016.

[85] L. Gavardi et al., "*Development of a New Class of Scintillating Fibres with Very Short Decay Time and High Light Yield*", JINST 12, 2017, P05013.

[86] A. Esposito, H. C. Gerritsen, F. S. Wouters, "*Fluorescence Lifetime Imaging Microscopy: Quality Assessment and Standards*", Springer Ser Fluoresc (2008) 6: 117-142.

[87] M. Deckenhoff, "*Signal Shape and Time of Light Propagation in Scintillating Fibre SCSF-78MJ from Kuraray* ", CERN-LHCb-PUB-2014-016.

[88] The LHCb collaboration, "*Expression of Interest for a Phase-II LHCb Upgrade: Opportunities in flavour physics, and beyond, in the HL-LHC era*", CERN-LHCC-2017-003.

[89] C. Joram, "*Intro to Phase-II Tracking and SciFi tracker*", Beyond the LHCb Phase-1 Upgrade Workshop, May 28-31, 2017, La Biodola, Isola d'Elba (Italy).

Acknowledgements

I would like to express my gratitude to all the people that directly contributed to the accomplishment of this thesis project.

First of all I wish to thank Dr. Johannes Albrecht for offering me to work on this thesis project and for agreeing to and supporting my long stay at CERN. I also would like to thank Dr. Christian Joram for welcoming me and giving me the great opportunity to be part of his group. I am also very grateful to Prof. Dr. Kevin Kröninger for reviewing my thesis.

The work presented in this manuscript could not have been achieved without all the persons that helped me by sharing their expertise, time and technical instrumentation. I would like to acknowledge Robert Kristic, Miranda Van Stenis and Thomas Schneider for the considerable technical support. I am very grateful to Eraldo Olivieri and Leszek Ropelewski for introducing me to their X-ray setup and allowing me to use it extensively. Also many thanks to Federico Faccio for providing the calibrated silicon diode. I also wish to acknowledge the major contribution of the PS irrad team (Federico Ravotti, Maurice Glaser, Blerina Gkotse and Giuseppe Pezzulo) in the successful module irradiation and consequent dose evaluation and in the dosimetry for the X-ray setup.

I would like to thank all the colleagues from the LHCb SciFi project for the very fruitful collaboration. I am very grateful to my everyday work companions in the last two years, Ana Barbara Rodriges Cavalcante, Lukas Gruber and again Christian Joram for letting me profit from your knowledge through daily discussions about the fibres, the setups, the SciFi project and the physics in general and for motivating me with your constant passion and excitement for work you do. Finally I would like to thank Tobias Tekampe for the unlimited support, often requested largely outside the working hours, in the non-applied matters as statistics, software and programming.